

DISSERTATION

zur Erlangung des akademischen Grades

"doctor rerum naturalium"

(Dr. rer. nat.)

in der Wissenschaftsdisziplin

"Klimaphysik"

Quantification of Internal Variability of the Arctic Summer Atmosphere based on HIRHAM5 Ensemble Simulations

eingereicht an der

Mathematisch-Naturwissenschaftlichen Fakultät
der Universität Potsdam



von

ANJA SOMMERFELD

Betreuer: Prof. Dr. Klaus Dethloff



Einreichung am 23. Mai 2015

Disputation am 11. November 2015

Published online at the
Institutional Repository of the University of Potsdam:
URN urn:nbn:de:kobv:517-opus4-85347
<http://nbn-resolving.de/urn:nbn:de:kobv:517-opus4-85347>

Abstract

The non-linear behaviour of the atmospheric dynamics is not well understood and makes the evaluation and usage of regional climate models (RCMs) difficult. Due to these non-linearities, chaos and internal variability (IV) within the RCMs are induced, leading to a sensitivity of RCMs to their initial conditions (IC). The IV is the ability of RCMs to realise different solutions of simulations that differ in their IC, but have the same lower and lateral boundary conditions (LBC), hence can be defined as the across-member spread between the ensemble members.

For the investigation of the IV and the dynamical and diabatic contributions generating the IV four ensembles of RCM simulations are performed with the atmospheric regional model HIRHAM5. The integration area is the Arctic and each ensemble consists of 20 members. The ensembles cover the time period from July to September for the years 2006, 2007, 2009 and 2012. This time period is chosen because of the melting sea ice and its impact on the atmospheric circulation and the resulting influence on the IV. The specific years are selected due to their minimum summer sea ice area that was achieved within the years. Based on the mean September sea ice area, the years 2007 and 2012 are defined as low ice years and 2006 and 2009 as high ice years. The investigation of these classified years enables an analysis of a relationship between the sea ice conditions and the internally generated variability. The ensemble members have the same LBC and differ in their IC only. The different IC are arranged by an initialisation time that shifts successively by six hours. Within each ensemble the first simulation starts on 1st July at 00 UTC and the last simulation starts on 5th July at 18 UTC and each simulation runs until 30th September. The analysed time period ranges from 6th July to 30th September, the time period that is covered by all ensemble members. The model runs without any nudging to allow a free development of each simulation to get the full internal variability within the HIRHAM5.

As a measure of the model generated IV, the across-member standard deviation and the across-member variance is used and the dynamical and diabatic processes influencing the IV are estimated by applying a diagnostic budget study for the IV tendency of the potential temperature developed by Nikiema and Laprise [2010] and Nikiema and Laprise [2011]. The diagnostic budget study is based on the first law of thermodynamics for potential temperature and the mass-continuity equation. The resulting budget equation reveals seven contributions to the potential temperature IV tendency.

As a first study, this work analyses the IV within the HIRHAM5. Therefore, atmospheric circulation parameters and the potential temperature for all four ensemble years are investigated. Similar to previous studies, the IV fluctuates strongly in time. Further, due to the fact that all ensemble members are forced with the same LBC, the IV depends on the vertical level within the troposphere, with high values in the lower troposphere and at 500 hPa and low values in the upper troposphere and at the surface. By the same reason, the spatial distribution shows low values of IV at the boundaries of the model domain.

The diagnostic budget study for the IV tendency of potential temperature reveals that the seven contributions fluctuate in time like the IV. However, the individual terms reach different absolute magnitudes. The budget study identifies the horizontal and vertical 'baroclinic' terms as the main contributors to the IV tendency, with the horizontal 'baroclinic' term producing and the vertical 'baroclinic' term reducing the IV. The other terms fluctuate around zero, because they are small in general or are balanced due to the domain average. The investigation of the spatial distribution illustrates that the horizontal transport term reaches the same magnitude like both 'baroclinic' terms, but has a producing and reducing impact on the IV, depending on the location.

The comparison of the results obtained for the four different ensembles (summers 2006, 2007, 2009 and 2012) reveals that on average the findings for each ensemble are quite similar concerning the magnitude and the general pattern of IV and its contributions. However, near the surface a weaker IV is produced with decreasing sea ice extent. This is caused by a smaller impact of the horizontal

'baroclinic' term over some regions and by the changing diabatic processes, particularly a more intense reducing tendency of the IV due to condensative heating. However, it has to be emphasised that the behaviour of the IV and its dynamical and diabatic contributions are influenced mainly by complex atmospheric feedbacks and large-scale processes and not by the sea ice distribution.

For a detailed understanding of the contributions leading to the IV it is necessary to analyse individual cases of high IV. Therefore, 13 time steps within the four ensembles are selected and examined concerning the relationship between the IV tendency of the potential temperature and the corresponding atmospheric situation.

Additionally, a comparison with a second RCM covering the Arctic and using the same LBC and IC is performed. For both models very similar results concerning the IV and its dynamical and diabatic contributions are found. Hence, this investigation leads to the conclusion that the IV is a natural phenomenon and is independent from the applied RCM.

Zusammenfassung

Das nicht-lineare Verhalten der atmosphärischen Dynamik ist noch immer nicht ausreichend verstanden und daher sind die Evaluierung und die Anwendung von regionalen Klimamodellen (RCM) schwierig. Aufgrund dieser Nicht-Linearitäten wird Chaos und modellinterne Variabilität (IV) in RCMs erzeugt, was zur Sensitivität der RCMs bezüglich ihrer Anfangsbedingungen führt. Die IV ist die Fähigkeit von RCMs, verschiedene Lösungen für Simulationen zu erzeugen, die sich in ihren Anfangsbedingungen unterscheiden, aber die gleichen unteren und seitlichen Randbedingungen aufweisen. Daher kann die IV als die Spannweite zwischen den Ensemblemitgliedern definiert werden.

Für die Untersuchung der IV und deren dynamische und diabatische Beiträge werden vier Ensembles mit dem atmosphärischen Regionalmodell HIRHAM5 erzeugt. Das Integrationsgebiet ist die Arktis und jedes Ensemble besteht aus 20 Ensemblemitgliedern. Die Ensembles umfassen den Zeitraum von Juli bis September für die Jahre 2006, 2007, 2009 und 2012. Der Zeitraum wurde aufgrund der sommerlichen Schmelzperiode des Meereises definiert, um die Auswirkung auf die atmosphärische Zirkulation und den damit verbundenen Einfluss auf die IV zu untersuchen. Die Wahl der Ensemblejahre wird aufgrund der minimalen sommerlichen Meereisausdehnung, welche in den entsprechenden Jahren auftrat, getroffen. Anhand der mittleren Meereisausdehnung im September werden die Jahre 2007 und 2012 als Jahre mit geringer und die Jahre 2006 und 2009 als Jahre mit hoher Meereisausdehnung definiert. Diese Einteilung ermöglicht die Ermittlung eines Zusammenhanges zwischen den Meereisbedingungen und der modellinternen Variabilität. Die Mitglieder eines Ensembles haben alle die gleichen unteren und seitlichen Randbedingungen und unterscheiden sich nur in ihren Anfangsbedingungen. Die unterschiedlichen Anfangsbedingungen werden durch eine Verschiebung der Initialisierungszeit um jeweils 6 Stunden erzeugt. Innerhalb eines jeden Ensembles wird die erste Simulation am 1. Juli um 00 UTC gestartet und die letzte Simulation beginnt am 5. Juli um 18 UTC. Jede Simulation endet am 30. September. Um gleich lange Simulationen für die Auswertung zu gewährleisten, wird die Studie für den Zeitraum vom 6. Juli bis 30. September durchgeführt. Das Modell wird ohne Nudging betrieben, um jeder Simulation eine freie Entwicklung zu gewähren und damit die modellinterne Variabilität des HIRHAM5 vollständig zu erhalten.

Als Maß für die im Modell generierte IV wird die Standardabweichung und die Varianz zwischen den Ensemblemitgliedern bestimmt. Die die IV beeinflussenden dynamischen und diabatischen Prozesse werden mit Hilfe der diagnostischen Budgetstudie zur Berechnung der IV Tendenz der potentiellen Temperatur bestimmt. Diese diagnostische Budgetstudie wurde von Nikiema and Laprise [2010] und Nikiema and Laprise [2011] entwickelt und basiert auf dem ersten Hauptsatz der Thermodynamik für die potentielle Temperatur und der Massenkontinuitätsgleichung. Aus der resultierenden Budgetgleichung können sieben Terme, die zu der Tendenz der potentiellen Temperatur beitragen, berechnet werden.

In dieser Arbeit wird erstmalig die IV des HIRHAM5 analysiert. Dafür werden Parameter der atmosphärischen Zirkulation und die potentiellen Temperatur für alle vier Ensemblejahre analysiert. Wie auch frühere Studien zeigten, schwankt die IV stark mit der Zeit. Außerdem wird eine vertikale Abhängigkeit der IV innerhalb der Troposphäre gefunden, mit hohen Werten in der unteren Troposphäre und in 500 hPa. Geringe Werte hingegen treten in der oberen Troposphäre und am Erdboden auf, da alle Ensemblemitglieder mit den gleichen Randbedingungen angetrieben werden. Daher zeigt auch die räumliche Verteilung niedrige IV Werte am Rand des Modellgebietes.

Die diagnostische Budgetstudie für die IV Tendenz der potentiellen Temperatur verdeutlicht, dass die sieben Beiträge ebenfalls mit der Zeit schwanken wie die IV selbst. Jedoch erreichen die einzelnen Terme unterschiedliche Intensitäten. Mit Hilfe der Budgetstudie können der horizontale und vertikale 'Baroklinitätsterm' als die wichtigsten Beiträge zur Tendenz der IV ermittelt werden.

Dabei trägt der horizontale 'Baroklinitätsterm' zur Produktion und der vertikale 'Baroklinitätsterm' zur Reduktion der IV bei. Die anderen Beiträge schwanken um Null, weil sie an sich klein oder aufgrund des Gebietsmittels ausbalanciert sind. Die Untersuchung der räumlichen Verteilung verdeutlicht, dass der horizontale Transportterm die gleiche Größenordnung erreicht wie die 'Baroklinitätsterme', aber, in Abhängigkeit von der Region, einen erhöhenden und einen reduzierenden Einfluss auf die IV hat.

Der Vergleich der Resultate für die Ensembles untereinander (Sommer 2006, 2007, 2009 und 2012) führt zu dem Erkenntnis, dass im Mittel die Ergebnisse für die IV und ihre Beiträge, die Größenordnung und die Muster betreffend, sehr ähnlich sind. Nur nahe der Erdoberfläche wird mit abnehmender Meereisausdehnung eine schwächere IV generiert. Dies ist bedingt durch einen geringeren Einfluss des horizontalen 'Baroklinitätsterms' der in manchen Regionen auftritt sowie durch die sich ändernden diabatischen Prozesse (Tendenz zur intensiveren Reduktion der IV) aufgrund von Erwärmung durch Kondensation. Jedoch ist das Verhalten der IV und ihrer dynamischen und diabatischen Beiträge durch komplexe atmosphärische Rückkopplungen und großskaligen Prozessen beeinflusst und nicht nur durch die Meereisverteilung.

Für ein detaillierteres Verständnis der Beiträge zur IV ist es erforderlich individuelle Ereignisse mit hoher IV zu untersuchen. Daher werden aus den vier Ensembles 13 Zeitschritte ausgewählt, anhand derer der Zusammenhang zwischen der IV Tendenz der potentiellen Temperatur und den entsprechenden atmosphärischen Bedingungen untersucht wird.

Des Weiteren wird ein Vergleich mit einem zweiten RCM durchgeführt. Dieses zweite RCM wird mit den selben unteren und seitlichen Randbedingungen und Anfangsbedingungen angetrieben wie das HIRHAM5. Für beide Modelle werden sehr ähnliche Ergebnisse für die IV und ihre dynamischen und diabatischen Beiträge gefunden. Daher führt die Untersuchung zu dem Schluss, dass die IV ein natürliches Phänomen und damit unabhängig von dem verwendeten RCM ist.

List of Abbreviations

A_h	Horizontal transport term
A_v	Vertical transport term
B_h	Horizontal 'baroclinic' term
B_v	Vertical 'baroclinic' term
C	Diabatic source and sink term
CRCM	Canadian Regional Climate Model
DA	Dipole anomaly
E	East
ECHAM5	European Centre Hamburg Model Version 5
ECMWF	European Centre for Medium-Range Weather Forecasts
E_h	Horizontal third-order term
EGR	Eady growth rate
E_v	Vertical third-order term
GCM	General circulation model
HIRHAM	High Resolution Hamburg Model
HIRLAM7	High Resolution Limited Area Model Version 7
IC	Intitial conditions
IV	Internal variability, across-member variance
JAS	July, August, September
LBC	Lateral boundary conditions
mslp	Mean sea level pressure

N	North
NSIDC	National Snow and Ice Data Center
RCM	Regional climate model
S	South
SST	Sea-surface temperature
UTC	Coordinated Universal Time
W	West

Contents

1	Introduction	1
1.1	Motivation	1
1.2	Objectives	4
2	Regional Climate Model	7
2.1	HIRHAM5 Model Description	7
2.2	Simulation Set-Up	10
3	Diagnostic Methods	13
3.1	Evaluation of HIRHAM5	13
3.2	Internal Variability (IV)	15
3.3	Diagnostic Budget Study for IV Processes	16
3.3.1	Budget Equation for Potential Temperature IV	16
3.3.2	Explanation of the Contribution Terms	23
4	Atmospheric and Sea Ice Conditions in the Selected Summers	25
4.1	Examined Years for the Investigation of IV	25
4.2	Evaluation of HIRHAM5	31
4.3	Cyclonic Activity	36
5	Simulated IV based on HIRHAM5	41
5.1	IV of Mean Sea Level Pressure and Geopotential	41
5.2	IV of Potential Temperature	46
6	Processes of Potential Temperature IV	53
6.1	Vertical Profile of the Contributions to IV Tendency	56
6.2	Temporal Evolution of the Contributions to IV Tendency	59
6.3	Spatial Distribution of the Contributions to IV Tendency	64
6.4	Impact of the Sea Ice Distribution on the IV and its Contributions	71

7	Comparison of Potential Temperature IV based on HIRHAM5 and CRCM5	77
7.1	CRCM Model Description	77
7.2	Results	79
7.2.1	Comparison of Potential Temperature IV	79
7.2.2	Comparison of the Contributions to IV Tendency	80
8	Case Studies of the Processes of Potential Temperature IV	85
8.1	Case: 23rd July 2006 00 UTC	87
8.2	Case: 15th September 2007 18 UTC	89
8.3	Case: 16th August 2009 00 UTC	91
8.4	Case: 5th August 2012 06 UTC	94
9	Conclusion and Outlook	97
9.1	Summary and Discussion	97
9.1.1	Arctic IV and the Contributions to IV Tendency	97
9.1.2	Dependency of the Arctic IV on the Sea Ice Conditions	99
9.1.3	Dependency of the Arctic IV on the Model	101
9.2	Outlook	101
	Bibliography	103
A	Appendix	i
A.1	Equations	i
A.2	Figures	ii
A.2.1	Vertical Profile of the Contributions to IV Tendency	ii
A.2.2	Temporal Evolution of the Contributions to IV Tendency	iii
A.2.3	Spatial Distribution of the Contributions to IV Tendency	iv

Chapter 1

Introduction

1.1 Motivation

During the last decade, the debate concerning the climate change focused on the Arctic, partly owing to the polar amplification for example caused by the ice-albedo feedback or since global climate models (GCMs) indicated that enhanced greenhouse gas concentration induce strongest changes in climate in the high-latitudes [IPCC, 2013]. Hence, the importance of using regional climate models (RCMs) is steadily growing for a more precise understanding and investigation of the meteorological and climatological conditions in the Arctic with a finer spatial resolution. GCMs, with their coarse horizontal resolution, are not able to fully capture atmospheric meso- and small-scale processes [Denis et al., 2002]. Hence, RCMs with their finer spatial resolution provide an added value due to their facility to simulate small scales with the right amplitude and the right climate statistics [Laprise et al., 2008]. The finer spatial resolution of RCMs makes it possible to resolve processes on a smaller scale leading to a more realistic simulation of the regional climate (Christensen et al. [1998], Giorgi and Bi [2000] and Christensen et al. [2001]). Therefore, dynamical downscaling is achieved by nesting a RCM with higher horizontal resolution into a GCM or global reanalysis data sets.

Both, GCMs and RCMs are sensitive to their initial conditions (IC) due to the non-linearities within the atmosphere and its dynamic [Lorenz, 1963], leading to internally generated variability in the models. The chaotic atmospheric flow induces a deterministic predictability in GCMs that is limited to two weeks when the IC differ between two simulations [Lucas-Picher et al., 2008b]. After two weeks the simulations produce totally different solutions. This internal variability (IV) of GCMs is comparable to the variability of the natural system [Caya and Biner, 2004]. Several studies argued that RCMs exhibit IV as well (Giorgi and Bi [2000], Christensen et al. [2001], Caya and Biner [2004], Rinke et al. [2004], Wu et al. [2005], Alexandru et al. [2007], Lucas-Picher et al. [2008a], Lucas-Picher

et al. [2008b], Roesch et al. [2008]). von Storch [2005] defined the IV as the possibility of RCMs to generate solutions for simulations that differ from each other, despite they use exactly the same lower and lateral boundary conditions (LBC), but slightly different IC. Giorgi and Bi [2000], Caya and Biner [2004], Lucas-Picher et al. [2008a] and several more found that the IV in RCMs is reduced compared to the one in GCMs, because the LBC provided by the GCMs or reanalysis data sets limit the degree of freedom of the RCM. Therefore, the possibility of the RCM to develop their own circulations, that differ from the forcing fields, is reduced. Hence, the predictability of the RCMs is extended [Lucas-Picher et al., 2008b], but the IV can have an influence on the interpretation of sensitivity studies produced with RCMs (Giorgi and Bi [2000], Rapać et al. [2011]). It has to be decided whether the anomalies in sensitivity studies are due to physical term or are injected by the IV [O'Brien et al., 2011]. Therefore, it is an important goal to estimate and quantify the IV generated in RCMs. The investigation of the sensitivity to the IC helps to analyse the potential predictability of the RCM.

A common method of investigating the IV in RCMs is the use of ensemble simulations. The ensembles are arranged by perturbing each ensemble member or by shifting the initialisation time. Both lead to a different solution of each simulation within an ensemble. Until now there were several studies dealing with the topic of the appropriate size of the RCM ensemble. This strongly depends on the problem that should be analysed. The numerical weather prediction uses large ensembles with sizes of five to 50 members [Theis and Gebhardt, 2009] and even up to 100 members [Gneiting and Raftery, 2005], because the predictability is increased and the percentage of outliers is decreased for a high ensemble size [Buizza and Palmer, 1998]. Covering the subject of investigating the IV in RCMs, the ensemble size differs strongly between the studies. Alexandru et al. [2007], Lucas-Picher et al. [2008a], Nikiema and Laprise [2010], Nikiema and Laprise [2011] and O'Brien et al. [2011] applied large ensembles for the examination of the IV. Whereas Rinke and Dethloff [2000] did not find a converging behaviour of IV due to the increase of the ensemble size from four to eight members. Lucas-Picher et al. [2008a] specify that the IV decreases with increasing ensemble size, but conclude that an ensemble size of six members is solid. Though Alexandru et al. [2007] used an ensemble with 20 members and recommended to build an ensemble with at least ten members to ensure a robust investigation of IV. During the last few years the trend was towards these enhanced ensemble sizes of 20 members for the analysis of the IV (Nikiema and Laprise [2010], Nikiema and Laprise [2011] and O'Brien et al. [2011]). The approach of using 20 member to generate an ensemble is applied in this present study as well.

Several studies analysed different factors that exert an impact on the IV in RCMs. Such factors are the IC, LBC, domain size, nudging, model parameterisations and geographical

location of the model domain (Giorgi and Bi [2000], Caya and Biner [2004], Rinke et al. [2004], Wu et al. [2005], Alexandru et al. [2007], Alexandru et al. [2009], Lucas-Picher et al. [2008a], Separovic et al. [2011], Omrani et al. [2012a], Omrani et al. [2012b]). The behaviour and the magnitude of the IV in RCMs depends on dynamical and diabatic processes like convection [Cr  tat and Pohl, 2012], precipitation (Giorgi and Bi [2000], Christensen et al. [2001]) and synoptic events (Caya and Biner [2004], Alexandru et al. [2007]). The impact of the geographical location of the model domain and the associated synoptic conditions is noticeable by comparing studies covering different regions. Giorgi and Bi [2000] investigated Asia, Christensen et al. [2001] the Mediterranean area, Cr  tat and Pohl [2012] the (sub-) tropical region (South Africa), Caya and Biner [2004], Alexandru et al. [2007], Lucas-Picher et al. [2008a], Rapa  c et al. [2011], Nikiema and Laprise [2010], Nikiema and Laprise [2011] different areas over North America, Roesch et al. [2008] Europe, Wu et al. [2005] Alaska and Rinke and Dethloff [2000] and Rinke et al. [2004] the Arctic. All found an IV dependency on the domain and seasonal specific atmospheric conditions. In general, the mid-latitudes are considered as well-flushed areas and therefore, the simulations within an ensemble that differ in their IC diverge only slightly from each other [von Storch, 2005]. In contrast for the Arctic a larger divergence between the simulations occur, due to the fact that baroclinic perturbations stay longer within the Arctic [Rinke and Dethloff, 2000]. Hence, the IV in RCMs covering the Arctic domain is larger compared to those for the mid-latitudes (Rinke et al. [2004], Sommerfeld et al. [2015]).

The investigation performed by Nikiema et al. [2015] more clearly illustrates the enhanced importance of the model domain compared to the applied RCM. They used the Canadian Regional Climate Model (CRCM) over the Arctic to analyse the IV generated within the RCM and got quite similar results as obtained with the HIRHAM5 by Sommerfeld et al. [2015].

Another factor influencing the IV is the often applied nudging procedure within the RCMs (Alexandru et al. [2009], Separovic et al. [2011], Omrani et al. [2012a] and Omrani et al. [2012b]). Their experiments with different kinds and intensities of nudging showed that an enhanced nudging leads mostly to a decreased IV within a RCM since the capability of the RCM simulations to develop free from the driving field is reduced. Therefore, the IV is smaller and the reproduction of the driving fields is improved [Omrani et al., 2012a]. In this work, the RCM is applied without any nudging to enable the free development of each ensemble member to estimate the magnitude of the IV generated in the RCM.

Additionally, to the quantification of the IV generated in RCMs, it is important to investigate the physical drivers that induce the IV. Hence, Nikiema and Laprise [2010] and Nikiema and Laprise [2011] were the first who developed a method to examine the dy-

namical and diabatic processes resulting in IV. This method addresses the IV of potential temperature and is based on a diagnostic equation for potential temperature derived from the first law of thermodynamics and the mass-continuity equation using the Reynolds decompositions (see Sec. 3.3.1). With the help of the diagnostic equation the individual contributions influencing the IV tendency within the RCM are quantified. They applied the study over an area covering northeastern part of Northern America and the Atlantic Ocean and found a temporal evolution of IV that fluctuates strongly in time and is connected to synoptic events. The diabatic term contributes strongest to a production of IV, while the vertical 'baroclinic' term reduces the IV with the same magnitude.

1.2 Objectives

The aim of this thesis is the estimation of the IV generated within the RCM HIRHAM5 over the Arctic. Previous studies that investigated the IV over the Arctic (Rinke and Dethloff [2000], Rinke et al. [2004]) used the former model version HIRHAM4. Hence, this is the first work that quantifies and examines the IV of the HIRHAM5. Further, the dynamical and diabatic contributions to the IV tendency over the Arctic are analysed for the first time by applying the method of the diagnostic equation for potential temperature developed by Nikiema and Laprise [2010]. The following key questions are formulated to be solved within this work: What are the characteristics (spatial distribution, vertical profile, temporal behaviour) of the IV in HIRHAM5? Which are the most important terms contributing to the IV tendency over the Arctic? Is there a relation between the sea ice distribution and the IV and its contributions? How do the results for the Arctic differ compared to the northeastern part of the Northern American region? Depends the calculated IV generated in an Arctic RCM on the applied model?

The investigated time period is the late summer (from July to September (JAS)), because this season is characterised by intense Arctic sea ice retreat. The wide area of ice free ocean results in an enhanced exchange of heat and moisture between the ocean and the atmosphere affecting the diabatic processes (Porter et al. [2012], Rinke et al. [2013]) and further, has an impact on the synoptic activity (Jaiser et al. [2012], Rinke et al. [2013]). Those processes can influence the IV and the role of the corresponding contributions. Although, it is known that the IV reaches its maximum over the Arctic during autumn and winter, due to the polar vortex that hamper the transport of the perturbations out of the model domain [Rinke et al., 2004], the period of interest in this work is the summer. The atmospheric circulation and the planetary wave activity are weaker during summer and hence, local and regional diabatic and baroclinic perturbations could have a stronger influence on the IV. Besides, the mean sea level pressure (mslp) and the $2m$ air temperature

1.2. OBJECTIVES

biases are smaller in summer compared to the winter season [Dethloff et al., 1996]. To investigate the possible dependency of IV and its dynamical and diabatic contributions on the sea ice distribution, years with low and high sea ice concentration are examined with respect to the mean September sea ice area. This method is specified in Sec. 4.1 and reveals the selection of the years 2006 and 2009 representing the high ice years and the years 2007 and 2012 representing low ice years.

This work is organised as follows: In Chapter 2 the used RCM HIRHAM5 and the arrangements of the ensemble simulations are described. The used methods, including an extensive derivation of the diagnostic budget equation for the IV of the potential temperature will be established in Chapter 3. Chapter 4 deals with the evaluation of the HIRHAM5 that is applied without any nudging in this study. In Chapter 5 the simulated IV is analysed for the mslp, the geopotential height and the potential temperature, followed by a further investigation of the IV of potential temperature with respect to its dynamical and diabatic contributors in Chapter 6. Chapter 7 compares the IV and its dynamical and diabatic contributions over the Arctic that is generated within the HIRHAM5 and the CRCM5. A detailed analysis of individual high IV events is given in Chapter 8. The findings and conclusions will be summarised in Chapter 9.

Chapter 2

Regional Climate Model

2.1 HIRHAM5 Model Description

In this study, the atmospheric RCM HIRHAM5 (High Resolution Hamburg Model version 5) [Christensen et al., 2007] is applied. It combines the regional weather forecast model HIRLAM version 7 (High Resolution Limited Area Model [Undén et al., 2002]) and the atmospheric GCM ECHAM5 (version 5.4.00) (European Centre Hamburg Model [Roeckner et al., 2003]). The HIRLAM7 provides the dynamical core and ECHAM5 the physical parameterisations for HIRHAM5. Both are coupled over an interface which arranges the exchange of parameters and variables within HIRHAM5. The model (the dynamical core of HIRLAM7) solves seven prognostic equations for the variables horizontal wind, surface pressure, temperature, specific humidity, cloud water content and cloud ice content. Besides two diagnostic variables (vertical motion and geopotential) are calculated.

HIRHAM5 is a hydrostatic grid point based model and has been integrated with a spatial resolution of approximately 0.25° (~ 25 km) on a rotated latitude-longitude grid and in the vertical 40 levels are used. The upper boundary is situated at 10 hPa (~ 31 km) and ten levels are in the lowest 1 km covering the Arctic boundary layer. In the vertical the discretisation is based on a sigma-pressure-hybrid coordinate ($\sigma - p$ - coordinates; Roeckner et al. [2003] and Eckermann [2009]) that is terrain-following near the ground and involves pressure coordinates in the upper levels. An Arakawa staggered C-grid [van Engelen et al., 1997] is used for the horizontal discretisation of the prognostic variables to enable an accurate representation of the horizontal advection. HIRHAM5 runs with a semi-implicit leapfrog time stepping scheme as time discretisation with a time step of 120 seconds.

The considered area is the circum Arctic region north of approximately 60° N (pan-Arctic domain, see Fig. 2.1) with 218 x 200 grid cells in the horizontal. The mesh grid of approximately 0.25° enables a complex representation of the orography with the Greenland

ice sheet of 3000 m height (see Fig. 2.1).

Due to the horizontal resolution of approximately 0.25° all physical processes beyond the grid-scale have to be parameterised in the model. The parameterisations are provided by the ECHAM5 and include short- and long-wave radiation schemes, convection, condensation, turbulence and vertical diffusion. The parameterisation schemes are shortly explained here and a detailed description can be found in Roeckner et al. [2003] and Klaus [2014]. Despite the HIRHAM5 time step is 120 seconds, both radiation schemes calculate the radiative transfer every two hours due to the high numerical effort. Within these two hours the temporally varying solar zenith angle is considered. The Tanre climatology [Tanre et al., 1984] is used for the radiative transfer to include the distribution of atmospheric aerosols that varies spatially but not temporally. In HIRHAM5 the short-wave (solar) radiation scheme developed by Fouquart and Bonnel [1980] is implemented and includes six solar spectral bands, three for the near infra-red and three in the visible/ultra-violet spectral range. The HIRHAM5 uses Mie-scattering for short-wave radiation that is scattered due to clouds [Rockel et al., 1991]. The long-wave (terrestrial) radiation scheme was developed by Mlawer et al. [1997] and considers 16 spectral bands. The radiation parameterisation contains a formulation of albedo. For grid cells that are fully covered by open water the albedo in HIRHAM5 is set constant to 0.07. The albedo of grid cells that are partly covered by water and ice is estimated by using a weighted mean. For the snow-free land surface HIRHAM5 uses an annually averaged background albedo based on satellite data [Hagemann, 2002]. A separation and a weighted average is done for snow-covered land areas when the grid cells are partly covered by forest. Besides, the Køltzow-albedo scheme is implemented in HIRHAM5. This scheme was developed by Køltzow [2007] for the Arctic region and contains a improved snow- and ice-albedo parameterisation including melt ponds.

The parameterisation scheme for convective processes in HIRHAM5 is formulated by Tiedtke [1989]. This mass flux scheme distinguishes between deep, shallow and mid-level convection. Deep and shallow convection are generated within the lowest model level and have a cloud thickness of $> 200 \text{ hPa}$ and $\leq 200 \text{ hPa}$. The mid-level convection is calculated only when both former convection types occur, the relative humidity is $> 90 \%$ and an upward movement is found at the cloud base. These cloud types are not parameterised separately within a grid cell, but are summarised within an ensemble that is parameterised for a one-dimensional column.

The scheme for condensation processes in HIRHAM5 considers prognostic equations (for specific humidity, cloud water content and cloud ice content), cloud microphysics and the prognostic statistical cloud scheme developed by Tompkins [2002]. The cloud microphysics includes several types of forming precipitation (e. g. coalescence, aggregation,

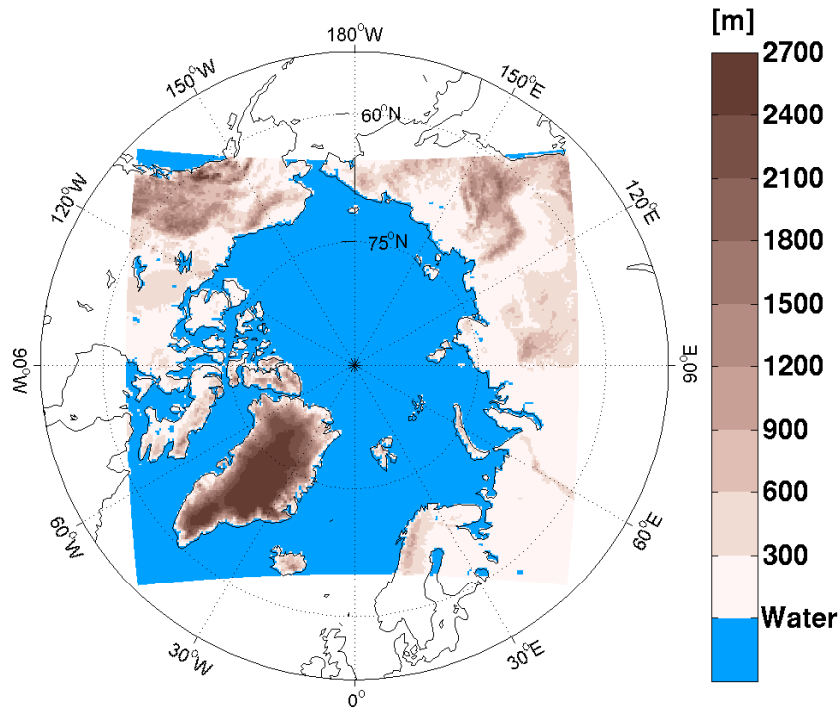


Figure 2.1: HIRHAM5 pan-Arctic model domain and orography in *m*.

accretion), evaporation of rain, sublimation of snow and ice, freezing of cloud water and melting of cloud ice.

The parameterisation of turbulence uses the Reynolds decompositions meaning the separation of an atmospheric variable in its temporal mean and its deviation. The parameterisation of the turbulent fluxes within the surface layer (from the surface up to 10 *m* representing the lowest vertical model level) is estimated by a transfer equation that calculates the vertical exchange of momentum, heat and humidity for the surface types land, water and ice. The parameterisation of the turbulence above the surface layer is performed with the eddy diffusion method implementing the relation between the turbulent fluxes and the vertical gradient of the averaged variable.

The ERA-Interim reanalysis data set [Dee et al., 2011] provided by the ECMWF (European Centre for Medium-Range Weather Forecasts) was used to initialise HIRHAM5 and to provide the LBC. The data set has a horizontal resolution of 0.75° . During the simulation the ERA-Interim data set drives HIRHAM5 every six hours with the sea-surface temperature (SST) and the sea ice concentration at the lower boundaries. The sea ice thickness is part of the lower boundary conditions and is set constant to 2 *m* in each ice covered grid cell. Snow on ice is not considered. As lateral boundaries the ERA-Interim data set prescribes every six hours the surface pressure and in each vertical level the horizontal wind components, temperature, specific humidity, cloud water and cloud ice. The surface temperature, background albedo, vegetation ratio and the leaf area index belong to the IC

that base on monthly climatologies. The orography, orography variance, land sea mask, roughness length, forest, soil type, soil wetness, soil water holding capacity, glacier fields and snow depth are as well used as IC.

The lateral boundary zone spans ten grid cells. In these grid cells a boundary relaxation (developed by Davies [1976]) is applied for the lateral forcing with the ERA-Interim data set. The outermost grid cells fully represent the prognostic variables of ERA-Interim. It follows a zone of nine grid cells that are characterised by a weighting between the driving data and the model solution. Towards the inner model domain the influence of the driving ERA-Interim data set decreases quasi-exponentially. After the ten boundary grid cells the model solution is based on the HIRHAM5 only.

To ensure a good reproduction of the atmospheric conditions due to the RCM simulations the HIRHAM5 usually is applied with an indiscriminate nudging [Omrani et al., 2012a] meaning a dynamical relaxation [Davies and Turner, 1977]. This indiscriminate nudging is implemented in HIRHAM5 with a magnitude of 1 %. Hence, every time step at each grid cell in all vertical levels, the prognostic variables are calculated with 99 % from the HIRHAM5 and with 1 % by the driving data set (ERA-Interim) [Klaus, 2014]. Applying this nudging leads to a suppression of the sensitivity of the RCM to their IC and hence reduce the IV of the model. Further, this increases the predictability and improves the ability of the RCM to reproduce the driving fields [Omrani et al., 2012a]. However, the aim of this study is the investigation of the IV generated within the HIRHAM5. Therefore, all simulations are carried out without any nudging.

A detailed description of the RCM HIRHAM5 can be found in Klaus [2014]. The HIRHAM5 (with indiscriminate nudging) was evaluated and applied by Klaus et al. [2012], Klaus [2014] and Zhou et al. [2014] for the Arctic region. They analysed spatial distributions and annual cycles for several meteorological parameters and describe the ability of the HIRHAM5 to simulate the spatial and temporal features in agreement with reanalysis and observational data in general, but with some biases.

2.2 Simulation Set-Up

Ensemble simulations

To analyse and quantify the IV of the HIRHAM5 it is important to keep the model variability in its basic state, as recommended by Alexandru et al. [2007]. Therefore, HIRHAM5 has been run without any nudging in this work. As investigated in previous studies (e. g. Alexandru et al. [2007], Lucas-Picher et al. [2008a]), the number of simulations belonging to an ensemble needs to be large enough to allow a solid estimation of the IV. Alexandru et al. [2007] found that an ensemble size of 20 members fulfills this condition and more

ensemble members do not lead to an improvement of the estimation of the IV. Therefore, I follow Alexandru et al. [2007] and use an ensemble with 20 members. The individual members use the same LBC and differ in their atmospheric IC only. This is arranged by a different initialisation time that was shifted successively by six hours in each case. The first simulation starts on 1st July at 00 UTC, the second starts on 1st July at 06 UTC, the third starts on 1st July at 12 UTC, etc. and the last simulation starts on 5th July at 18 UTC. Each simulation is performed then continuously until 30th September 18 UTC. The analysis is applied for the time period that is covered by all ensemble members from 6th July until 30th September. It is noteworthy that the considered time period including the HIRHAM5 spin-up time of approximately five days. Hence, the spin-up time is not excluded from the temporal averages of the HIRHAM5 ensembles. The ensemble simulations are performed for four different years, namely 2006, 2007, 2009 and 2012. These years were chosen based on their sea ice minimum during the summer season. The underlying idea was to select two years with high ice conditions (2006 and 2009) and two years with low ice conditions (2007 and 2012) that occur during the years of this millenium (see Sec. 4.1).

Output

The budget study for potential temperature accounts temperature tendencies due to radiation, vertical diffusion, condensation and convection (see Section 3.3.1). These variables are not part of the standard model output and therefore have to be written out additionally. They are calculated in the tendency diagnostics of the ECHAM5 part in HIRHAM5. The temperature tendency diagnostics contains and calculates all physical and dynamical processes separately that contribute to the total temperature tendency. Therefore, the temperature tendencies due to radiation, vertical diffusion, convection and condensation are saved separately. The temperature tendency due to radiation summarises thermal and solar radiation conditions. All temperature tendencies have the unit K/s and are accumulated over the time steps and stored every six hours. In the vertical HIRHAM5 runs at 40 levels, however, due to storage capacity both, the standard model output and the temperature tendencies are saved only for 19 pressure levels in the vertical: 10, 30, 50, 70, 100, 200, 250, 300, 400, 500, 600, 700, 800, 850, 900, 925, 950, 975 and 1000 hPa and every six hours.

Chapter 3

Diagnostic Methods

The present chapter describes the three methods used for analysing the simulated basic state of the Arctic atmospheric conditions and its performance compared to the ERA-Interim data set (Sec. 3.1), the IV within HIRHAM5 (Sec. 3.2) and the quantification of dynamical and diabatic reasons for the IV (Sec. 3.3).

3.1 Evaluation of HIRHAM5

First, the four years which will be used for the whole study need to be chosen with respect to low and high ice conditions. Therefore, the anomaly of the mean September sea ice area covering the time from 1979 to 2012 provided by the ERA-Interim data set is used. The sea ice area represents the total area of sea ice meaning that regions with open water are removed. The anomaly is calculated by subtracting the mean September sea ice area climatology (1981 to 2010 like defined by [NSIDC, 2015]) from each individual year within this time period (see Fig. 4.1). Fig. 4.1 reveals that during the years of this millennium the September sea ice area is below the climatological (1981 to 2010). Hence, the years for the investigation are taken from the time period of the last ten years (2003 to 2012) detecting the years 2006 and 2009 as high ice years and 2007 and 2012 as low ice years. For these selected years the monthly averaged (July, August, September) anomaly (based on the climatology from 2003 to 2012) of the sea ice concentration provided by ERA-Interim is used to identify the spatial differences of the sea ice distributions during the high and low ice years. Additionally, the monthly averaged mean sea level pressure (mslp) anomalies of ERA-Interim are used to characterise the atmospheric circulation during the selected years with respect to the climatology (based on 1981 to 2010).

Second, for the evaluation of the HIRHAM5 its bias with respect to the ERA-Interim data set is calculated for the monthly averaged mslp and geopotential height at 500 *hPa* fields. The ensemble mean is calculated for the four ensembles and further the corresponding

ERA-Interim fields are subtracted from these ensemble mean fields.

Third, the Eady growth rate (EGR) is calculated as a measure for the strength of baroclinic instability. As mentioned in the introduction the IV is strongly related to the synoptic time scale and hence, the EGR is one measure to understand and explain the physical processes and results, since the most important contributions for the generation and reduction of IV are related to baroclinicity.

Eady [1949] developed the Eady model of baroclinic instability to understand its process. This model is based on a linearised baroclinic instability equation assuming an incompressible fluid. The EGR was defined by Lindzen and Farrell [1980] and is a measure for the maximum growth of instability and therefore describes the cyclone growth [Paciorek et al., 2002]. In the following the EGR provided by Hoskins and Valdes [1990] is applied:

$$\sigma = 0.31 \cdot \frac{f}{N} \cdot \left| \frac{\delta(u, v)}{\delta z} \right|. \quad (3.1)$$

u and v are the horizontal wind fields, z is the geopotential height and $\frac{\delta(u, v)}{\delta z}$ is the vertical wind shear. f is the Coriolis parameter and $N = \sqrt{\frac{g}{\theta} \cdot \frac{\partial \theta}{\partial z}}$ the Brunt-Väisälä frequency with θ the potential temperature and g the acceleration due to gravity. Hence, the EGR is defined by the vertical wind shear and the vertical stratification of the atmosphere.

Near the surface the EGR is dominated by the Brunt-Väisälä frequency [Hoskins and Valdes, 1990]. Therefore, they recommended an application of the EGR above 780 hPa (~ 2 km), because in this height the EGR is dominated by the vertical wind shear, which is more important for the baroclinic instability than the Brunt-Väisälä frequency. However, Hoskins and Valdes [1990] argued, that at high latitudes the variations of the Brunt-Väisälä frequency are important.

To analyse the potential of baroclinic instability in this study the EGR is calculated between the geopotential heights at 850 hPa and at 500 hPa. However, high orography (Greenland in this studied area) has still an influence on the EGR. That has to be considered in the interpretation of the results.

Hoskins and Valdes [1990] used climatological data of the winter season, Paciorek et al. [2002], Serreze and Barrett [2008], Jaiser et al. [2012] used daily data and Rinke et al. [2013] used monthly data for the calculation of the EGR. However, in this work the EGR is calculated with the six-hourly data of the HIRHAM5 simulations. Simmonds and Lim [2009] pointed out that it is advantageous to use six-hourly data of the atmospheric state compared to daily or monthly averaged values for calculating the EGR. The EGR is of a non-linear character and therefore, should be calculated with instantaneous atmospheric conditions followed by averaging the EGR for the mean state, instead of using already averaged atmospheric variables.

3.2 Internal Variability (IV)

As a first study, this work describes and analyses the IV generated within the HIRHAM5 using ensemble simulations (Chapter 5). The IV is the capability of RCMs to generate different realisation for simulations that vary in their IC [von Storch, 2005], illustrating the spread between the ensemble members [Alexandru et al., 2007]. Hence, the IV is estimated by calculating the across-member standard deviation and the across-member variance. The IV is analysed for the atmospheric circulation fields mslp and geopotential height by using the across-member standard deviation $\sqrt{\sigma_\varphi^2}$ resulting from the across-member variance (Eq. 3.4). The IV of the mslp and the geopotential height is shown as the across-member spread around the temporal evolution of the ensemble mean and as spatial distributions using contour lines (see Sec. 5.1).

The across-member variance (Eq. 3.4) is used for estimating the IV of the potential temperature (see Sec. 5.2). It is a necessary input for the diagnostic budget study of potential temperature IV (see Sec. 3.3.1) to determine the dynamical and diabatic contributions to the IV tendency (Chapter 6).

The calculation of the potential temperature IV is shown in Eq. 3.5. Its derivation uses the Reynolds decomposition (see Appendix, Eq. A.1) meaning that a variable φ can be decomposed in the ensemble mean ($\langle\varphi\rangle$) and in the deviation of each member n from the ensemble mean (φ'_n):

$$\varphi_n = \langle\varphi\rangle + \varphi'_n. \quad (3.2)$$

The ensemble mean of N ensemble members is calculated with:

$$\langle\varphi\rangle = \frac{1}{N} \sum_{n=1}^N \varphi_n. \quad (3.3)$$

The IV is defined as the across-member variance σ_φ^2 of the variable φ_n . Approximately the across-member variance can be assumed as the mean of the deviation square:

$$\sigma_\varphi^2 \approx \frac{1}{N} \sum_{n=1}^N \varphi_n'^2 \equiv \langle\varphi_n'^2\rangle. \quad (3.4)$$

Hence, the specification of the variable φ as the potential temperature $\theta = T \cdot \left(\frac{p_0}{p}\right)^\kappa$ (with temperature T , pressure p , the standard pressure $p_0 = 1000 \text{ hPa}$ and the constant $\kappa = \frac{R_L}{c_p}$ that is the quotient estimated from the gas constant for dry air $R_L = 287.058 \text{ J/(kg} \cdot \text{K)}$ over the specific heat capacity for dry air at a constant pressure $c_p = 1004 \text{ J/(kg} \cdot \text{K)}$) leads

to the IV equation of potential temperature:

$$\sigma_{\theta}^2 \approx \frac{1}{N} \sum_{n=1}^N \theta_n'^2 \equiv \langle \theta_n'^2 \rangle. \quad (3.5)$$

This IV of potential temperature (Eq. 3.5) is used for Eq. 3.28 to develop the potential temperature IV tendency.

The potential temperature IV of the HIRHAM5 is calculated with the six-hourly temperature data T , that has been converted into the potential temperature.

The IV of the potential temperature is shown as temporal and domain averaged vertical profile, as vertical and domain averaged temporal evolution and as vertical and temporal averaged spatial distribution. To avoid incorrect values over the mountainous regions within the lower pressure levels, these fields are masked out in the grid cells of those pressure levels that are affected by the orography. Due to the same lateral boundary forcing for all ensemble members the across-member variance is very small within the boundary zone. Therefore, values in the lateral boundary zone are neglected. Additionally, the patterns of the spatial distributions are graphically smoothed using a running mean over 11x11 successive grid points to allow an easier interpretation.

3.3 Diagnostic Budget Study for IV Processes

The dynamical and diabatic origin of IV are analysed and quantified with the diagnostic budget study for potential temperature and the relative vorticity (developed by Nikiema and Laprise [2010] and Nikiema and Laprise [2011]). For this study it will paid attention only to the potential temperature. The potential temperature ($\theta = t \cdot \left(\frac{p_0}{p}\right)^{\kappa}$) is defined as the temperature that a dry air parcel with the pressure p obtains by bringing this air parcel adiabatically to the standard pressure p_0 . The potential temperature is used for the diagnostic budget study of the potential temperature IV, because it enables the application of the first law of thermodynamic (Eq. 3.6) and it is an important atmospheric variable concerning the static stability.

3.3.1 Budget Equation for Potential Temperature IV

For the derivation of the diagnostic budget study for potential temperature in an ensemble of N members the initial equation is the first law of thermodynamics for the potential temperature:

$$\frac{d\theta_n}{dt} \equiv \frac{\partial\theta_n}{\partial t} + \vec{V}_n \cdot \vec{\nabla}\theta_n + \omega_n \frac{\partial\theta_n}{\partial p} = J_n \quad (3.6)$$

with the horizontal wind \vec{V}_n , the vertical motion ω_n and the total source and sink term J_n combining the radiative heating, vertical diffusion heating, condensative heating and the convective heating rates as contributions to the source and sink term.

Then, the mass-continuity $\vec{\nabla} \cdot \vec{V} + \frac{\partial \omega}{\partial p} = 0$ multiplied by θ_n and added to Eq. 3.6 leads to:

$$\frac{d\theta_n}{dt} \equiv \frac{\partial \theta_n}{\partial t} + \vec{V}_n \cdot \vec{\nabla} \theta_n + \theta \vec{\nabla} \cdot \vec{V} + \omega_n \frac{\partial \theta_n}{\partial p} + \theta \frac{\partial \omega}{\partial p} = J_n \quad (3.7)$$

By using the $\vec{\nabla}$ -rule (see Appendix, Eq. A.6) the first law of thermodynamics in combination with the mass-continuity equation (Eq. 3.7) yields to Eq. 3.6 in flux form:

$$\frac{\partial \theta_n}{\partial t} + \vec{\nabla} \cdot (\theta_n \vec{V}_n) + \frac{\partial (\theta_n \omega_n)}{\partial p} = J_n. \quad (3.8)$$

By applying the ensemble mean operator (Reynolds decomposition (see Appendix A.1)) to Eq. 3.8,

$$\frac{\partial \langle \theta \rangle}{\partial t} + \vec{\nabla} \cdot \langle \theta \vec{V} \rangle + \frac{\partial \langle \theta \omega \rangle}{\partial p} = \langle J \rangle \quad (3.9)$$

is obtained for the ensemble mean and the deviation from the ensemble mean of Eq. 3.8 is:

$$\frac{\partial \theta'_n}{\partial t} + \vec{\nabla} \cdot (\theta_n \vec{V}_n - \langle \theta \vec{V} \rangle) + \frac{\partial (\theta_n \omega_n - \langle \theta \omega \rangle)}{\partial p} = J'_n. \quad (3.10)$$

By applying the Reynolds decomposition (see Appendix, Eq. A.1) to the potential temperature

$$\theta_n = \langle \theta \rangle + \theta'_n \quad (3.11)$$

and the horizontal wind vector

$$\vec{V}_n = \langle \vec{V} \rangle + \vec{V}'_n \quad (3.12)$$

the second term of the left-hand side in Eq. 3.10 can be written as

$$\theta_n \vec{V}_n = \langle \theta \rangle \langle \vec{V} \rangle + \langle \theta \rangle \vec{V}'_n + \theta'_n \langle \vec{V} \rangle + \theta'_n \vec{V}'_n \quad (3.13)$$

and

$$\langle \theta \vec{V} \rangle = \langle \langle \theta \rangle \langle \vec{V} \rangle \rangle + \langle \langle \theta \rangle \vec{V}'_n \rangle + \langle \theta'_n \langle \vec{V} \rangle \rangle + \langle \theta'_n \vec{V}'_n \rangle. \quad (3.14)$$

With the Reynolds postulate (see Appendix, Eq. A.5) the second and third term on the right-hand side of Eq. 3.14 are zero. Hence, the second term on the left-hand side of Eq. 3.10 can be expressed as a combination of Eq. 3.13 and Eq. 3.14:

$$\theta_n \vec{V}_n - \langle \theta \vec{V} \rangle = \langle \theta \rangle \vec{V}'_n + \theta'_n \langle \vec{V} \rangle + \theta'_n \vec{V}'_n - \langle \theta'_n \vec{V}'_n \rangle. \quad (3.15)$$

The same method is applied for the third term on the left-hand side of Eq. 3.10. Hence, Eq. 3.10 can be formulated as follows:

$$\frac{\partial \theta'_n}{\partial t} + \vec{\nabla} \cdot \left(\langle \theta \rangle \vec{V}'_n + \theta'_n \langle \vec{V} \rangle + \theta'_n \vec{V}'_n - \langle \theta'_n \vec{V}'_n \rangle \right) + \frac{\partial}{\partial p} \left(\langle \theta \rangle \omega'_n + \theta'_n \langle \omega \rangle + \theta'_n \omega'_n - \langle \theta'_n \omega'_n \rangle \right) = J'_n. \quad (3.16)$$

Applying the $\vec{\nabla}$ -rule (see Appendix, Eq. A.6) for multiplying $\vec{\nabla}$ and $\frac{\partial}{\partial p}$ with the terms within the brackets of Eq. 3.16, leads to the following expression of the prognostic equation of potential temperature deviation:

$$\begin{aligned} \frac{\partial \theta'_n}{\partial t} + \langle \theta \rangle \vec{\nabla} \cdot \vec{V}'_n + \vec{V}'_n \cdot \vec{\nabla} \langle \theta \rangle + \theta'_n \vec{\nabla} \cdot \langle \vec{V} \rangle + \langle \vec{V} \rangle \cdot \vec{\nabla} \theta'_n + \vec{\nabla} \cdot \left(\theta'_n \vec{V}'_n - \langle \theta'_n \vec{V}'_n \rangle \right) \\ + \langle \theta \rangle \frac{\partial \omega'_n}{\partial p} + \omega'_n \frac{\partial \langle \theta \rangle}{\partial p} + \theta'_n \frac{\partial \langle \omega \rangle}{\partial p} + \langle \omega \rangle \frac{\partial \theta'_n}{\partial p} + \frac{\partial}{\partial p} \left(\theta'_n \omega'_n - \langle \theta'_n \omega'_n \rangle \right) = J'_n \end{aligned} \quad (3.17)$$

Due to the mass-continuity equation for a pressure-coordinate system $\vec{\nabla}_h \cdot \vec{v}_h = -\frac{\partial \omega}{\partial p}$ two terms for the ensemble mean part and the deviation part of Eq. 3.17 are zero:

$$\begin{aligned} \theta'_n \vec{\nabla} \cdot \langle \vec{V} \rangle + \theta'_n \frac{\partial \langle \omega \rangle}{\partial p} &= 0 \\ \langle \theta \rangle \vec{\nabla} \cdot \vec{V}'_n + \langle \theta \rangle \frac{\partial \omega'_n}{\partial p} &= 0. \end{aligned} \quad (3.18)$$

Using the preceding equation, Eq. 3.17 changes to:

$$\begin{aligned} \frac{\partial \theta'_n}{\partial t} + \vec{V}'_n \cdot \vec{\nabla} \langle \theta \rangle + \langle \vec{V} \rangle \cdot \vec{\nabla} \theta'_n + \vec{\nabla} \cdot \left(\theta'_n \vec{V}'_n - \langle \theta'_n \vec{V}'_n \rangle \right) \\ + \omega'_n \frac{\partial \langle \theta \rangle}{\partial p} + \langle \omega \rangle \frac{\partial \theta'_n}{\partial p} + \frac{\partial}{\partial p} \left(\theta'_n \omega'_n - \langle \theta'_n \omega'_n \rangle \right) = J'_n. \end{aligned} \quad (3.19)$$

The application of the Euler decomposition (see Appendix, Eq. A.7) to Eq. 3.19 leads to the expression:

$$\begin{aligned} \frac{D \theta'_n}{Dt} \equiv \frac{\partial \theta'_n}{\partial t} + \langle \vec{V} \rangle \cdot \vec{\nabla} \theta'_n + \langle \omega \rangle \frac{\partial \theta'_n}{\partial p} = -\vec{V}'_n \cdot \vec{\nabla} \langle \theta \rangle - \omega'_n \frac{\partial \langle \theta \rangle}{\partial p} \\ - \vec{\nabla} \cdot \left(\theta'_n \vec{V}'_n - \langle \theta'_n \vec{V}'_n \rangle \right) - \frac{\partial}{\partial p} \left(\theta'_n \omega'_n - \langle \theta'_n \omega'_n \rangle \right) + J'_n. \end{aligned} \quad (3.20)$$

It follows the multiplication of Eq. 3.20 with θ'_n :

$$\begin{aligned}
 \frac{D\theta'_n}{Dt} \cdot \theta'_n &\equiv \left(\frac{\partial \theta'_n}{\partial t} \right) \cdot \theta'_n + \langle \vec{V} \rangle \cdot \left(\vec{\nabla} \theta'_n \right) \cdot \theta'_n + \langle \omega \rangle \left(\frac{\partial \theta'_n}{\partial p} \right) \theta'_n \\
 &= -\theta'_n \vec{V}'_n \cdot \vec{\nabla} \langle \theta \rangle - \theta'_n \omega'_n \frac{\partial \langle \theta \rangle}{\partial p} - \theta'_n \left[\vec{\nabla} \cdot \left(\theta'_n \vec{V}'_n - \langle \theta'_n \vec{V}'_n \rangle \right) - \frac{\partial}{\partial p} (\theta'_n \omega'_n - \langle \theta'_n \omega'_n \rangle) \right] + \theta'_n J'_n.
 \end{aligned} \tag{3.21}$$

Now, the $\vec{\nabla}$ -rules (see Appendix, Eq. A.6) has to be applied on each term of the left-hand-side. This is shown for the first term and the others are terms are calculated analogously:

$$\left(\frac{\partial \theta'_n}{\partial t} \right) \cdot \theta'_n = \frac{\partial}{\partial t} (\theta'_n \cdot \theta'_n) - \frac{\partial \theta'_n}{\partial t} \cdot \theta'_n. \tag{3.22}$$

The transformation with adding $\frac{\partial \theta'_n}{\partial t} \cdot \theta'_n$ leads to:

$$\begin{aligned}
 2 \left(\frac{\partial \theta'_n}{\partial t} \cdot \theta'_n \right) &= \frac{\partial}{\partial t} (\theta'_n \cdot \theta'_n) \\
 &= \frac{\partial \theta_n'^2}{\partial t}.
 \end{aligned} \tag{3.23}$$

Due to the division by 2 the expression of the first term of the left-hand side of Eq. 3.21 can be replaced by $\frac{\partial}{\partial t} \left[\frac{\theta_n'^2}{2} \right]$.

These three steps are applied for each term on the left-hand side of Eq. 3.21, leading to:

$$\begin{aligned}
 \frac{1}{2} \frac{D\theta_n'^2}{Dt} &\equiv \frac{\partial}{\partial t} \left[\frac{\theta_n'^2}{2} \right] + \frac{\langle \vec{V} \rangle}{2} \cdot \vec{\nabla} \theta_n'^2 + \frac{\langle \omega \rangle}{2} \frac{\partial \theta_n'^2}{\partial p} = -\theta'_n \vec{V}'_n \cdot \vec{\nabla} \langle \theta \rangle - \theta'_n \omega'_n \frac{\partial \langle \theta \rangle}{\partial p} \\
 &\quad - \theta'_n \left[\vec{\nabla} \cdot \left(\theta'_n \vec{V}'_n - \langle \theta'_n \vec{V}'_n \rangle \right) - \frac{\partial}{\partial p} (\theta'_n \omega'_n - \langle \theta'_n \omega'_n \rangle) \right] \\
 &\quad + \theta'_n J'_n.
 \end{aligned} \tag{3.24}$$

Again, an ensemble averaging is applied on Eq. 3.24:

$$\begin{aligned}
 \frac{1}{2} \frac{D \langle \theta_n'^2 \rangle}{Dt} &\equiv \frac{\partial}{\partial t} \left[\frac{\langle \theta_n'^2 \rangle}{2} \right] + \frac{\langle \vec{V} \rangle}{2} \cdot \vec{\nabla} \langle \theta_n'^2 \rangle + \frac{\langle \omega \rangle}{2} \frac{\partial \langle \theta_n'^2 \rangle}{\partial p} \\
 &= -\langle \theta'_n \vec{V}'_n \rangle \cdot \vec{\nabla} \langle \theta \rangle - \langle \theta'_n \omega'_n \rangle \frac{\partial \langle \theta \rangle}{\partial p} - \underbrace{\left\langle \theta'_n \vec{\nabla} \cdot \left(\theta'_n \vec{V}'_n - \langle \theta'_n \vec{V}'_n \rangle \right) + \theta'_n \frac{\partial}{\partial p} (\theta'_n \omega'_n - \langle \theta'_n \omega'_n \rangle) \right\rangle}_{\text{third-order terms (T.-O. T.)}} \\
 &\quad + \langle \theta'_n J'_n \rangle.
 \end{aligned} \tag{3.25}$$

Applying the Reynolds postulate (see Appendix, Eq. A.5) on the third-order terms leads to:

$$\begin{aligned}
 T. - O. T &= \left\langle \theta'_n \vec{\nabla} \cdot (\theta'_n \vec{V}'_n) - \theta'_n \vec{\nabla} \cdot \langle \theta'_n \vec{V}'_n \rangle + \theta'_n \frac{\partial}{\partial p} (\theta'_n \omega'_n) - \theta'_n \frac{\partial}{\partial p} \langle \theta'_n \omega'_n \rangle \right\rangle \\
 T. - O. T &= \underbrace{\left\langle \theta'_n \vec{\nabla} \cdot (\theta'_n \vec{V}'_n) \right\rangle}_{\text{Reynolds term}} - \underbrace{\left\langle \theta'_n \vec{\nabla} \cdot \langle \theta'_n \vec{V}'_n \rangle \right\rangle}_{=0} + \underbrace{\left\langle \theta'_n \frac{\partial}{\partial p} (\theta'_n \omega'_n) \right\rangle}_{\text{Reynolds term}} - \underbrace{\left\langle \theta'_n \frac{\partial}{\partial p} \langle \theta'_n \omega'_n \rangle \right\rangle}_{=0}. \quad (3.26)
 \end{aligned}$$

Hence, Eq. 3.25 changes to:

$$\begin{aligned}
 \frac{1}{2} \frac{D \langle \theta_n'^2 \rangle}{Dt} &\equiv \frac{\partial}{\partial t} \left[\frac{\langle \theta_n'^2 \rangle}{2} \right] + \frac{\langle \vec{V} \rangle}{2} \cdot \vec{\nabla} \langle \theta_n'^2 \rangle + \frac{\langle \omega \rangle}{2} \frac{\partial \langle \theta_n'^2 \rangle}{\partial p} \\
 &= - \left\langle \theta'_n \vec{V}'_n \right\rangle \cdot \vec{\nabla} \langle \theta \rangle - \langle \theta'_n \omega'_n \rangle \frac{\partial \langle \theta \rangle}{\partial p} - \left\langle \theta'_n \vec{\nabla} \cdot (\theta'_n \vec{V}'_n) \right\rangle - \left\langle \theta'_n \frac{\partial}{\partial p} (\theta'_n \omega'_n) \right\rangle + \langle \theta'_n J'_n \rangle. \quad (3.27)
 \end{aligned}$$

With the approach of Eq. 3.5, the $\langle \theta_n'^2 \rangle$ in Eq. 3.27 can be replaced by the IV of potential temperature meaning the across-member variance of potential temperature (σ_θ^2). Hence, the prognostic equation for potential temperature variance is obtained:

$$\begin{aligned}
 \frac{1}{2} \frac{D \sigma_\theta^2}{Dt} &\equiv \frac{\partial}{\partial t} \left[\frac{\sigma_\theta^2}{2} \right] + \langle \vec{V} \rangle \cdot \vec{\nabla} \frac{\sigma_\theta^2}{2} + \langle \omega \rangle \frac{\partial}{\partial p} \left[\frac{\sigma_\theta^2}{2} \right] \\
 &= - \left\langle \theta'_n \vec{V}'_n \right\rangle \cdot \vec{\nabla} \langle \theta \rangle - \langle \theta'_n \omega'_n \rangle \frac{\partial \langle \theta \rangle}{\partial p} - \left\langle \theta'_n \vec{\nabla} \cdot (\theta'_n \vec{V}'_n) \right\rangle - \left\langle \theta'_n \frac{\partial}{\partial p} (\theta'_n \omega'_n) \right\rangle + \langle \theta'_n J'_n \rangle. \quad (3.28)
 \end{aligned}$$

To further develop the diagnostic potential temperature IV tendency in flux form, the last step is the calculation of:

$$\left[(Eq. 3.28) + \frac{1}{2} \sigma_\theta^2 \underbrace{\left(\langle \vec{\nabla} \cdot \langle \vec{V} \rangle \rangle + \frac{\partial \langle \omega \rangle}{\partial p} = 0 \right)}_{\text{mass-continuity equation}} \right]. \quad (3.29)$$

Therefore, the left-hand side of the mass-continuity equation and Eq. 3.28 and the right-hand-sides of both equations are added, respectively:

$$\begin{aligned}
 & \frac{1}{2}\sigma_\theta^2 \left(\vec{\nabla} \cdot \langle \vec{V} \rangle + \frac{\partial \langle \omega \rangle}{\partial p} \right) = 0 \\
 & + \frac{\partial}{\partial t} \left[\frac{\sigma_\theta^2}{2} \right] + \langle \vec{V} \rangle \cdot \vec{\nabla} \frac{\sigma_\theta^2}{2} + \langle \omega \rangle \frac{\partial}{\partial p} \left[\frac{\sigma_\theta^2}{2} \right] = \dots
 \end{aligned} \tag{3.30}$$

$$\frac{\partial}{\partial t} \left[\frac{\sigma_\theta^2}{2} \right] + \underbrace{\langle \vec{V} \rangle \cdot \vec{\nabla} \frac{\sigma_\theta^2}{2} + \frac{1}{2}\sigma_\theta^2 \vec{\nabla} \cdot \langle \vec{V} \rangle}_{\bar{\text{I}}} + \underbrace{\langle \omega \rangle \frac{\partial}{\partial p} \left[\frac{\sigma_\theta^2}{2} \right] + \frac{1}{2}\sigma_\theta^2 \frac{\partial \langle \omega \rangle}{\partial p}}_{\bar{\text{II}}} = \dots$$

By applying the $\vec{\nabla}$ -rule (see Appendix, Eq. A.6) on $\bar{\text{I}}$ it follows:

$$\begin{aligned}
 \langle \vec{V} \rangle \cdot \vec{\nabla} \frac{\sigma_\theta^2}{2} + \frac{1}{2}\sigma_\theta^2 \vec{\nabla} \cdot \langle \vec{V} \rangle &= \frac{1}{2} \left(\langle \vec{V} \rangle \cdot \vec{\nabla} (\sigma_\theta^2) + \vec{\nabla} \sigma_\theta^2 \cdot \langle \vec{V} \rangle \right) \\
 &= \frac{1}{2} \left[\vec{\nabla} \cdot \left(\langle \vec{V} \rangle \sigma_\theta^2 \right) \right].
 \end{aligned} \tag{3.31}$$

The same is done for $\bar{\text{II}}$ resulting in:

$$\begin{aligned}
 \langle \omega \rangle \frac{\partial}{\partial p} \left[\frac{\sigma_\theta^2}{2} \right] + \frac{1}{2}\sigma_\theta^2 \frac{\partial \langle \omega \rangle}{\partial p} &= \frac{1}{2} \left(\langle \omega \rangle \frac{\partial}{\partial p} [\sigma_\theta^2] + \sigma_\theta^2 \frac{\partial \langle \omega \rangle}{\partial p} \right) \\
 &= \frac{1}{2} \left[\frac{\partial}{\partial p} (\langle \omega \rangle \sigma_\theta^2) \right].
 \end{aligned} \tag{3.32}$$

Hence, Eq. 3.28 can be developed to:

$$\begin{aligned}
 \frac{1}{2} \frac{D\sigma_\theta^2}{Dt} &\equiv \frac{\partial}{\partial t} \left[\frac{\sigma_\theta^2}{2} \right] + \frac{1}{2} \left[\vec{\nabla} \cdot \left(\langle \vec{V} \rangle \sigma_\theta^2 \right) \right] + \frac{1}{2} \left[\frac{\partial (\langle \omega \rangle \sigma_\theta^2)}{\partial p} \right] \\
 &= - \left\langle \theta'_n \vec{V}'_n \right\rangle \cdot \vec{\nabla} \langle \theta \rangle - \langle \theta'_n \omega'_n \rangle \frac{\partial \langle \theta \rangle}{\partial p} - \left\langle \theta'_n \vec{\nabla} \cdot \left(\theta'_n \vec{V}'_n \right) \right\rangle - \left\langle \theta'_n \frac{\partial}{\partial p} (\theta'_n \omega'_n) \right\rangle + \langle \theta'_n J'_n \rangle.
 \end{aligned} \tag{3.33}$$

Multiplying Eq. 3.33 by a factor 2 and transforming the equation leads to Eq. 3.34, the diagnostic potential temperature IV tendency (left-hand side L_θ) and its contributions (right-hand side R_θ).

$$\begin{aligned}
 \frac{\partial \sigma_\theta^2}{\partial t} &= - \vec{\nabla} \cdot \left(\langle \vec{V} \rangle \sigma_\theta^2 \right) - \frac{\partial (\langle \omega \rangle \sigma_\theta^2)}{\partial p} - 2 \left\langle \theta'_n \vec{V}'_n \right\rangle \cdot \vec{\nabla} \langle \theta \rangle - 2 \langle \theta'_n \omega'_n \rangle \frac{\partial \langle \theta \rangle}{\partial p} \\
 &\quad - 2 \left\langle \theta'_n \vec{\nabla} \cdot \left(\theta'_n \vec{V}'_n \right) \right\rangle - 2 \left\langle \theta'_n \frac{\partial}{\partial p} (\theta'_n \omega'_n) \right\rangle + 2 \langle \theta'_n J'_n \rangle
 \end{aligned} \tag{3.34}$$

Eq. 3.34 has seven terms contributing to the IV tendency. To shorten Eq. 3.34 each contribution term is defined and summarised by a symbolic letter:

$$L_\theta = R_\theta = A_h + A_v + B_h + B_v + C + E_h + E_v \quad (3.35)$$

with the diagnostic tendency of potential temperature IV:

$$L_\theta = \frac{\partial \sigma_\theta^2}{\partial t} \quad (3.36)$$

the horizontal transport term:

$$A_h = -\vec{\nabla} \cdot \left(\langle \vec{V} \rangle \sigma_\theta^2 \right) \quad (3.37)$$

the vertical transport term:

$$A_v = -\frac{\partial \left(\langle \omega \rangle \sigma_\theta^2 \right)}{\partial p} \quad (3.38)$$

the horizontal 'baroclinic' term:

$$B_h = -2 \left\langle \theta'_n \vec{V}'_n \right\rangle \cdot \vec{\nabla} \langle \theta \rangle \quad (3.39)$$

the vertical 'baroclinic' term:

$$B_v = -2 \left\langle \theta'_n \omega'_n \right\rangle \frac{\partial \langle \theta \rangle}{\partial p} \quad (3.40)$$

the diabatic source and sink term:

$$C = 2 \left\langle \theta'_n J'_n \right\rangle \quad (3.41)$$

the horizontal third-order term:

$$E_h = -2 \left\langle \theta'_n \vec{\nabla} \cdot \left(\theta'_n \vec{V}'_n \right) \right\rangle \quad (3.42)$$

the vertical third-order term:

$$E_v = -2 \left\langle \theta'_n \frac{\partial}{\partial p} \left(\theta'_n \omega'_n \right) \right\rangle. \quad (3.43)$$

With these seven terms the dynamical and diabatic contributions to a generation and a reduction of the IV of potential temperature can be quantified.

3.3.2 Explanation of the Contribution Terms

For the calculation of each of the seven contributions to the diagnostic potential temperature IV tendency (L_θ) the six-hourly temporal evolution of the HIRHAM5 output (saved on 19 pressure levels) is used. The input variables of the budget study are the temperature T (for the calculation of the potential temperature θ), both horizontal and the vertical wind components u and v and the temperature tendencies due to radiation, convection, condensation and vertical diffusion (summarised in J of the first law of thermodynamic for potential temperature (Eq. 3.6)).

The seven particular contributions of Eq. 3.35 describe different atmospheric processes which are defined in Nikiema and Laprise [2010] and explained here again. All of these terms contribute to the IV tendency of potential temperature L_θ , meaning the temporal derivation of the across-member variance of the potential temperature (Eq. 3.36). Therefore, the terms that have positive values illustrate a contribution to a generation or production of IV tendency, while contributions with negative values reduce the IV tendency. Hence, due to the different contribution terms, there are various physical interpretations of the influence on the IV tendency. The terms A_h (Eq. 3.37) and A_v (Eq. 3.38) are the horizontal and vertical transport terms of potential temperature IV by the ensemble mean flow. They indicate the horizontal displacement of the IV (across-member variance, σ_θ^2) by the ensemble mean flow, resulting in negative and positive values meaning the direction of the IV's transport within the integration area. Besides, when IV is transported out of the model domain A_h and A_v contribute negatively to the IV tendency. The other way around, both terms contribute positively to the IV tendency when IV is transported into the model domain.

The terms B_h (Eq. 3.39) and B_v (Eq. 3.40) describe the contributions to IV tendency due to the covariances of horizontal and vertical flow fluctuations and potential temperature fluctuations acting in the direction of the horizontal and vertical gradient of the ensemble mean potential temperature. They are related to baroclinic processes in the weather systems and linked to synoptic events. Therefore, they are called 'baroclinic' terms hereinafter. The positive contribution to the IV tendency due to the averaged horizontal 'baroclinic' term (B_h) entails that the covariance between the fluctuations of the potential temperature and the horizontal wind ($\langle \theta'_n \vec{V}'_n \rangle$) and the horizontal gradient of the mean potential temperature ($\vec{\nabla} \langle \theta \rangle$) have a contrary sign. Further, the multiplication by -2 leads to positive values of B_h indicating a production of IV. The ensemble mean potential temperature increases southward ($\vec{\nabla} \langle \theta \rangle < 0$). Hence, the covariance has to be positive ($\langle \theta'_n \vec{V}'_n \rangle > 0$), indicating that warm air perturbations ($\theta'_n > 0$) flows towards cold regions (northward, $\vec{V}'_n > 0$) or that cold air perturbations ($\theta'_n < 0$) flows towards warm regions (southward, $\vec{V}'_n < 0$).

This implies a motion against the horizontal gradient of the ensemble mean potential temperature ($\vec{\nabla} \langle \theta \rangle < 0$, due to the increasing potential temperatures southward), leading to a production of potential temperature IV. A reduction of IV tendency due to B_h (negative values) is found when the covariance and the ensemble mean gradient have the same sign leading to a negative contribution of B_h due to the multiplication by -2. Physically this can be explained by the motion of cold air perturbations ($\theta'_n < 0$) towards cold regions (northward, $\vec{V}'_n > 0$) and warm air deviations ($\theta'_n > 0$) towards warm regions (southward, $\vec{V}'_n < 0$). In both cases the covariance between the fluctuations of the potential temperature and the horizontal wind is negative ($\langle \theta'_n \vec{V}'_n \rangle < 0$). These fluxes are in agreement with the horizontal gradient of the ensemble mean potential temperature ($\vec{\nabla} \langle \theta \rangle < 0$) and therefore, lead to a negative contribution to the IV tendency.

The negative contribution to the IV tendency due to the averaged vertical 'baroclinic' term (Eq. 3.40) reveals, that the covariance between the potential temperature perturbation and the vertical motion perturbation ($\langle \theta'_n \omega'_n \rangle$) and the vertical gradient of the ensemble mean potential temperature ($\frac{\partial \langle \theta \rangle}{\partial p}$) have the same sign. The vertical gradient of the ensemble mean potential temperature ($\frac{\partial \langle \theta \rangle}{\partial p}$) is always negative due to the stable mean state of the atmosphere. Hence, the covariance $\langle \theta'_n \omega'_n \rangle$ has to be negative as well to obtain a negative contribution to the IV tendency, because of the multiplication by -2. Physically this implies the ascent ($\omega'_n < 0$) of warm air perturbations ($\theta'_n > 0$) and the sinking ($\omega'_n > 0$) of cold air perturbations ($\theta'_n < 0$) with respect to the ensemble mean flow. This behaviour leads to a reduction of potential temperature IV. The other way around, B_v contributes to a generation of potential temperature IV when the covariance is positive ($\langle \theta'_n \omega'_n \rangle > 0$), indicating an adiabatic rising ($\omega'_n < 0$) of cold air perturbations ($\theta'_n < 0$) or adiabatic descending ($\omega'_n > 0$) of warm air fluctuations ($\theta'_n > 0$).

C (Eq. 3.41) is the diabatic source and sink term and includes the fluctuations of the temperature tendencies due to radiation, vertical diffusion and surface sensible heat flux, condensation and convection which are summarised in J'_n . C represents the covariance between the fluctuations of the potential temperature and the diabatic heating rate ($\langle \theta'_n J'_n \rangle$). This term contributes to a generation of potential temperature IV tendency, when warm air perturbations ($\theta'_n > 0$) are heated diabatically ($J'_n > 0$). However, C reduces the IV tendency, when warm/cold fluctuations are cooled/heated diabatically. The sixth-order horizontal diffusion representing subgrid-scale processes is not considered in this budget study, because its magnitude is small with values of $-0.3 \times 10^{-5} K^2/s$ at the surface and becomes zero with increasing height.

The terms E_h (Eq. 3.42) and E_v (Eq. 3.43) are the third-order terms, describing the covariance of the potential temperature fluctuations acting upon the perturbation gradient meaning the divergence of the fluctuations flow of potential temperature.

Chapter 4

Atmospheric and Sea Ice Conditions in the Selected Summers

To get an overview of the characteristics of the Arctic conditions and the ability of the RCM HIRHAM5 to simulate the atmospheric circulation, a short evaluation of the HIRHAM5 compared with the ERA-Interim data set (Sec. 4.2) is presented. And, for a better understanding of the IV generated within the model and the dynamical and diabatic contributions to the IV tendency, this chapter presents the basic state of the Arctic atmosphere. It includes an explanation of the reasons for selecting the years 2006, 2007, 2009 and 2012 that are analysed within this work (Sec. 4.1), and the cyclonic activity simulated with HIRHAM5 (Sec. 4.3).

4.1 Examined Years for the Investigation of IV

As mentioned in the introduction (Chapter 1) the investigated time period covers the summer and early autumn season from July to September (JAS), which is characterised by intense sea ice melting. One idea of the analysis of the IV within HIRHAM5 was to look for a relationship between the IV and the sea ice cover. It is well known, that the atmospheric circulation has a strong impact on the IV within a RCM (Rinke and Dethloff [2000], Rinke et al. [2004] Alexandru et al. [2007], Lucas-Picher et al. [2008a], Nikiema and Laprise [2010] and Nikiema and Laprise [2011]). Further Nikiema and Laprise [2010] and Nikiema and Laprise [2011] examined that specific atmospheric conditions influence the IV due to dynamical processes like advection and baroclinicity and diabatic processes. Hence, it is assumed that the distribution and concentration of the sea ice could affect the IV by modifying the exchange of moisture and heat fluxes between the ocean and atmosphere. Therefore, the quantification of the IV and its dynamical and diabatic origins is determined for years with high ice conditions and years with low ice conditions in September. This

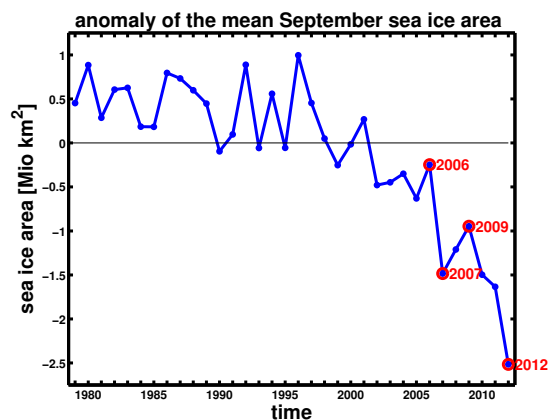


Figure 4.1: Temporal evolution of the mean September sea ice area anomaly from 1979 to 2012 provided by the ERA-Interim data set. The anomaly is calculated by subtracting the mean September sea ice area climatology (period from 1981 to 2010 like defined by NSIDC [2015]) from the mean September sea ice area. The red marked years are the analysed years within this study. The years 2007 and 2012 represent the low ice years and the years 2006 and 2009 represent the high ice years.

enables the investigation of the influence of differing atmospheric and sea ice conditions on the RCM generated IV. The selection of adequate years is based on the mean September sea ice area provided by the ERA-Interim data set from 1979 to 2012. Hence, the September sea ice anomaly is calculated by subtracting the mean September sea ice area climatology (1981 to 2010 like defined by the NSIDC [2015]) from the mean September sea ice area for each years from 1979 until 2012. These September anomalies of the sea ice area are shown in Fig. 4.1. This figure illustrates a strong negative trend of the sea ice area during the beginning of this millennium. Due to the ongoing debate concerning the current sea ice retreat only the last ten years are considered for the selection of the years with low and high ice conditions. Hence, the decision was made to use the years 2007 and 2012 representing low ice years and 2006 and 2009 representing high ice years.

For a better illustration the spatial distribution of the monthly averaged sea ice concentration is shown in Fig. 4.2. Within the model HIRHAM5 the sea ice is prescribed and the sea ice thickness is set constant to 2 m in grid cells that are covered by sea ice (see Section 2.1). Hence, the analysis based on the ERA-Interim data set that acts as driving data for the HIRHAM5. It has to be mentioned, that from January 1989 to January 2009 the sea ice concentration is set constant to 1 for all grid cells that are located north of 82.5° N [ECMWF, 2015]. The spatial distribution of the monthly mean sea ice concentration is shown in Fig. 4.2 for July to September (columns) for the high ice years 2006 and 2009 (first and second row) and the low ice years 2007 and 2012 (third and fourth row). Additionally, the spatial distribution of the September sea ice concentration anomalies for all four years are shown (Fig. 4.3) For a more clear identification of the regions with less or more sea ice during these years the anomaly is based on the ten-year climatology from 2003 to 2012. To explain the reasons of the observed sea ice distribution, concentration

4.1. EXAMINED YEARS FOR THE INVESTIGATION OF IV

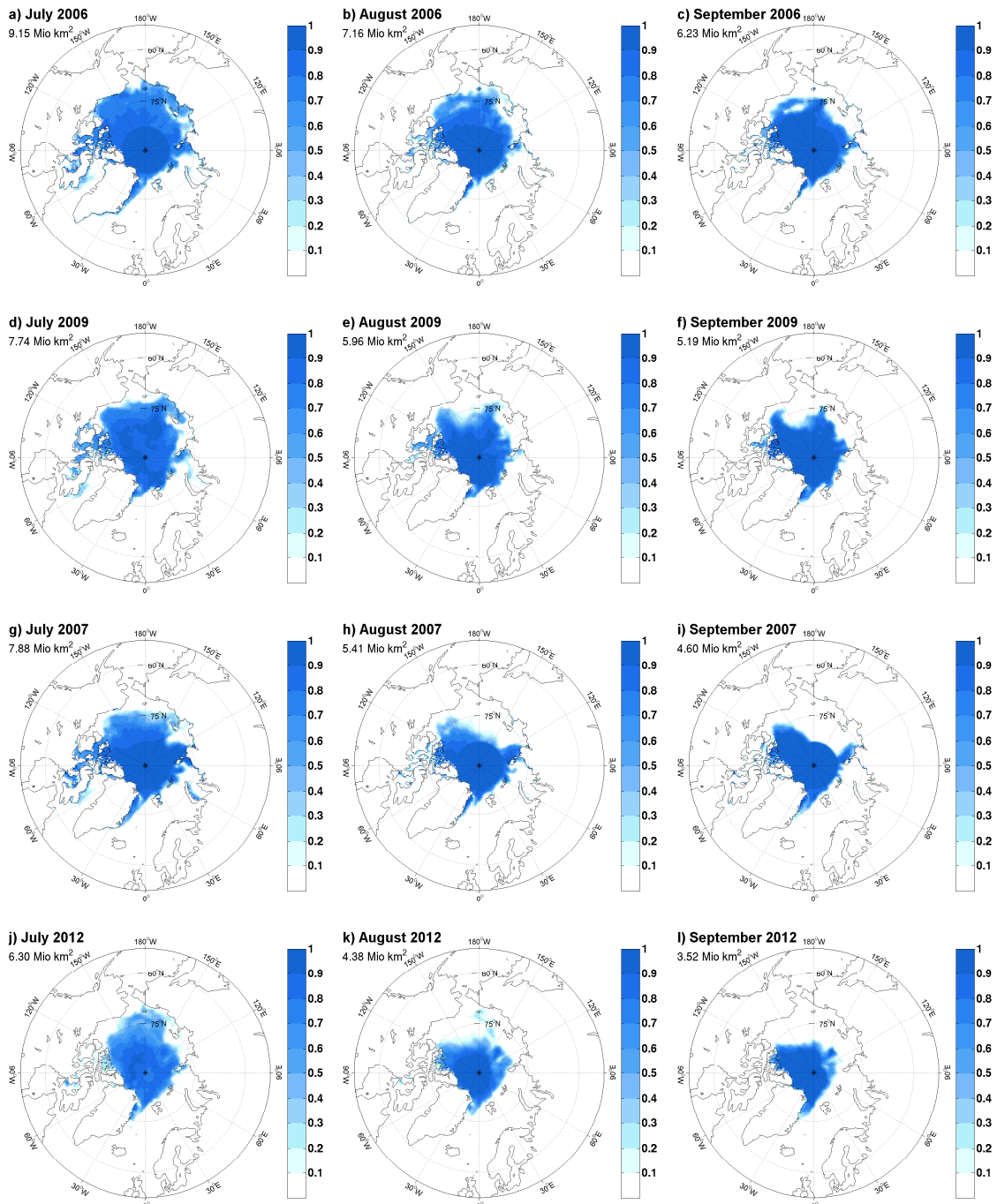


Figure 4.2: Spatial distribution of the monthly averaged sea ice concentration provided by the ERA-Interim data set for July, August and September (columns) for the high ice years 2006 and 2009 (first and second row) and the low ice years 2007 and 2012 (third and fourth row). For each month the corresponding monthly averaged sea ice extent in Mio km² is written within the figures.

and anomalies, the anomalies of the mslp provided by the ERA-Interim data set are shown as well (Fig. 4.4). The mslp anomalies base on the 30-year climatology from 1981 to 2010 and are shown as monthly averages.

The comparison of the spatial distribution of the monthly averaged sea ice concentration

during the high ice years 2006 and 2009 and the low ice years 2007 and 2012 (Fig. 4.2) reveals spatial differences. In 2006 the largest sea ice extent is obtained by ERA-Interim, with even 6.23 Mio km^2 averaged for September, whereas the NSIDC [2015] observed a mean September sea ice extent of 5.9 Mio km^2 . A strong polynya within the Beaufort Sea was detected by satellite data [NSIDC, 2015] and can be seen in the ERA-Interim data as well (Fig. 4.2 (b) and (c)). 2009 is defined as an high ice year as well, but the sea ice concentration pattern shows less sea ice in the area near 75° N between 150° W and 180° W. The anomalies of the sea ice concentration (based on the mean September climatology from 2003 to 2012) illustrate a quite similar pattern with positive anomalies in the central Arctic Ocean for both high ice years (Fig. 4.3(a), (c)). During September 2006, the strongest positive anomaly is found at the Beaufort Sea and the East Siberian Sea covering the region from 85° N to 75° N. This anomaly is less pronounced and partly negative during September 2009. The ERA-Interim mslp anomalies based on the climatology from 1981 to 2010 (Fig. 4.4) illustrate that during July 2006 the pressure reaches lower values than normal over the Beaufort Sea and from the Canada Basin over Greenland to Europe and higher values over the Laptev Sea and East Siberian Sea and Siberia and Scandinavia. That behaviour changes sharply from August, with a small but strong low pressure vortex over the central Arctic Ocean and a belt of abnormal high pressure along the coastlines and northern Europe, to September with an intense negative mslp anomaly over Eurasia and the eastern Arctic Ocean.

Compared to 2006, the mslp anomaly during 2009 reveals a high pressure over the central Arctic Ocean during July (Fig. 4.4(d)). The seasonal averaged (JAS) mslp anomaly (not shown) shows a positive dipole anomaly (DA) during 2009. This positive DA is characterised by a positive mslp anomaly over the Canadian Archipelago and negative mslp anomaly over the Barents Sea [Wang et al., 2009]. The seasonal averaged positive mslp anomaly reaches far into the Arctic Ocean due to the anomaly pattern in July 2009. In general, the positive DA results in a sea ice transport from the central Arctic Ocean into the Barents and Greenland Seas. This DA pattern is more pronounced during 2009 compared to 2006. Hence, the sea ice retreat is a little bit stronger during 2009 compared to 2006.

The mean sea ice distribution during summer 2007 and 2009 starts with almost the same sea ice extent (7.88 Mio km^2 during July 2007 and 7.74 Mio km^2 during July 2009). However, during 2007 the sea ice loss is enhanced compared to 2006 and 2009. Hence, it is defined as a low ice year. During the beginning of the summer 2007 high pressure is observed over the Arctic Ocean as well. However, 2007 is characterised by a stronger dipole pattern with low pressure over Siberia (see Fig. 5.3 (g), (h)). The anomalies clearly illustrate the mslp dipole during summer 2007 with higher pressure over the Arctic Ocean in July 2007 that further develops to a positive DA until September 2007 with high pressure over the

4.1. EXAMINED YEARS FOR THE INVESTIGATION OF IV

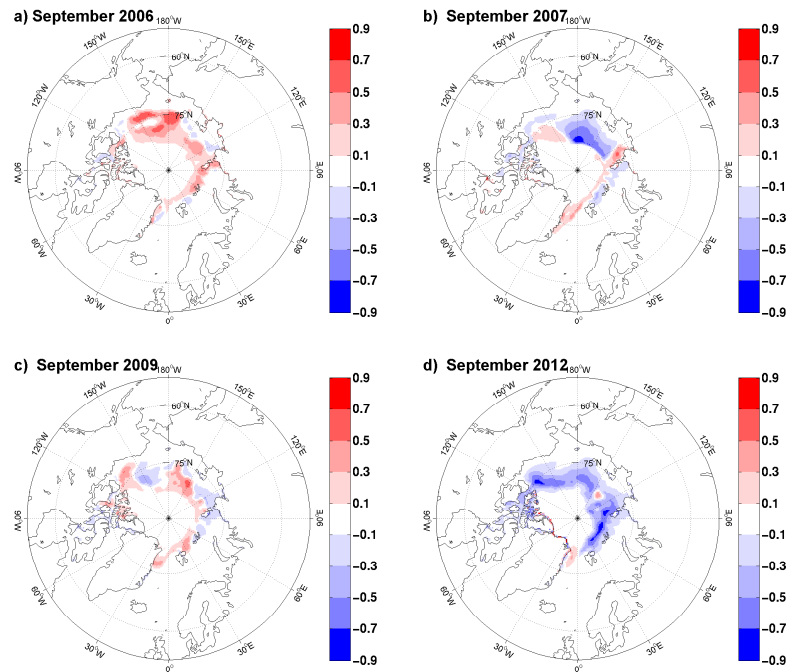


Figure 4.3: Spatial distribution of the September sea ice area anomaly provided by the ERA-Interim data set for the high ice years 2006 (a) and 2009 (c) and the low ice years 2007 (b) and 2012 (d). The anomaly is calculated by subtracting the mean September sea ice concentration climatology (period from 2003 to 2012, representing the last ten years with a successive negative mean September sea ice area anomaly visible in Fig. 4.1) from the mean September sea ice area of the four investigated years.

Canadian Archipelago, and lower pressure than normal over the Barents Sea (Fig. 4.4(third row)). This pattern of anticyclonic conditions over the central Arctic Ocean and the positive DA are responsible for a strong sea ice retreat (Dorn et al. [2012], Wang et al. [2009]). This positive DA is stronger than during 2009 and hence, leads to an intensified trans-polar drift resulting in the sea ice retreat in the Laptev and East Siberian Seas. The observed mean September sea ice extent was 4.28 Mio km^2 and the absolute minimum sea ice extent was achieved on 18th September with 4.17 Mio km^2 [NSIDC, 2015]. The mean September sea ice extent provided by the ERA-Interim data set reaches 4.6 Mio km^2 (Fig. 4.2(i)). The difference in the sea ice extent between ERA-Interim and the NSIDC in September 2007 can be explained due to the fact, that until January 2009 the sea ice concentration is set to 1 for all grid cells north of 82.5° N [ECMWF, 2015]. This can be clearly seen in Fig. 4.2(i). However, the minimum sea ice extent during 2007 is undercut during summer 2012. Then, the Laptev and Beaufort Seas are completely ice free in September compared to 2007. The anomaly of the September sea ice concentration (Fig. 4.3(d)) more clearly illustrates, that negative sea ice concentration anomalies range from the whole eastern Arctic Ocean to the Beaufort Sea. The sea ice reduction reached a new maximum in the Arctic (ERA-Interim September mean: 3.52 Mio km^2) and on 16th September the sea ice extent amounts 3.41 Mio km^2 only [NSIDC, 2015]. NSIDC [2015] argue that this is

CHAPTER 4. ATMOSPHERIC AND SEA ICE CONDITIONS IN THE SELECTED SUMMERS

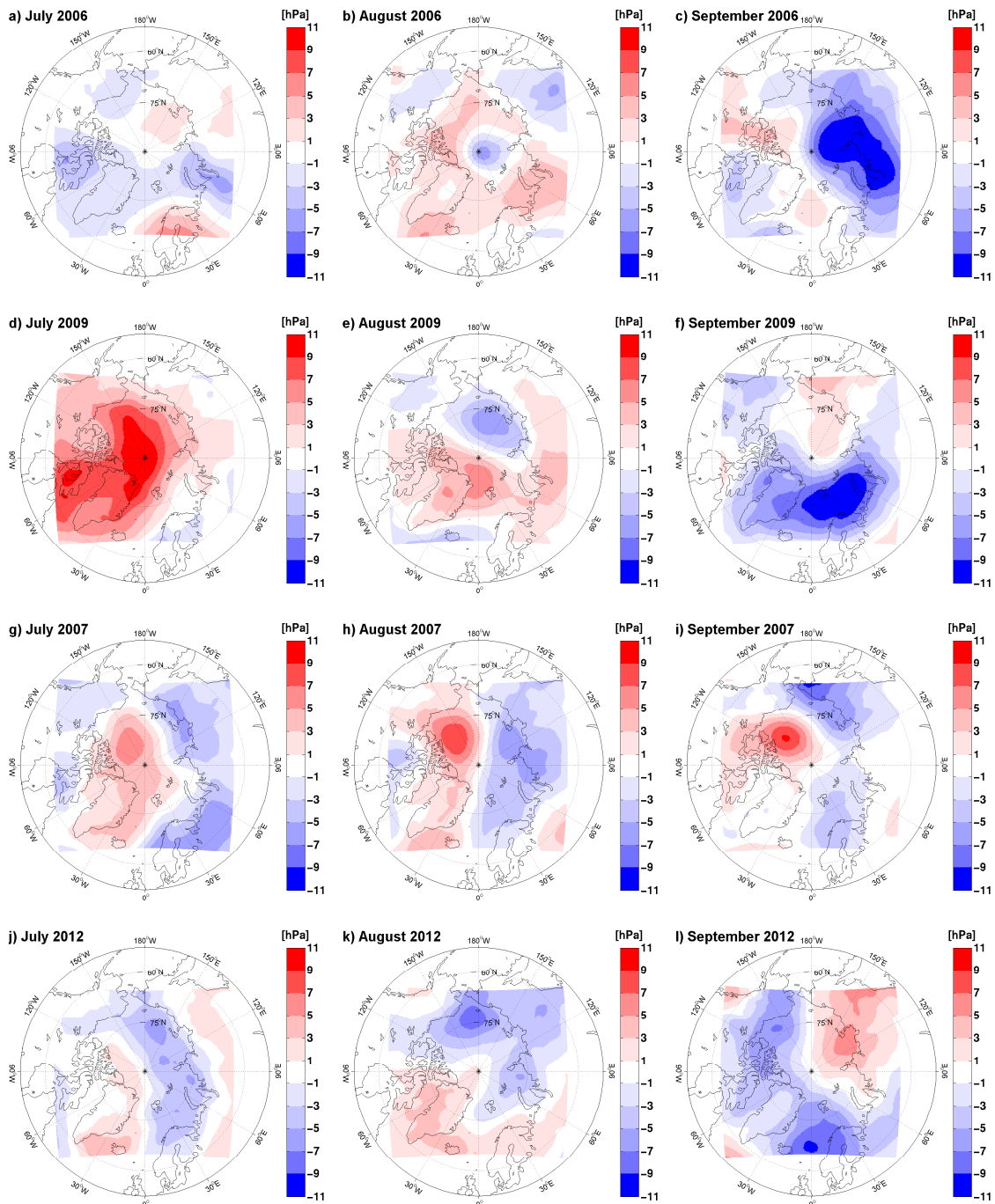


Figure 4.4: Spatial distribution of the monthly averaged mslp anomaly provided by the ERA-Interim data set for July, August and September (columns) for the high ice years 2006 and 2009 (first and second row) and the low ice years 2007 and 2012 (third and fourth row). The anomaly is calculated by subtracting the monthly mslp climatology (period from 1981 to 2010 like defined by NSIDC [2015]) from the monthly mslp of the four investigated years.

promoted due to the strong sea ice loss in June because of the warm conditions over the Arctic Ocean and Northern Eurasia and due to the high pressure over the Beaufort Sea and low pressure over Siberia, resulting in an enhanced ice transport through the Fram Strait in

June. This warm and anticyclonic conditions are often accompanied with an intense sea ice reduction during summer [Dorn et al., 2012]. However, the following months July to September are mainly characterised by a negative mslp anomaly over the Arctic Ocean. Hence, the seasonal averaged mslp anomaly (not shown) reveals a stronger low pressure circulation than usual over the Barents and Kara Seas caused by the July and September mslp anomaly (Figs. 4.4(j), (l)) and over the Beaufort Sea and Chukchi Sea caused by the July and August mslp anomaly (Figs. 4.4(j), (k)). This distinct anomalous low pressure over the Chukchi Sea and Beaufort Sea found in the ERA-Interim mslp anomaly during July and August 2012 is in agreement with the observed cyclone events during these months. Especially, the great Arctic cyclone event during the beginning of August 2012 (Simmonds and Rudeva [2012], Zhang et al. [2013], Parkinson and Comiso [2013]) leads to a strong sea ice reduction.

The special atmospheric conditions in relation with the sea ice concentration induce the decision to analyse the four selected years with the RCM HIRHAM5 and estimate and explain the IV within the HIRHAM5. In the following the year 2012 is exemplarily examined in a more detailed way compared to the other years. This is due to the fact, that during summer 2012 the maximum sea ice reduction was observed and it is the latest case of minimum sea ice extent. The results obtained for the other years will be shortly explained and if mentioned, the figures will be shown in the Appendix (Chapter A).

4.2 Evaluation of HIRHAM5

A comprehensive validation of the HIRHAM5 was given by Klaus [2014] however, they used the model set-up with nudging. Therefore, it is necessary to shortly evaluate the HIRHAM5 in this work again, because here the unnudged HIRHAM5 is applied, as explained in Sec. 2.2. This method enables the free development of each simulation without any nudging of the external forcing by the driving data within the model domain. Hence, it is obvious that the difference between the simulations and the driving data is more pronounced. The evaluation is performed for all ensembles (2006, 2007, 2009 and 2012) with the ensemble mean of the 20 HIRHAM5 simulations, respectively. However, the evaluation is shown here explicitly for 2012, whereas for the other ensemble years the bias is shown only.

The monthly mean geopotential height at 500 *hPa* simulated with HIRHAM5 and provided by the ERA-Interim data set for summer 2012 (Figs. 4.5(d) and (e) for July, Fig. 4.6(d) and (e) for August and Fig. 4.7(d) and (e) for September) reveal the circum-polar low pressure system, that intensifies from July to September. This pattern weakens with decreasing height and is only weakly pronounced in the mslp (Figs. 4.5, 4.6 and Fig. 4.7 (a) and

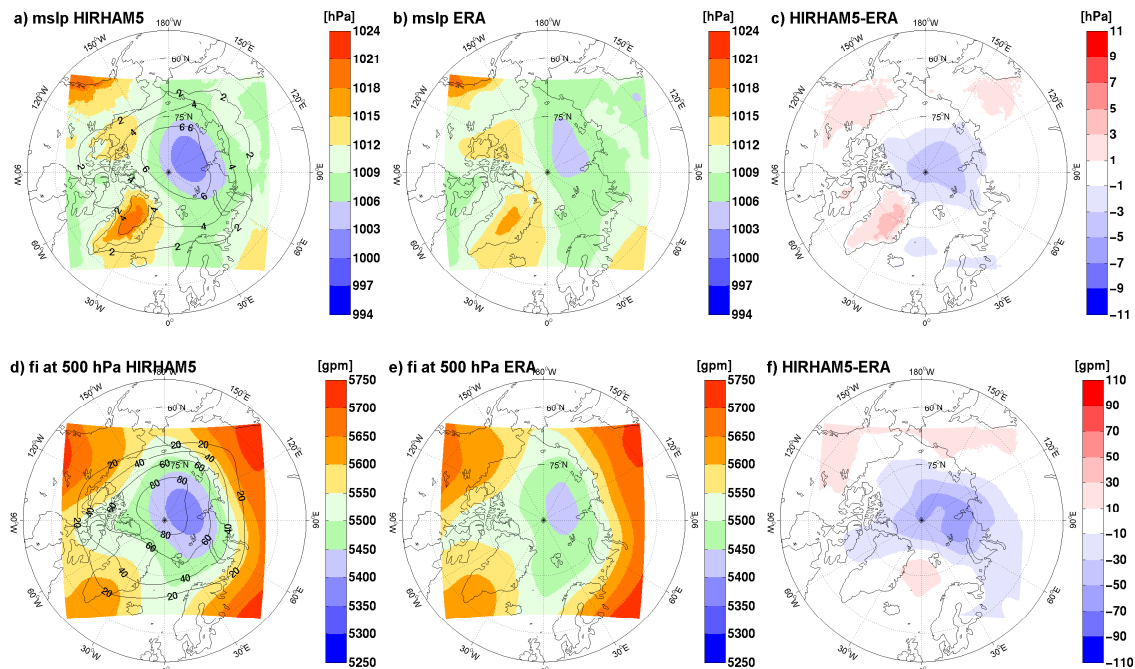


Figure 4.5: Spatial distribution of the monthly averaged July msip in hPa (first row) and the geopotential height at 500 hPa in gpm (second row) simulated with HIRHAM5 (first column), provided by ERA-Interim (second column) and the difference between ERA-Interim and HIRHAM5 (third column) for the ensemble representing the low ice year 2012. The contour lines in (a) and (d) illustrate the HIRHAM5 across-member standard deviation of the corresponding variable.

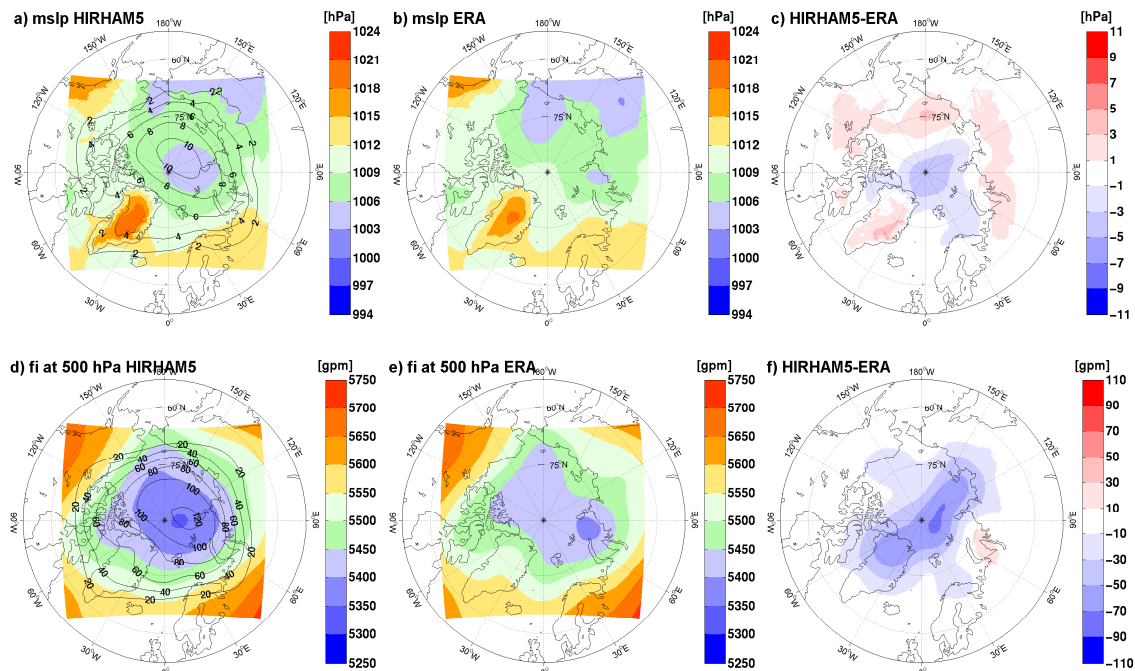


Figure 4.6: Spatial distribution of the monthly averaged August msip in hPa (first row) and the geopotential height at 500 hPa in gpm (second row) simulated with HIRHAM5 (first column), provided by ERA-Interim (second column) and the difference between ERA-Interim and HIRHAM5 (third column) for the ensemble representing the low ice year 2012. The contour lines in (a) and (d) illustrate the HIRHAM5 across-member standard deviation of the corresponding variable.

4.2. EVALUATION OF HIRHAM5

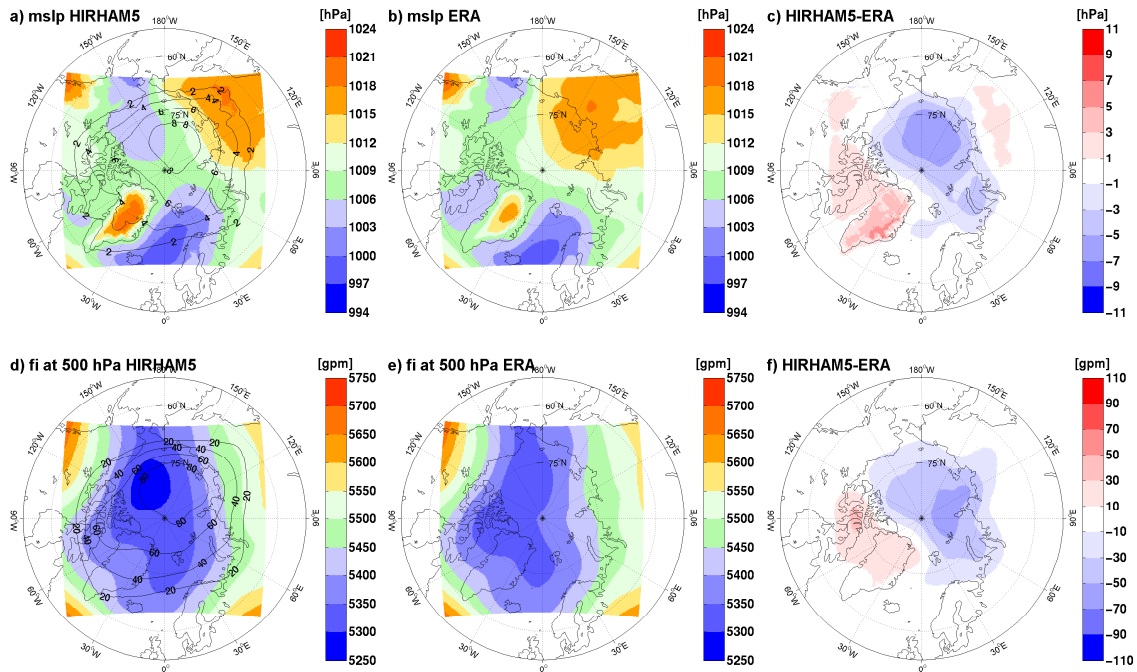


Figure 4.7: Spatial distribution of the monthly averaged September mslp in hPa (first row) and the geopotential height at 500 hPa in gpm (second row) simulated with HIRHAM5 (first column), provided by ERA-Interim (second column) and the difference between ERA-Interim and HIRHAM5 (third column) for the ensemble representing the low ice year 2012. The contour lines in (a) and (d) illustrate the HIRHAM5 cross-member standard deviation of the corresponding variable.

(b), respectively) however, with stronger pronouncement in the HIRHAM5 simulations compared to the ERA-Interim data set. The ensemble averaged monthly mean of the July mslp (Fig. 4.5(a)) shows an extensive low pressure system over the Eastern Arctic Ocean. In August it is maintained that the pressure is higher over this region and over eastern Siberia low pressure is formed (Fig. 4.6(a), (b)). In September (Fig. 4.7(a), (b)) the Icelandic Low is deepened and the Siberian High is established.

The comparison with the ERA-Interim data set shows, that HIRHAM5 systematically underestimates the monthly mean pressure over the central Arctic Ocean. Hence, HIRHAM5 tends to simulate an excessive low pressure system, especially for the mslp during September 2012 and the geopotential height at 500 hPa during August 2012. However, during August 2012 a positive bias is found in the mslp difference (Fig. 4.6(c)) ranging from the Beaufort Sea to the East Siberian Sea with a maximum near the Chukchi Sea. In this region HIRHAM5 is not able to fully simulate the tongue of low pressure as shown by ERA-Interim (Fig. 4.6(b)). The beginning of August 2012 was embossed by the great Arctic cyclone [Zhang et al., 2013] that developed on 2nd August over northern Siberia and entered the East Siberian Sea on 4th August and reached its maximum on 6th August with a minimum central pressure of 966 hPa (Simmonds and Rudeva [2012], Zhang et al. [2013] and Parkinson and Comiso [2013]). The cyclone persisted almost 13 days and had

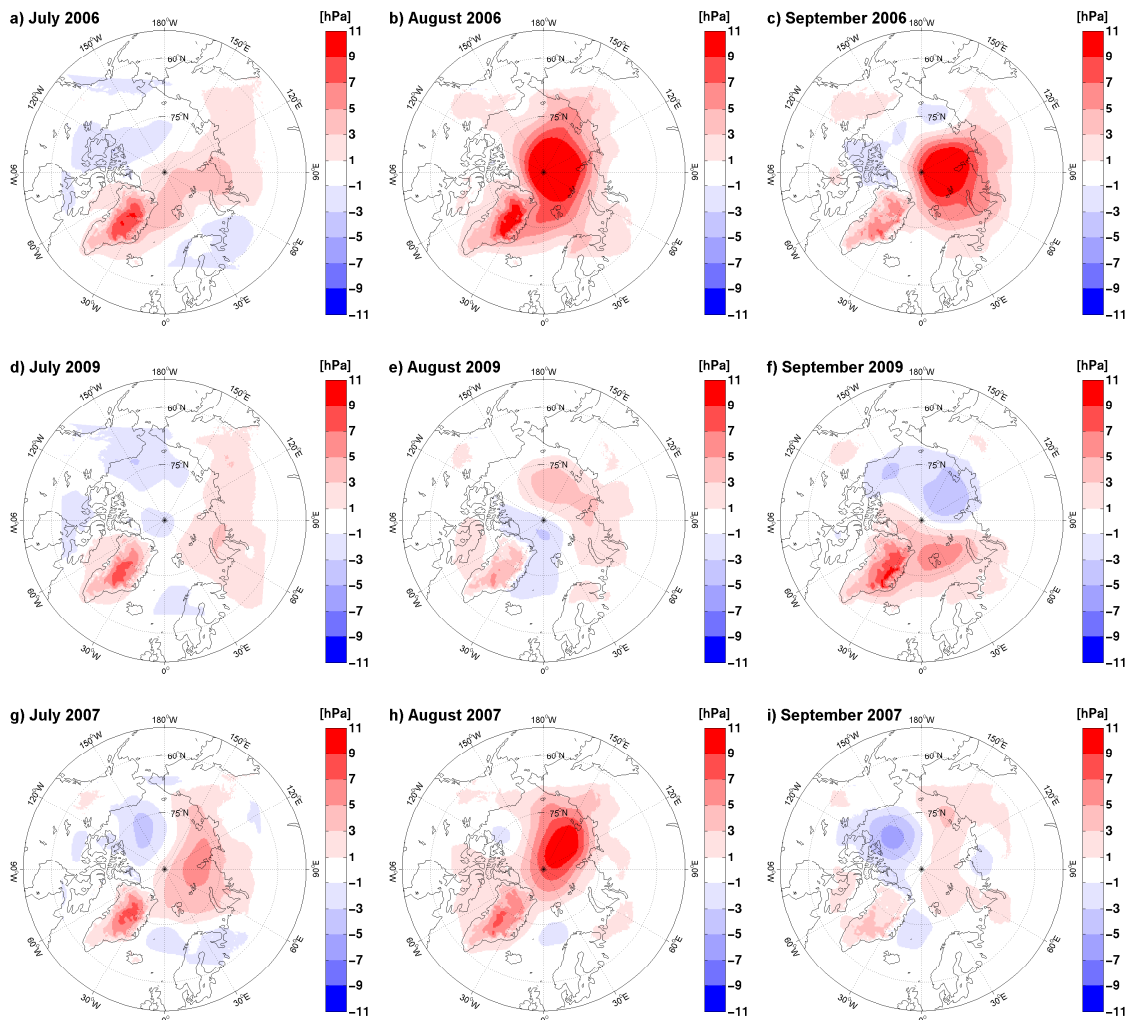


Figure 4.8: Spatial distribution of the monthly averaged difference of the mslp in *hPa* between the HIRHAM5 simulations (ensemble mean) and the data provided by ERA-Interim for July, August and September (columns) for the ensembles representing the high ice years 2006 and 2009 (first and second row) and the low ice year 2007 (third row). The corresponding figures for the low ice year 2012 are shown in Fig. 4.5(c), 4.6(c) and 4.7(c).

strong impact on the sea ice (Fig. 4.2(k)), with enhanced ice breakup and melting and decreased thickness in the Canadian Basin due to increased upward ocean heat transport caused by the strong winds and associated ice motion [Zhang et al., 2013]. Therefore, the sea ice retreated rapidly between 4th August and 8th August 2012 [NSIDC, 2015]. Differently to the underestimation of the pressure over the Arctic Ocean, the pressure over the land areas is mainly overestimated by HIRHAM5 during summer 2012.

However, the biases in the pressure distribution for the ensembles 2006, 2007 and 2009 (Fig. 4.8 for mslp and Fig. 4.9 for geopotential height at 500 *hPa*) reveal that the HIRHAM5 in general rather tends to overestimate than underestimate the pressure. More precisely, the area of positive bias is larger than the area of negative bias. Besides, the absolute values

4.2. EVALUATION OF HIRHAM5

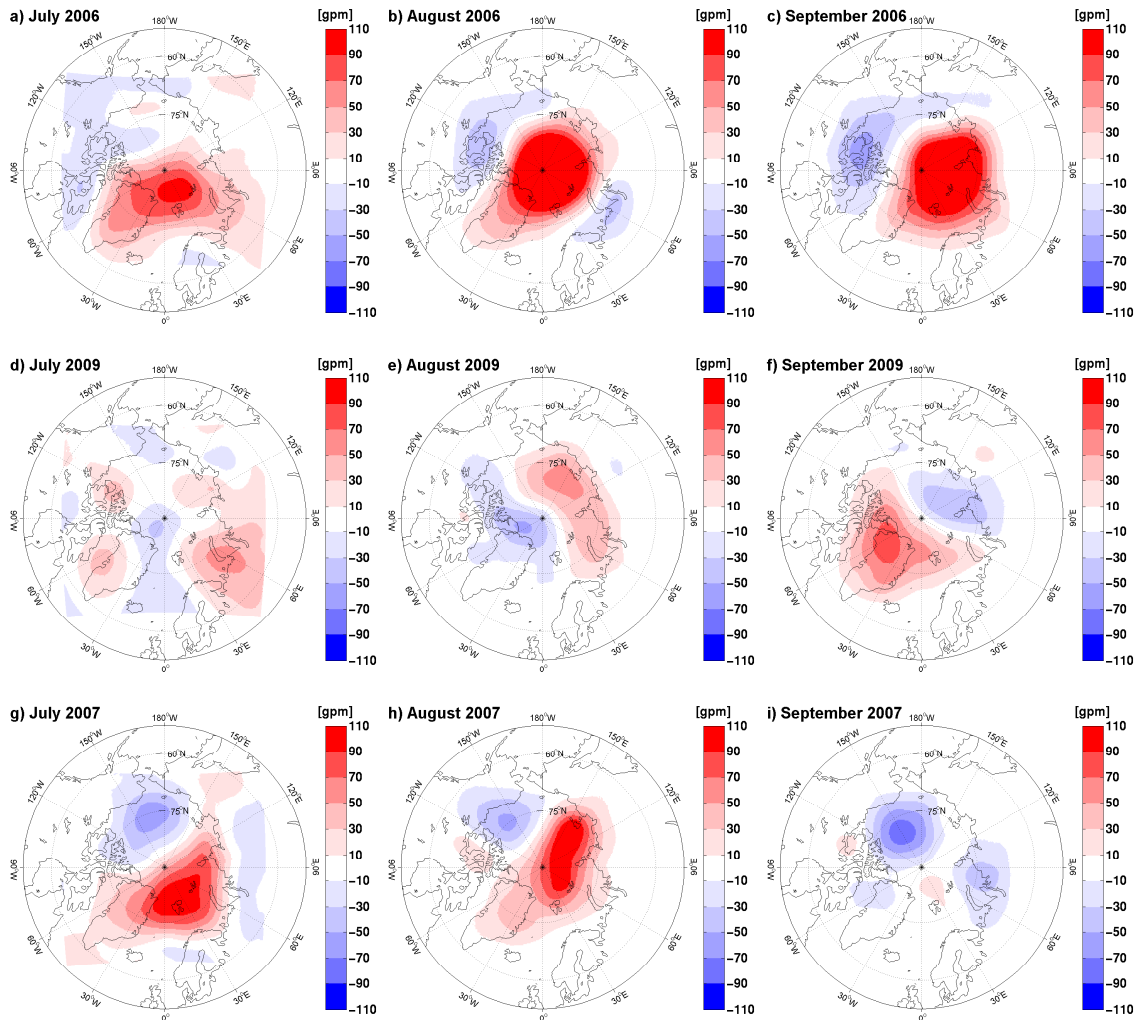


Figure 4.9: Spatial distribution of the monthly averaged difference of the geopotential height at 500 hPa in gpm between the HIRHAM5 simulations (ensemble mean) and the data provided by ERA-Interim for July, August and September (columns) for the ensembles representing the high ice years 2006 and 2009 (first and second row) and the low ice year 2007 (third row). The corresponding figures for the low ice year 2012 are shown in Fig. 4.5(f), 4.6(f) and 4.7(f).

illustrate a more intense overestimation compared to the magnitude of the underestimation. During summer 2006 the bias reaches values of up to 120 gpm at 500 hPa and 12 hPa for mslp over the Arctic Ocean. The same is valid during July (geopotential height at 500 hPa) and August 2007 (geopotential height at 500 hPa and mslp).

Generally, a strong underestimation of the pressure over the Beaufort Sea is found in the biases of the mslp and the geopotential at 500 hPa . This region is characterised by high pressure during July and August especially at the surface (Fig. 5.3(first and second columns)). In September this area is distinguished by low pressure at 500 hPa that is underestimated compared to ERA-Interim, representing the formation of the polar vortex. The underestimation of both, the high pressure at the surface and low pressure in 500 hPa

illustrates that the high pressure at the surface is simulated to weak and the low pressure at 500 *hPa* is simulated to strong.

Different to 2012, it is found in general that the monthly averaged atmospheric circulation patterns during July and August 2006, 2007 and 2009 (see Fig. 5.3 and Fig. 5.4) are characterised by high pressure over the Arctic Ocean that is overestimated by HIRHAM5. Besides, the biases found during 2012 are smaller compared to the summers 2006, 2007 and 2009, apart from July and August 2009 and September 2007. The latter one is characterised by relatively small biases near the surface and a spatially limited bias in geopotential at 500 *hPa*.

Generally, it is obvious that the bias between the ensemble mean of the HIRHAM5 simulations and the ERA-Interim data set is smaller than the ensemble standard deviation (explained in detail in Sec. 5.1, see contour lines in Fig. 4.5, Fig. 4.6 and Fig. 4.7). This result illustrates a good agreement of the HIRHAM5 simulations with the ERA-Interim data set, despite using the model without any nudging. The HIRHAM5 capture the circulation processes and provide reliable simulations.

It can be argued, that the biases are a result of the coarser ERA-Interim horizontal resolution compared to HIRHAM5's resolution. The disagreement between HIRHAM5 and the ERA-Interim data set arises from the model set-up that is used. In this work HIRHAM5 runs without any nudging leading to a decoupled development of the simulations from the boundary forcing [Omrani et al., 2012a]. Klaus [2014] obtained very small biases for the HIRHAM5 simulated circulation with respect to the ERA-Interim data set by using the dynamical nudging technique. In the Arctic domain the lateral boundary control is less pronounced compared to a RCM applied over the mid-latitudes [Rinke and Dethloff, 2000]. The HIRHAM5 is able to reproduce the mean atmospheric circulation patterns, although the set-up of the HIRHAM5 runs without any nudging.

4.3 Cyclonic Activity

It can be anticipated shortly, that the diagnostic budget study for the IV of potential temperature reveals that the horizontal and vertical 'baroclinic' terms (B_h and B_v) are the most important processes influencing the IV. This is in agreement with the results found by Rinke and Dethloff [2000], Alexandru et al. [2007], Nikiema and Laprise [2010] and Nikiema and Laprise [2011]. They showed that the IV fluctuates on the synoptic time scale and is associated with synoptic events and Nikiema and Laprise [2010]. Further, Nikiema and Laprise [2011] explicitly quantify the impact of the baroclinicity on the IV. Hence, this section deals with the Eady growth rate (EGR) that is defined as the potential for baroclinic instability. With the help of this parameter the results obtained with the diagnostic budget

4.3. CYCLONIC ACTIVITY

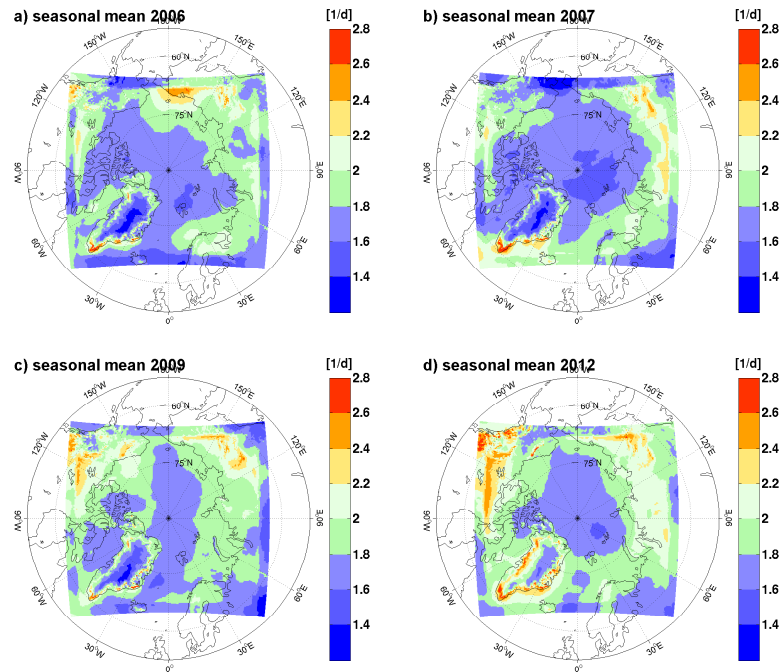


Figure 4.10: Spatial distribution of the seasonal averaged (JAS) Eady growth rate (EGR) between 850 hPa and 500 hPa in $1/d$ simulated with the HIRHAM5 for the ensemble means representing the high ice years 2006 (a) and 2009 (c) and the low ice years 2007 (b) and 2012 (d). The EGR is calculated every six hours for each ensemble member and afterwards the ensemble mean and the temporal average is calculated.

study can be interpreted.

The EGR is calculated between 850 hPa and 500 hPa with six-hourly HIRHAM5 data (see Sec. 3.1) for each ensemble member for each of the four ensembles (2006, 2007, 2009 and 2012). The ensemble mean of the EGR is calculated and the results are shown seasonally averaged (Fig. 4.10) for all four ensembles and for the ensemble of 2012 the monthly averages (Fig. 4.11) are shown as well.

The summer means (JAS) of the EGR (Fig. 4.10) reveal, that the potential for baroclinic instability is small over the central Arctic Ocean. That is the case for all ensembles. However, during 2009 and 2012 high values of EGR reach further into the Arctic Ocean. Over (eastern/central) Siberia the highest values are achieved (up to 2.5 $1/d$) and during summer 2009 and 2012 over Northern America, too. During summer 2006 over eastern Siberia and the Chukchi Sea a region with high EGR is simulated with the HIRHAM5. It seems that the maximum values of EGR follow a belt along the coastlines. It is obvious, that during all years the strongest EGR is simulated over Siberia, Laptev Sea (apart from 2007) and Barents Seas (including the corresponding land parts) and northern America. This is in accordance with the high occurrence of frontal frequency and cyclones in the Arctic during summer. The frontal frequency is high at the coastlines in summer due to the strong temperature gradient between the snow-free land and the cold Arctic Ocean [Serreze

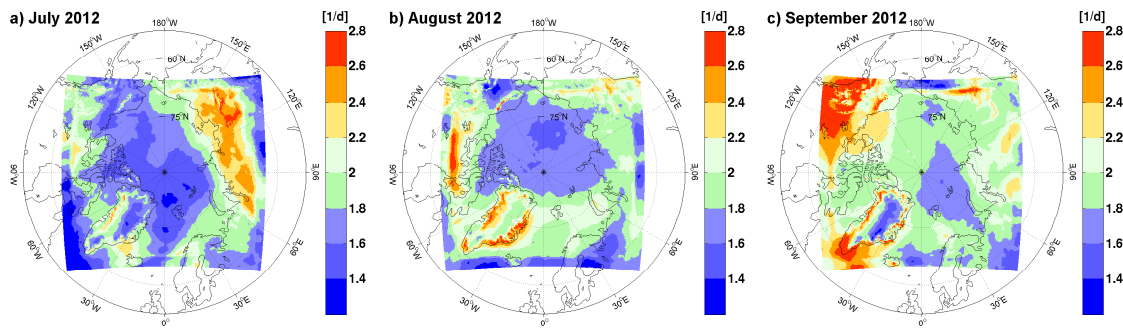


Figure 4.11: Spatial distribution of the monthly averaged Eady growth rate (EGR between 850 hPa and 500 hPa in $1/d$ simulated with the HIRHAM5 for July (a), August (b) and September (c) for the ensemble representing the low ice year 2012. The EGR is calculated every six hours for each ensemble member and afterwards the ensemble mean and the temporal average is calculated.

et al., 2001]. This is associated with baroclinicity that supports cyclogenesis. These results are conform with a high rate of cyclogenesis over northern Eurasia and Canada (Serreze et al. [1993] and references therein) and east-central Eurasia and Alaska [Zhang et al., 2004]. However, cyclones generated over Alaska migrate south-eastward to the Canadian Archipelago and the ones that have their origin in Eurasia migrate eastward and mostly enter the Arctic Ocean [Zhang et al., 2004]. More precisely, the cyclones enter the Arctic Ocean within a wide area from the Laptev Sea to the Chukchi Sea [Serreze et al., 1993] during summer. However, Sorteberg and Walsh [2008] figured out that the Norwegian, Barents and Kara Seas have a high cyclone activity. During summer the cyclones tend to converge over the central Arctic Ocean, independent of their origin [Sorteberg and Walsh, 2008]. Hence, in this region the cyclone activity is connected with cyclolysis [Serreze, 1995] illustrating the decay of the cyclones. Therefore, the values of the EGR are small over the Arctic Ocean (Fig. 4.10).

In general the belts of high EGR coincide with the regions of the horizontal 'baroclinic' term that is associated with synoptic events and contributes to the IV generation within HIRHAM5 (see Chapter 6 and Fig. 6.6(c), Fig. A.5(c), Fig. A.7(c) and Fig. A.6(c)).

For the investigation of the temporal evolution of the spatial distribution of the EGR for each ensemble the monthly means are calculated (shown here for the ensemble 2012 (Fig. 4.11)). It is obvious that the potential for baroclinicity is largest during September (especially over Northern America and at the southern part of Greenland). However, it is interesting that during July 2012 the most intense EGR is found over northern Siberia, whereas it becomes weaker during August and September. However, high values of EGR extends from the Barents Sea towards Greenland (Fig. 4.11(b)).

For the other ensembles (2006, 2007 and 2009) (not shown) the highest EGR is also simulated during September with strongest values over the land areas especially, over northern America (2009) and central Siberia (2006 and 2007). The other months are

4.3. CYCLONIC ACTIVITY

characterised by small areas of high EGR. During July 2006 and 2009, EGR shows maxima over east Siberia and during August 2009 additionally over the Northern American coast. The EGR is overall quite weak in August.

Chapter 5

Simulated IV based on HIRHAM5

The atmosphere's chaotic behaviour and non-linearities generate internal variability (IV) (see Chapter 1 for more details). This internally generated variability can influence physically forced signals in RCMs [Rinke et al., 2004] and references therein. Hence, the quantification of IV helps to separate the IV from externally generated climate signals in a RCM.

In this chapter the magnitude of the IV is quantified for the HIRHAM5 ensemble simulations. Time periods, regions within the Arctic domain and vertical levels of particularly high and low IV are identified. Four ensembles (2006, 2007, 2009 and 2012) with 20 ensemble members in each case were performed and investigated with a special attention to the behaviour of the IV during high ice years (2006, 2009) and low ice years (2007, 2012). The considered time period is 6th July to 30th September for the four ensembles. The results are shown from 1000 *hPa* up to 300 *hPa*, because the focus of this study is on the troposphere. The analysis contains the quantification of the IV for the mslp, the geopotential height (Sec.5.1) and the potential temperature (Sec. 5.2). As explained in Sec. 3.2 the IV for the atmospheric circulation is examined by calculating the standard deviation between the ensemble members (across-member standard deviation), while for the potential temperature the variance between the ensemble members (across-member variance) is investigated.

5.1 IV of Mean Sea Level Pressure and Geopotential

In this section, the IV of the atmospheric circulation is analysed. The six-hourly domain averaged ensemble mean (black bold line) and the across-member spread (shaded in grey) of the mslp is shown in Fig. 5.1 and of the geopotential height in different heights (850 *hPa*, 500 *hPa* and 300 *hPa*) is represented in Fig. 5.2. The figures indicate that the amplitude of the ensemble spread fluctuates in time and becomes smaller with increasing height. This

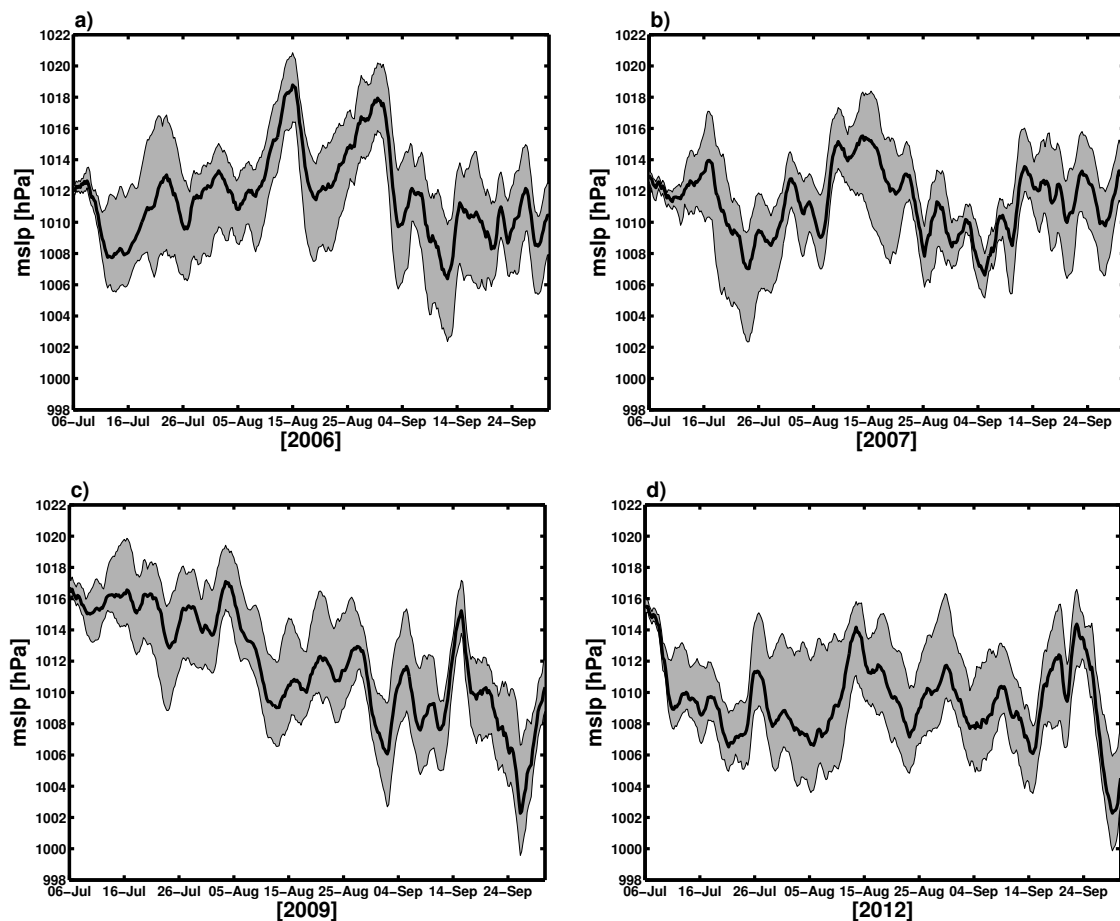


Figure 5.1: Temporal evolution of the ensemble mean mslp (bold black line) and the across-member standard deviation (ensemble spread shaded in grey) in hPa simulated with the HIRHAM5 for the ensembles representing the high ice years 2006 (a) and 2009 (c) and the low ice years 2007 (b) and 2012 (d).

is due to the fact, that at lower levels the subgrid-scale processes (turbulence, convection and condensation) play a more important role than at higher levels. The calculation of the normalised (by the ensemble mean) standard deviation (not shown) more clearly illustrates the height dependency of the IV of the atmospheric circulation. At 850 hPa the normalised standard deviation can reach values of up to 5 %, at 500 hPa of up to 1.7 % (or even 2 % during 2012) and at 300 hPa of up to 1.3 % (or even 1.6 % during 2012). However, the normalised standard deviation is smallest for the mslp (Fig. 5.1) with values of up to 0.9 %. This is caused by the lower boundary forcing that is prescribed every six hours and inhibits the free development of each ensemble member reducing the IV. During the beginning of August 2012, when the great Arctic cyclone event occurs, the across-member spread is particularly high (up to 10 hPa in the mslp (Fig. 5.1(d)) and 100 gpm in the geopotential height at 850 hPa (Fig. 5.2(j))). This is also seen in the spatial distribution of the standard deviation (contour lines) of the mslp (Fig. 4.6(a)) and of the geopotential height (Fig. 4.6(d)). The investigation of the atmospheric circulation for each individual

5.1. IV OF MEAN SEA LEVEL PRESSURE AND GEOPOTENTIAL

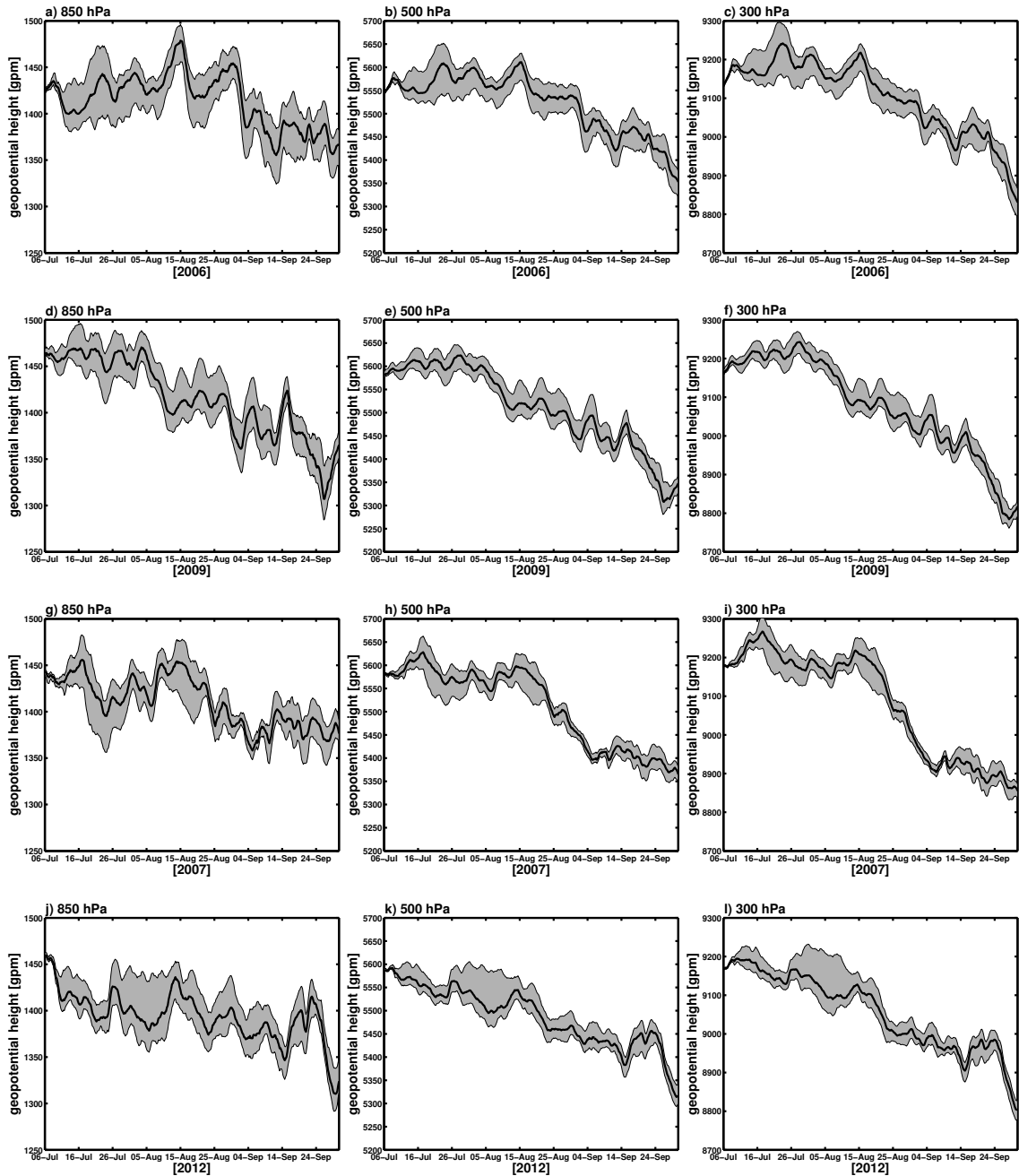


Figure 5.2: Temporal evolution of the ensemble mean geopotential height (bold black line) and the across-member standard deviation (ensemble spread shaded in grey) in *gpm* at 850 *hPa*, 500 *hPa* and 300 *hPa* (columns) simulated with the HIRHAM5 for the ensembles representing the high ice years 2006 and 2009 (first and second row) and the low ice years 2007 and 2012 (third and fourth row).

ensemble member during the beginning of August 2012 reveals, that only eight out of the 20 realisations simulate the great Arctic cyclone event. In general they agree in the origin, the track, the temporal development and the intensity of the cyclone compared to the observations that are explained by several studies (Simmonds and Rudeva [2012], Zhang et al. [2013] and Parkinson and Comiso [2013]) and to the ERA-Interim data set.

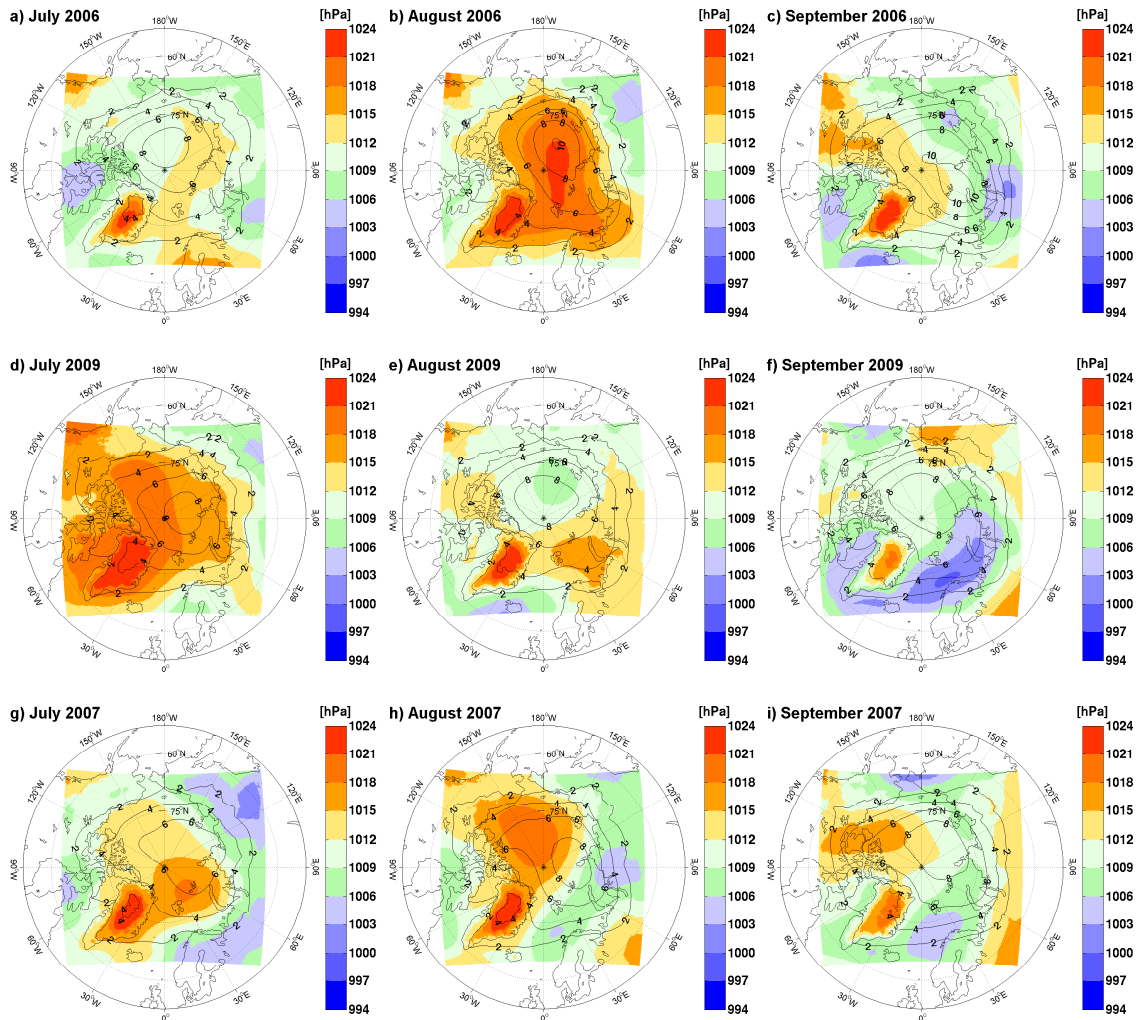


Figure 5.3: Spatial distribution of the monthly averaged mslp in *hPa* (colour) and its across-member standard deviation (contours) simulated with the HIRHAM5 for July, August and September (columns) for the ensembles representing the high ice years 2006 and 2009 (first and second row) and the low ice year 2007 (third row). The corresponding figures for the low ice year 2012 are shown in Sec. 4.2 in Fig. 4.5(a), Fig. 4.6(a) and Fig. 4.7(a).

The representation of the cyclone by the other ensemble members is poor, due to an early dissipation or the diverging track.

Fig. 5.3 shows the spatial distribution of the ensemble mean mslp for the ensembles representing the high ice years 2006, 2009 and the low ice year 2007 (rows). Figs. 4.5(a), 4.6(a) and 4.7(a) show the same for the ensemble 2012. All the figures contain the corresponding standard deviation between the ensemble members (contour lines). Fig. 5.4 shows the corresponding results for the geopotential height at 500 *hPa* (see Fig. 4.5(d), 4.6(d) and 4.7(d) for the ensemble 2012). The figures show that the IV is small near the boundaries of the model domain, that is caused by the lateral boundary forcing which is equal for each simulation (see Sec. 2.2). Within all ensembles the standard deviation of

5.1. IV OF MEAN SEA LEVEL PRESSURE AND GEOPOTENTIAL

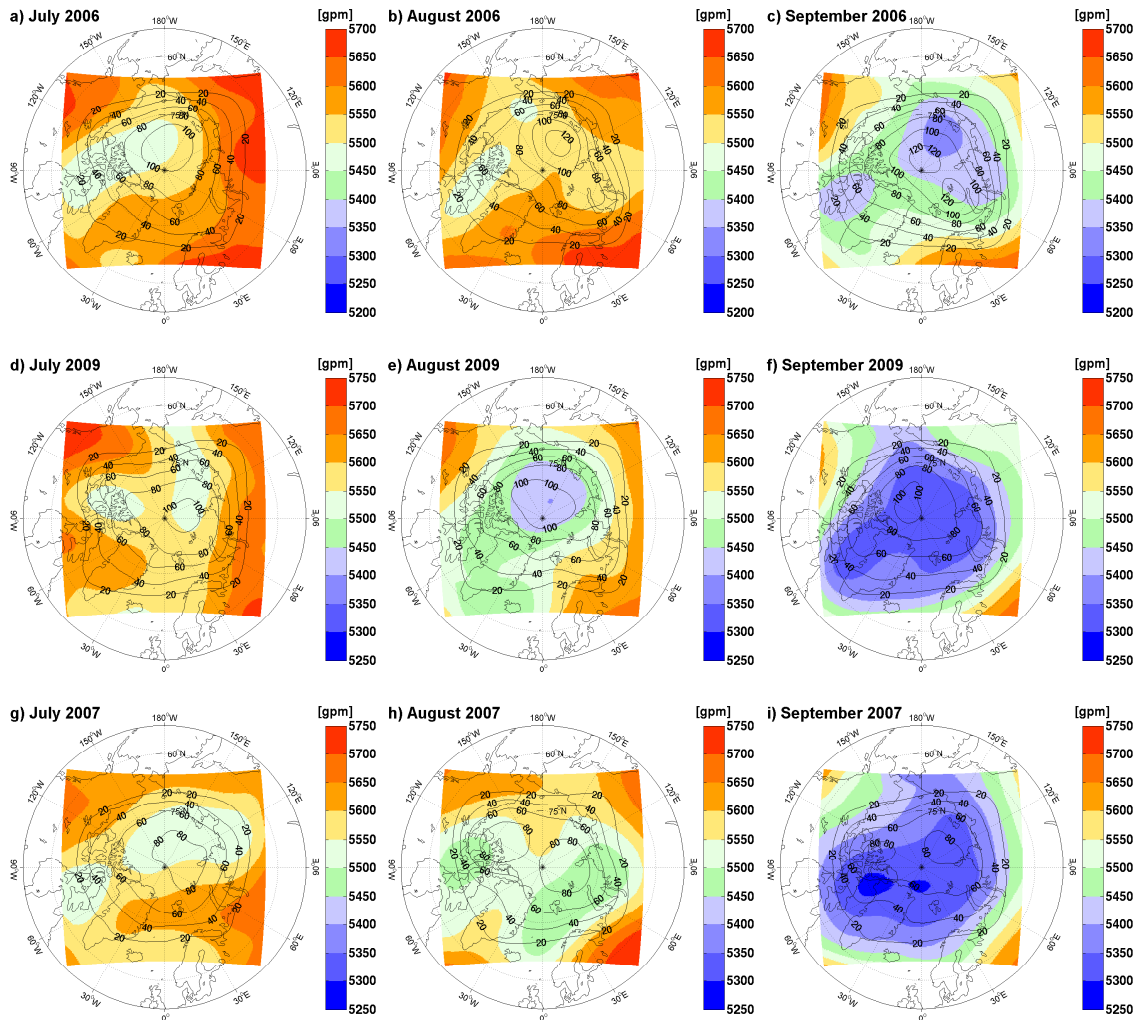


Figure 5.4: Spatial distribution of the monthly averaged geopotential height in gpm at $500 hPa$ (colour) and its across-member standard deviation (contours) simulated with the HIRHAM5 for July, August and September (columns) for the ensembles representing the high ice years 2006 and 2009 (first and second row) and the low ice year 2007 (third row). The corresponding figures for the low ice year 2012 are shown in Sec. 4.2 in Fig. 4.5(d), Fig. 4.6(d) and Fig. 4.7(d).

mslp and geopotential height has its maximum over the central Arctic Ocean. In September 2006 and August and September 2007 the standard deviation of the geopotential height exhibits a pattern with two maxima. This is not the case for the corresponding mslp standard deviation. However, Rinke and Dethloff [2000] found that within their HIRHAM4 ensemble simulations for July 1990. The magnitude of the mslp standard deviation during September 2012 is comparable to the other ensembles. During August 2012 the standard deviation reaches values higher than $12 hPa$ (Fig. 4.6(a)) associated with the great Arctic cyclone event.

In general, the ensemble standard deviation and therefore the IV for the atmospheric circulation pattern is slightly stronger during 2006 compared to the other ensembles. This

is found for the IV of the potential temperature as well (see Sec. 5.2). Additionally, the bias of the ensemble mean compared to ERA-Interim is large (see Sec. 4.2) during 2006. This indicates, that not only the ensemble mean during summer 2006 differs more from the reality compared to the other ensemble years, but the ensemble members differs strongly to each other as well. Both, the large bias and the large across-member standard deviation maybe are caused by a simulation that differ intensely from the other ensemble members. A closer look reveals that during August and September 2006, the ensemble mean biases of the atmospheric circulation (see Fig. 4.8 and Fig. 4.9) are slightly larger than the across-member standard deviation in some regions over the Arctic Ocean. The same is valid for August 2007 and for the geopotential height at 500 *hPa* during July 2007. A larger model bias compared to the IV illustrates that all simulations of an ensemble differ from the ERA-Interim fields, but are similar to each other. This is a hint for a systematic error within HIRHAM5, however, the biases exceed only slightly the IV. For 2012 (see Fig. 4.5, Fig. 4.6, 4.7) and 2009 (see Fig. 4.8 and Fig. 4.9(second row)), the model bias reveals values of the same order or even smaller than the IV. The outcome that the model bias is smaller than the IV was discussed by Rinke and Dethloff [2000] for the month July as well, but with an ensemble generated with the former model version HIRHAM4 covering the year 1990. They interpreted their findings such that the internally generated model noise due to the initial data can have the same magnitude as the bias caused by the parameterisations. However, Rinke and Dethloff [2000] obtained smaller values of standard deviations with HIRHAM4 compared to the results obtained with the HIRHAM5 simulations in this work. The reason could be that they analysed the year 1990 with an ensemble of only four members. The ensemble simulations by Alexandru et al. [2007] over the northeastern part of Northern America and the western North Atlantic Ocean showed weaker IV for the geopotential height than found here. This can be understood by the considered mid-latitude model domain. Several studies pointed out, that the flow situation differs between the mid-latitudes and the Arctic domain influencing the IV (e.g. von Storch [2005], Rinke and Dethloff [2000] and Rinke et al. [2004]). Perturbations due to different IC stay longer in the Arctic domain due to the typical circum-polar circulation. This also explains the obtained increasing IV towards the autumn season [Rinke et al., 2004] caused by the intensifying polar vortex that inhibits the movement of the IV out of the model domain (Lucas-Picher et al. [2008a] and references therein).

5.2 IV of Potential Temperature

In the following, the IV of potential temperature is analysed by calculating its vertical profile, the temporal evolution and the spatial distribution. It has to be noted that the

spatial distributions herein are shown as seasonal means from July to September (averaged over the full period from 6th July to 30th September). In this section the IV of potential temperature is investigated by using the across-member variance (Eq. 3.5) instead of the across-member standard deviation. The across-member variance of potential temperature is the input for the diagnostic budget study for examining the contributions to the IV tendency (Chapter 6).

The vertical, temporal and domain averaged IV is strongest within the ensemble 2006 (see Tab. 6.1). The vertical profile for the temporal and domain averaged potential temperature IV is shown in Fig. 5.5(a). In general the vertical profile is quite similar for all years: Lowest values are observed close to the surface and in the upper troposphere, two peaks of high IV are found in the lower troposphere and at 500 *hPa* and in between these peaks the IV is weaker. A more detailed view reveals that for 2006, 2007 and 2009 largest values are observed in the lower troposphere (925 *hPa* to 950 *hPa*) and a second maximum occurs at 500 *hPa*. Whereas, in 2012 the absolute maximum is found at 500 *hPa* (ca. 7.5 K^2) and the second maximum is located at 925 *hPa* which reaches much lower values (ca. 5.5 K^2). The comparisons between the first and the second maxima for the other ensembles indicate that the differences between both maxima are smaller compared to the maxima in 2012. The smallest values of IV are simulated near the surface, because of the lower boundary forcing that is equal for all ensemble members, and at 300 *hPa*.

With regard to the investigation of the IV in high and low ice years, the near-surface IV (at 925 *hPa*) is stronger for the high ice years 2006 and 2009 compared to the low ice years 2007 and 2012. However, in the upper levels a dependency between the sea ice state and the IV of potential temperature is not detected.

Fig. 5.5(b) presents the temporal evolution of the domain and vertical averaged IV of potential temperature for all years, while Fig. 5.6 shows the domain average at different vertical levels. It is obvious that the IV grows during the first five days of the analysed time period indicating a spin-up time. Generally, the potential temperature IV of each ensemble strongly fluctuates in time at all levels. The vertical averaged temporal evolution (Fig. 5.5(b)) reveals that IV fluctuates between 3 K^2 and 9 K^2 during summer 2007 and 2012. In 2006 the IV reaches values between 5 K^2 and 11 K^2 and in 2009 between 5 K^2 and 9 K^2 . The most distinct peaks of IV are found in 2006, while the peaks during the other years are not that outstanding compared to the mean fluctuation.

Fig. 5.6 clearly illustrates the temporal development of the IV of potential temperature in different heights. The peaks that are marked in Fig. 5.6 are high IV events. Their IV characteristics are summarised in Tab. 8.1 and the red ones are investigated in detail in Chapter 8.

During the beginning of the simulations all ensembles provide the maximum IV at 925

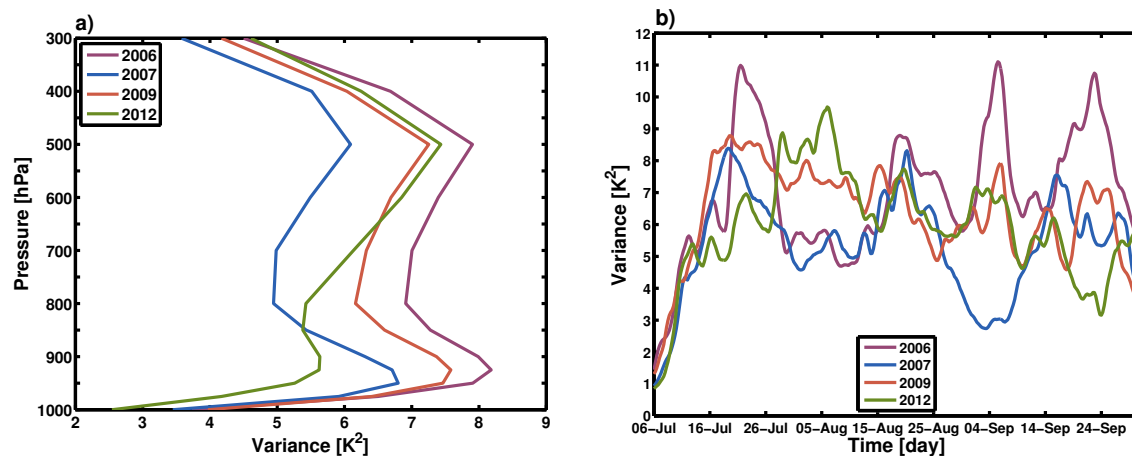


Figure 5.5: Vertical profiles of the temporal and domain averaged (a) and the temporal evolution of the domain and vertical averaged (b) across-member variance (IV) in K^2 for the ensembles representing the high ice years 2006 and 2009 and the low ice years 2007 and 2012.

hPa. However, with consecutive simulation time the level of maximum IV depends on the time and can occur at 925 *hPa* or 500 *hPa*, but from the beginning of September the occurrence of the maximum IV at 500 *hPa* predominates. Independent of the level at which the maximum IV occurs, the peaks could reach values between 12 K^2 and 14 K^2 . The IV is smallest in 300 *hPa* for all simulated years. But, there the IV fluctuates in time as well. However, the amplitude of the fluctuations is weakest during 2009. During 2012 the highest IV of potential temperature (Fig. 5.6(d)) occurs at 500 *hPa* (up to 14 K^2). Only during the beginning of the simulation (until the end of July) the highest IV is observed at 925 *hPa* and later the IV is dominated by IV at 500 *hPa*. At all pressure levels, IV reaches highest values between 27th July and 9th August with an absolute maximum of ca. 14 K^2 at 500 *hPa* on 5th August 2012 at 06 UTC. This result coincides with the great Arctic cyclone event of August 2012 [Zhang et al., 2013]. This shows that the temporal evolution of the potential temperature IV is associated with the occurrence of synoptic events. Lowest values of IV occur during 19th September and 24th September 2012 of ca. 4 K^2 at 500 *hPa*.

Tabs. 6.1 - 6.4 summarise the domain averaged values for the IV of potential temperature. They indicate that all ensembles produce highest values of IV at 925 *hPa* (apart from 2012) and lowest at 1000 *hPa* followed by the IV at 300 *hPa*.

Considering the high and low ice years no dependency could be pointed out concerning the temporal evolution of IV. The course and magnitude of the temporal evolution of IV seems not to be influenced by the sea ice conditions.

The spatial patterns of the temporal averaged potential temperature IV at 925 *hPa* (left column) and 500 *hPa* (right column) are shown in Fig. 5.7 for the high ice years 2006

5.2. IV OF POTENTIAL TEMPERATURE

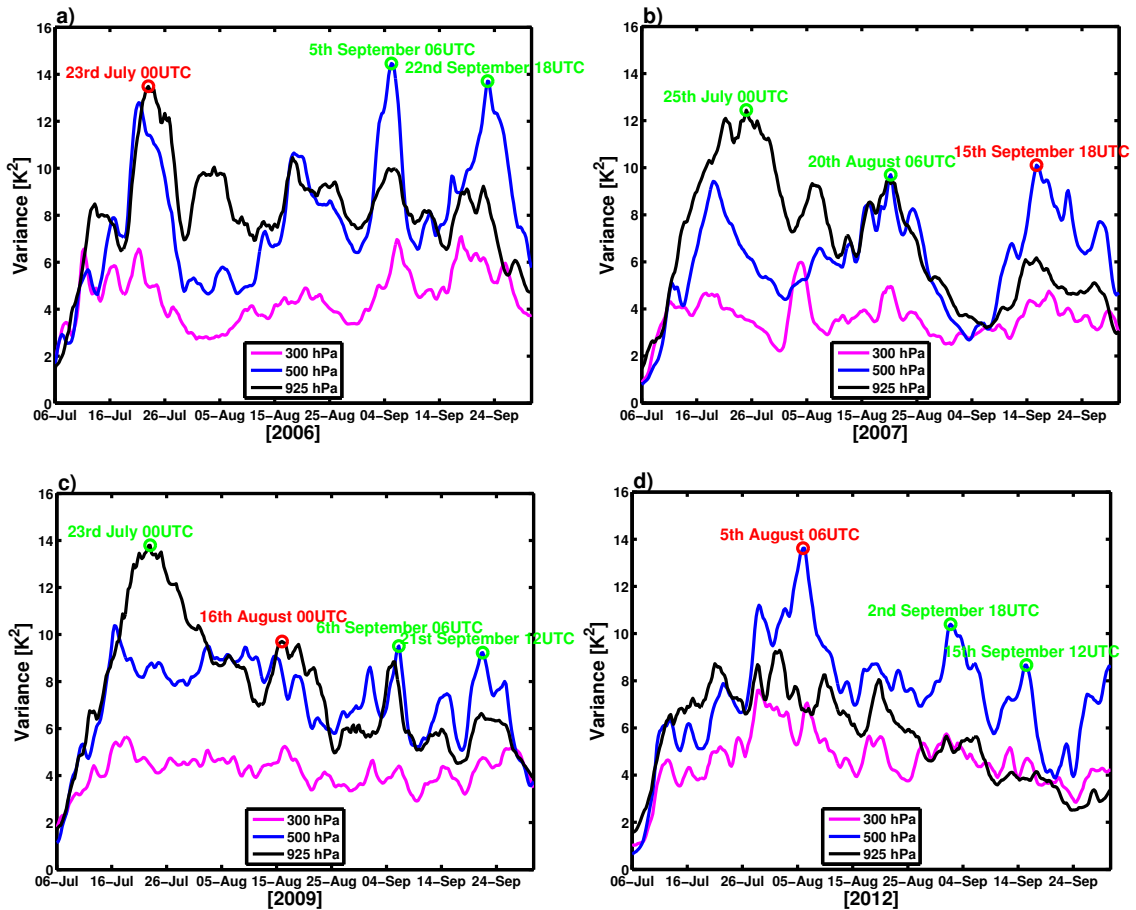


Figure 5.6: Temporal evolution of the domain averaged across-member variance (IV) in K^2 at 925 hPa, 500 hPa and 300 hPa for the ensembles representing the high ice years 2006 (a) and 2009 (c) and the low ice ensembles 2007 (b) and 2012 (d). The marked time steps are investigated and their results are summarised in Tab. 8.1 and the red ones are analysed in detail in Chapter 8.

and 2009 (first and second row) and the low ice years 2007 and 2012 (third and fourth row). The IV is small near the boundaries of the model domain due to the identical lateral boundary forcing in all simulations of one ensemble. The strongest IV ($> 12 K^2$) is found over the whole Arctic Ocean in summer 2006. During 2009 at 925 hPa high IV is found in a small part of the Beaufort Sea, but a large area at the Siberian coast and a region north of Greenland. In 2007, such large IV is found only over the Beaufort and the Laptev Seas. At 925 hPa during 2012 two centres of high potential temperature IV ($8 K^2$ to $10 K^2$) can be noted over the East Siberian/Laptev Seas and the Beaufort Sea areas (Fig. 5.7(g)), however, with lower intensity compared to the other ensembles. The maximum IV is found in 500 hPa (Fig. 5.7(h)). There is a large area covering the Arctic Ocean over which the IV reaches values up to $12 K^2$. The same is valid for 2006 and 2009 at 500 hPa. During 2007, the IV at 500 hPa is smaller and values of only up to $10 K^2$ are calculated. It is obvious that the locations of maximum IV and its intensity change with height. Therefore, the vertical

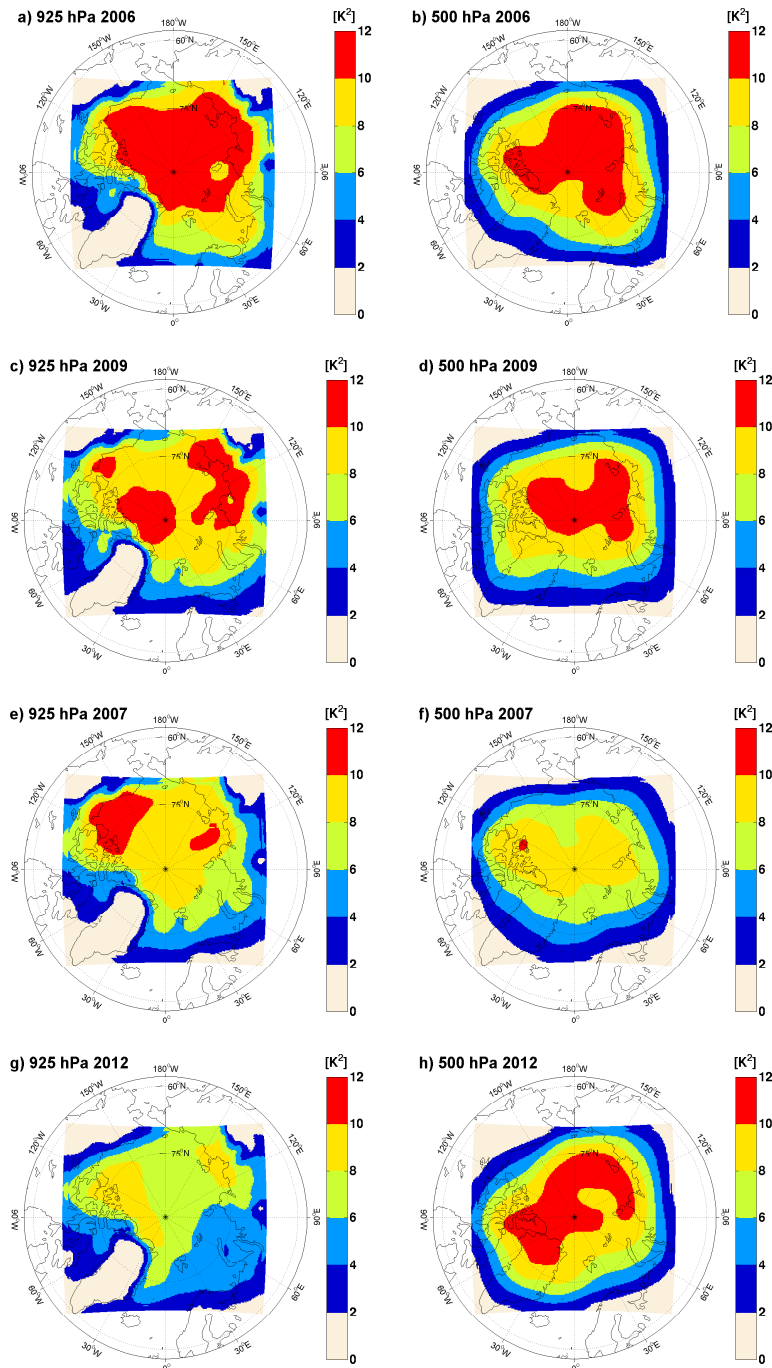


Figure 5.7: Spatial distribution of the temporal averaged across-member variance (IV) in K^2 at 925 hPa (left column) and at 500 hPa (right column) for the ensembles representing the high ice years 2006 and 2009 (first and second row) and the low ice years 2007 and 2012 (third and fourth row).

averaged pattern (not shown) is spatially quite homogeneous without any pronounced local maxima and minima apart from 2006 over the East Siberian and Laptev Seas.

The spatial distribution of IV reveals that with decreasing sea ice concentration the IV of potential temperature weakens. However, this is valid only near the surface and not found

at 500 *hPa* (Fig. 5.7(right column)) and in the vertical averaged spatial distributions (not shown). Furthermore, the locations of the centres with maximum IV do not coincide with the ice covered or ice free regions (see Fig. 4.2).

In general the vertical profiles of potential temperature IV are in agreement with the results obtained for the northeastern part of Northern America and parts of the Atlantic Ocean (using the Canadian RCM) with highest values near the surface and decreasing IV intensity with increasing height [Nikiema and Laprise, 2010]. However, a second maximum is found at 500 *hPa* for the Arctic domain, whereas for the mid-latitudes a second maximum is obtained at ca. 200 *hPa* [Nikiema and Laprise, 2010]. Further, the magnitude of IV is ten to 100 times larger for the Arctic domain compared to mid-latitudes IV of potential temperature. This result supports the findings in Sec. 5.1 and the therein given explanations concerning the dependency of the IV on the geographical location (Rinke et al. [2004] and von Storch [2005]).

In accordance with previous studies for other regions (Giorgi and Bi [2000], Christensen et al. [2001], Caya and Biner [2004], Wu et al. [2005], Lucas-Picher et al. [2008a] and several more), the pronounced temporal variation of IV in the Arctic it has to be emphasised. The IV of potential temperature differs in an order of three between the high and low IV events. Contrary to this result the amplitudes of the temporal evolution are larger over Northern America resulting in maximum potential temperature IV events of intensities five times larger than in low IV events [Nikiema and Laprise, 2010].

Chapter 6

Processes of Potential Temperature IV

In the previous Chapter 5, the IV generated within the HIRHAM5 ensemble simulations was examined and quantified in detail by using the across-member standard deviation for the atmospheric circulation and the across-member variance for the potential temperature. The various contributions to IV generated within the HIRHAM5 are investigated in this chapter.

The aim is to quantify the dynamical and diabatic contributions to the IV tendency. Hence, Eq. 3.34 (see Sec. 3.3.1) is used, which describes the IV tendency of potential temperature on the left-hand side and the contributions to the IV tendency on the right-hand side. The diagnostic budget study of potential temperature IV tendency was developed by Nikiema and Laprise [2010]. They identify seven contributions to the IV tendency of potential temperature (see Eq. 3.34 and Eq. 3.35). The dynamical terms (explained in detail in Sec. 3.3.2) are the horizontal and vertical transport terms (A_h and A_v), the horizontal and vertical 'baroclinic' terms (B_h and B_v) and the horizontal and vertical third-order terms (E_h and E_v). The contribution C is the diabatic source and sink term that includes the temperature tendencies due to radiation, vertical diffusion, convection and condensation. The sum of the seven contributions should be equal to the IV tendency on the left-hand side. However, this is not applicable due to the fact that small dissipative mechanisms that are operating within the HIRHAM5, either in the numerics of the model or such as the neglected horizontal diffusion, are not considered within this budget study (see Sec. 3.3). The budget study is done for each of the four ensembles representing both high ice years (2006, 2009) and both low ice years (2007 and 2012), covering the time period from 6th July to 30th September. The aim is to analyse the individual contributions to the IV tendency of the potential temperature with respect to their overall importance and specific magnitude, pattern and variability. As described in Chapter 5, the IV characteristics are similar in low and high ice years. Similarly the patterns of the dynamical and diabatic contributions do not differ among the years. Therefore, the present chapter focuses on

Table 6.1: Temporal and domain averaged potential temperature across-member variance (IV) in K^2 , the seven contributions in $\times 10^{-5} K^2/s$ to IV tendency and the sum of all contributions (last row) for the ensemble representing the high ice year 2006.

	vertical average	at 1000 hPa	at 925 hPa	at 800 hPa	at 700 hPa	at 500 hPa	at 300 hPa
IV	6.93	3.73	8.18	6.91	7.00	7.90	4.50
Ah	-0.45	0.55	-0.02	-0.18	-0.37	-0.80	-0.87
Av	-0.02	-0.13	0.23	0.10	0.07	-0.15	-0.12
Bh	5.24	8.29	7.39	4.26	3.84	5.41	3.49
Bv	-3.79	-0.51	-3.60	-3.79	-3.82	-4.74	-1.55
Eh	-0.23	0.08	-0.31	-0.30	-0.28	-0.15	0.09
Ev	0.10	-0.22	-0.01	0.61	0.26	-0.22	0.09
C	0.36	-6.50	-1.57	1.00	1.56	1.74	-0.40
sum of all terms	1.21	1.55	2.12	1.70	1.26	1.09	0.73

Table 6.2: Temporal and domain averaged potential temperature across-member variance (IV) in K^2 , the seven contributions in $\times 10^{-5} K^2/s$ to IV tendency and the sum of all contributions (last row) for the ensemble representing the high ice year 2009.

	vertical average	at 1000 hPa	at 925 hPa	at 800 hPa	at 700 hPa	at 500 hPa	at 300 hPa
IV	6.38	3.97	7.58	6.16	6.33	7.25	4.17
Ah	-0.36	0.36	-0.04	-0.20	-0.39	-0.60	-0.63
Av	-0.03	-0.18	0.05	0.06	0.07	-0.09	-0.02
Bh	4.67	8.29	7.09	3.73	3.27	4.64	2.50
Bv	-3.84	-0.76	-3.82	-3.98	-3.89	-4.78	-1.09
Eh	-0.08	0.10	-0.31	-0.29	-0.21	0.13	0.35
Ev	0.12	-0.28	-0.09	0.70	0.28	-0.20	0.07
C	0.45	-6.82	-1.36	1.04	1.65	1.77	-0.34
sum of all terms	0.93	0.69	1.53	1.05	0.77	0.87	0.84

Table 6.3: Temporal and domain averaged potential temperature across-member variance (IV) in K^2 , the seven contributions in $\times 10^{-5} K^2/s$ to IV tendency and the sum of all contributions (last row) for the ensemble representing the low ice year 2007.

	vertical average	at 1000 hPa	at 925 hPa	at 800 hPa	at 700 hPa	at 500 hPa	at 300 hPa
IV	5.39	3.45	6.71	4.95	4.98	6.09	3.58
Ah	-0.30	0.33	0.02	-0.11	-0.24	-0.53	-0.61
Av	-0.02	0.00	0.08	0.04	0.07	-0.05	-0.13
Bh	4.56	8.57	6.64	3.50	3.18	4.63	2.78
Bv	-3.61	-0.55	-3.51	-3.68	-3.70	-4.49	-1.34
Eh	-0.17	0.20	-0.04	-0.15	-0.25	-0.24	0.11
Ev	0.06	-0.37	0.06	0.44	0.15	-0.09	0.11
C	0.79	-7.01	-0.51	1.99	1.95	1.70	-0.30
sum of all terms	1.31	1.18	2.70	2.04	1.16	0.93	0.62

Table 6.4: Temporal and domain averaged potential temperature across-member variance (IV) in K^2 , the seven contributions in $\times 10^{-5} K^2/s$ to IV tendency and the sum of all contributions (last row) for the ensemble representing the low ice year 2012.

	vertical average	at 1000 hPa	at 925 hPa	at 800 hPa	at 700 hPa	at 500 hPa	at 300 hPa
IV	6.00	2.54	5.62	5.43	6.13	7.43	4.61
Ah	-0.48	-0.37	0.11	-0.19	-0.48	-0.86	-0.94
Av	-0.02	-0.05	-0.03	0.10	0.10	-0.12	-0.00
Bh	5.02	6.16	6.46	3.76	3.75	5.69	3.21
Bv	-4.24	-0.52	-3.99	-4.21	-4.51	-5.33	-1.42
Eh	-0.10	0.02	-0.05	-0.26	-0.24	-0.03	0.29
Ev	0.07	-0.26	-0.13	0.58	0.22	0.25	0.12
C	0.09	-4.33	-0.61	1.43	2.15	2.05	-0.38
sum of all terms	1.15	1.38	1.76	1.21	0.99	1.14	0.87

summer 2012, because of the great Arctic cyclone event and the corresponding sea ice retreat in the beginning of August 2012 (Simmonds and Rudeva [2012], Zhang et al. [2013] and Parkinson and Comiso [2013]). The results for the other ensembles (2006, 2009 and 2007) are explained only shortly and only specifics are pointed out and displayed. However, as for 2012 (Tab. 6.4), the results of the contributions generating and reducing the potential temperature IV are summarised in Tabs. 6.1, 6.2 and 6.3 for the ensembles 2006, 2009 and 2007, respectively. The tables show that during all years and in all heights, the horizontal 'baroclinic' term (B_h) leads to a generation, whereas the vertical 'baroclinic' term (B_v) weakens the IV tendency. Both contributions are the most important ones. However, B_v cannot fully compensate the B_h . The impact of B_h on the IV tendency is most pronounced near the surface, but B_v contributes strongest to the reduction in the mid-troposphere at 500 hPa. The diabatic source and sink term C has a positive influence in the IV tendency on vertical, temporal and domain average. However, the investigation of the vertical dependency of the term C reveals, that its contribution is negative in the lower troposphere and at 300 hPa and positive at mid-tropospheric levels. The strongest impact on IV is found at 1000 hPa. Considering the sum of all contributions (last row in Tabs. 6.1 - 6.4), the net tendency is most balanced in the ensemble 2009 (Tabs. 6.2).

It was emphasised in Chapter 5 that the magnitude of the IV within a RCM depends on the geographical location of the model domain and on the applied RCM. Hence, it is clear that the contributions influencing the IV are affected as well by both factors. Over northeastern part of Northern America the horizontal and the vertical 'baroclinic' terms (B_h , B_v) have the same impact on the IV tendency of potential temperature [Nikiema and Laprise, 2010] as over the Arctic domain, but B_h is weaker in Northern America. However, Nikiema and Laprise [2010] found that the strong negative contribution of B_v is compensated by the diabatic source and sink term C , which is quite small compared to both 'baroclinic' terms over the Arctic. Due to the fact that the IV is larger in the Arctic domain compared to the mid-latitudes, the magnitudes of the contributions to the IV tendency differ in an order of $10 K^2/s$ between both regions.

6.1 Vertical Profile of the Contributions to IV Tendency

The temporal and domain averaged vertical profile for each contribution are shown in Fig. 6.1(a) for the high ice years 2006 and 2009 and in Fig. 6.1(b) for the low ice years 2007 and 2012. As already discussed for the vertical profiles of the IV of potential temperature, the vertical profiles of the seven contributions for each year are relatively similar in their behaviour and magnitudes as well. Hence, there is no clear signal indicating high and low ice conditions, not even near the surface as found for the IV.

6.1. VERTICAL PROFILE OF THE CONTRIBUTIONS TO IV TENDENCY

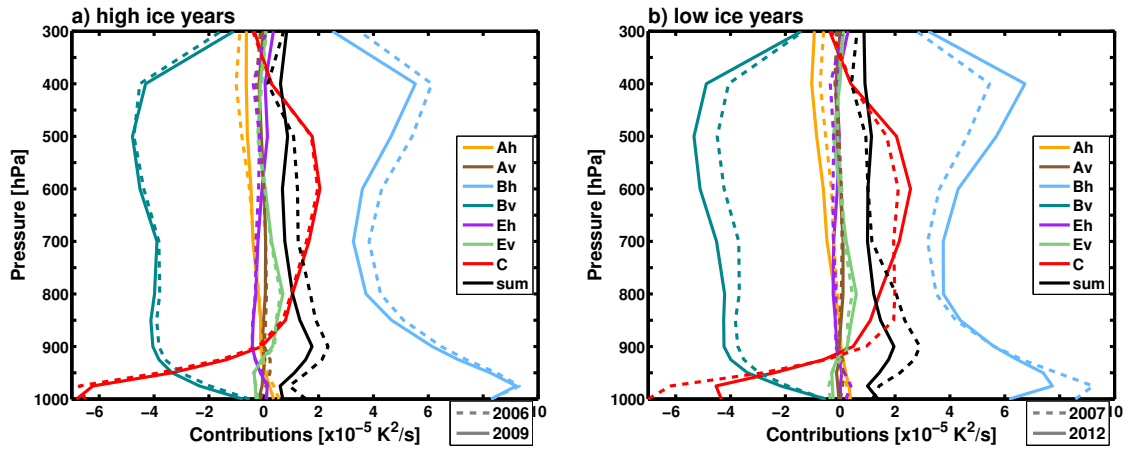


Figure 6.1: Vertical profile of the temporal and domain averaged seven contributions in $10^{-5} K^2/s$ to IV tendency and the sum of all contributions for the ensemble representing the high ice years 2006 (dashed) and 2009 (solid) (a) and the low ice years 2007 (dashed) and 2012 (solid) (b).

The vertical profiles identify strongest influence of the horizontal and vertical ‘baroclinic’ terms (B_h , B_v) on the IV tendency during all years. As summarised in Tabs. 6.1 - 6.4, B_h has positive values in all vertical levels and therefore, contributes to a generation of IV and can be interpreted as a source term for IV. In contrast, the values of B_v are always negative indicating a reduction of the potential temperature IV. Similar to IV, the magnitude of the contributions depend on the height. B_h is smallest in the middle and at the top of the troposphere. Maxima of B_h are calculated at 975 hPa (ca. $8 \times 10^{-5} K^2/s$ in 2012 and ca. $9 \times 10^{-5} K^2/s$ in the other years) and at 400 hPa (ca. $7 \times 10^{-5} K^2/s$ in 2012 and ca. $6 \times 10^{-5} K^2/s$ in the other years). The magnitude of B_v is vertically more uniform (ca. $-5 \times 10^{-5} K^2/s$ to $-4 \times 10^{-5} K^2/s$) between 900 hPa and 400 hPa. Further, B_v is of no importance at the surface and near the tropopause, because the vertical motion is almost zero at these levels. The other terms (apart from C) are up to 100 times smaller compared to B_h and B_v and fluctuate around zero, hence, contribute positively and negatively to the IV tendency depending on the level. Due to the increasing horizontal wind velocity with increasing heights, the magnitude of the horizontal transport term A_h is enhanced in the upper levels. Above 900 hPa, A_h contributes negatively to IV tendency, leading to a reduction of IV.

The diabatic source and sink term C changes its sign depending on the vertical level. Near the ground C is negative with values of ca. $-4 \times 10^{-5} K^2/s$ during summer 2012 and of ca. $-7 \times 10^{-5} K^2/s$ in 2006, 2007 and 2009. In the mid-troposphere it contributes positively to IV tendency with values of ca. $2 \times 10^{-5} K^2/s$. C reaches slightly negative values above 350 hPa. To further analyse the diabatic source and sink term C , the individual contributions to C are investigated. The calculation is based on the covariances between the fluctuations of the potential temperature and the four individual temperature tendencies due to condensation

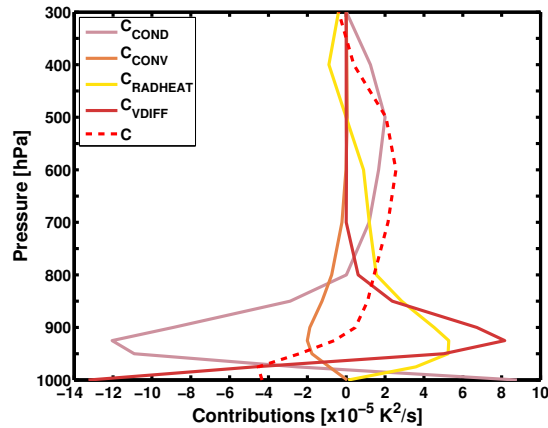


Figure 6.2: Vertical profile of the temporal and domain averaged contribution C in $10^{-5} K^2/s$ (dashed line is identical to red solid line in Fig. 6.1(b)) to IV tendency and the separated parts of the term C meaning the covariances between the fluctuations of potential temperature and the temperature tendencies due to condensation, convection, radiation and vertical diffusion, respectively for the ensemble representing the low ice year 2012. The corresponding figures for the other ensembles are shown in the Appendix Fig. A.1.

C_{COND} , convection C_{CONV} , radiation $C_{RADHEAT}$ and vertical diffusion C_{VDIFF} separately. Fig. 6.2 reveals that the negative contribution of C in the lower troposphere (above 975 hPa) is caused by the temperature tendency due to condensation. This indicates that evaporation occurs in regions with warm potential temperature perturbations and condensation in regions with cold potential temperature perturbations. The term C based on the temperature tendency due to condensation is compensated by the temperature tendencies due to vertical diffusion and radiation below 800 hPa. Above 800 hPa the contribution to IV tendency changes, with C_{COND} leading to a generation with increasing influence with increasing height. In the mid-troposphere up to 500 hPa, the IV tendency is produced by the diabatic heating due to $C_{RADHEAT}$. Physically, the results indicate that regions with warm potential temperature perturbation are heated due to radiation and due to the condensation process. The contributions due to the C_{VDIFF} and C_{CONV} are negligible above 800 hPa. Besides, the latter one contributes only slightly to a reduction of potential temperature IV tendency near the surface. The corresponding vertical profiles of the separated covariances between the fluctuations of potential temperature and the four individual heating rates contributing to the diabatic source and sink term for the other ensembles (see Appendix Fig. A.1) clearly illustrates that the result is independent from the analysed years. No differences between the selected low and high ice years can be detected.

The vertical profiles of the sum of all terms (Fig. 6.1(black lines)) indicate a positive contribution to IV tendency. This is mainly caused due to the fact that the horizontal diffusion (values of up to $-0.3 \times 10^{-5} K^2/s$ near the surface) is neglected in this study.

6.2 Temporal Evolution of the Contributions to IV Tendency

Vertical Averaged Temporal Evolution

The temporal evolution for each contribution (vertical and domain averaged) is shown in Fig. 6.3 and reveals a strong fluctuation in time of all seven terms within all ensembles. Again, the contributions B_h and B_v account most strongly to IV tendency of potential temperature during all years, with B_h being overall positive and B_v negative. The overall positive contribution of B_h to the IV tendency can be explained by examining the two parts of B_h ($\langle \theta'_n \vec{V}'_n \rangle$ and $\vec{\nabla} \langle \theta \rangle$) separately (see Eq. 3.39) like shown in Fig. 6.4(a) for the ensemble 2012. The vertical and domain averaged temporal evolution of both covariances ($\langle \theta'_n U'_n \rangle$ and $\langle \theta'_n V'_n \rangle$, dashed lines) and the horizontal gradients of the ensemble mean potential temperature ($\frac{\partial \langle \theta \rangle}{\partial X}$ and $\frac{\partial \langle \theta \rangle}{\partial Y}$, solid lines) are displayed in this figure. Both covariances contribute mainly with an opposite sign to their corresponding horizontal gradients. This means that the product of the covariances and the gradients is negative leading to a positive B_h due to the multiplication by -2 (see Eq. 3.39). In physical terms this reveals that the covariance of fluctuations ($\langle \theta'_n \vec{V}'_n \rangle > 0$) transport heat towards cold regions, hence contrary to the horizontal ensemble mean potential temperature gradient that represents the increasing temperatures southward ($\vec{\nabla} \langle \theta \rangle < 0$). These fluxes against the mean gradient result in a generation of potential temperature IV tendency.

The negative values of B_v are explained with the help of Fig. 6.4(b) which illustrates that the covariance between the vertical motion and the potential temperature fluctuation ($\langle \theta'_n \omega'_n \rangle$) and the vertical gradient of ensemble mean potential temperature ($\frac{\partial \langle \theta \rangle}{\partial p}$) have the same sign, namely negative. On average the atmospheric stratification is stable ($\frac{\partial \langle \theta \rangle}{\partial p} < 0$). The negative covariance exhibit that warm air rises and cold air sinks, like the mean temperature gradient of the atmosphere. This behaviour results in a reduction of IV tendency. Around the 5th August 2012 the covariance part of the vertical 'baroclinic' term contributes to a stronger reduction of IV tendency with values of ca. $-0.065 \times 10^{-2} K^2/s$.

The vertical averaged term C is mostly positive, but weak (Fig. 6.3). Fig. 6.4(c) shows the temporal evolution of the vertical and domain averaged diabatic source and sink term C based on the covariances between the potential temperature perturbation and the individual temperature tendencies due to radiation, condensation, convection and the vertical diffusion. The radiative heating and the heating due to vertical diffusion are the most important terms of the diabatic source term. However, Fig. 6.2 reveals that the contribution due to the vertical diffusion to the term C is limited to the lower troposphere. In vertical average both terms, always contribute to a generation of IV of potential temperature, whereas, C_{CONV} is negative and therefore, reduces the IV tendency. The impact of C_{COND} fluctuates

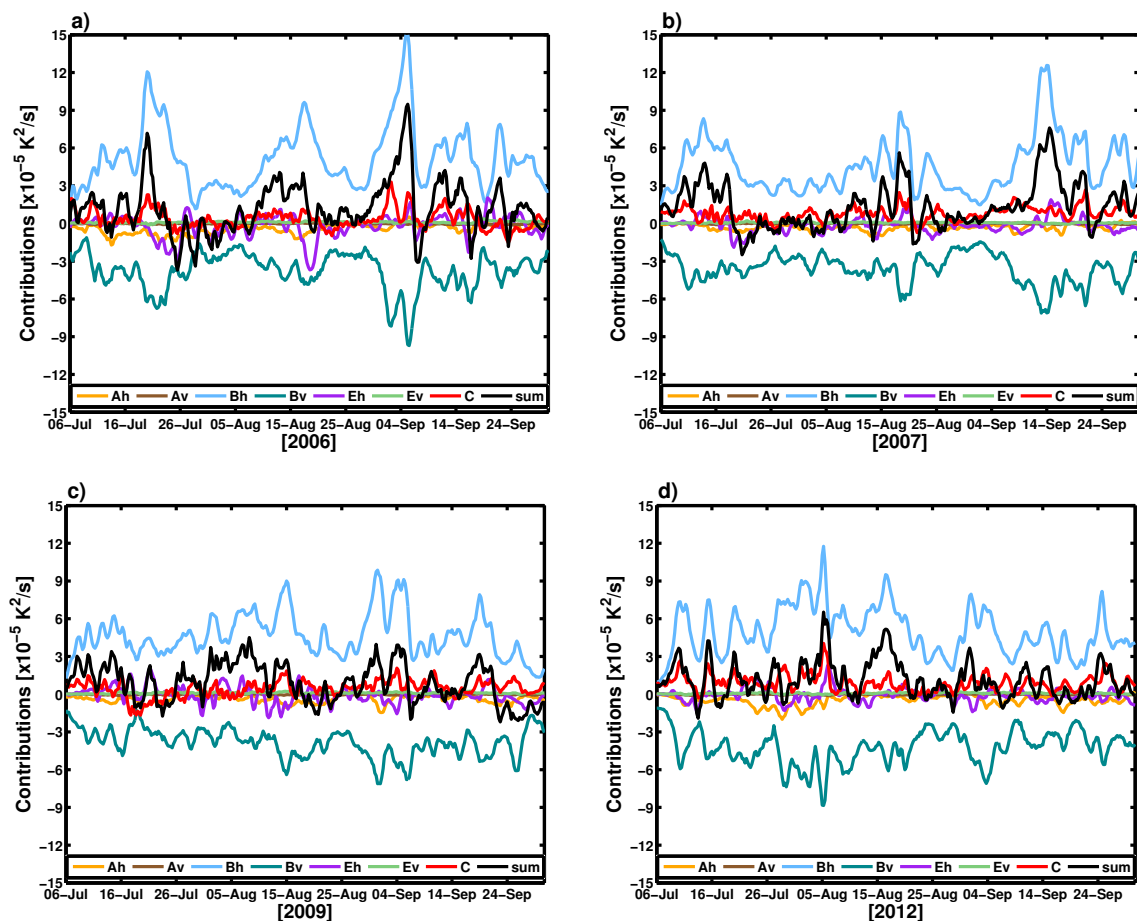


Figure 6.3: Temporal evolution of the vertical and domain averaged seven contributions in $10^{-5} K^2/s$ to IV tendency and the sum of all contributions for the ensembles representing the high ice years 2006 (a) and 2009 (c) and the low ice years 2007 (b) and 2012 (d).

around zero but with strong amplitudes ranging from $-2 \times 10^{-5} K^2/s$ to $2 \times 10^{-5} K^2/s$. On vertical average an intense and only negative contribution of the diabatic term C due to the condensation fluctuations is simulated from the beginning of August to the beginning of September within all considered ensembles (for 2006, 2007 and 2009 not shown). Physically this means a strong reduction of the IV tendency due to condensation processes in cold regions and evaporation in warm regions. Though, from Fig. 6.2 it is known, that the negative vertical averaged contribution due to condensation is mainly induced by the processes in the lower troposphere. The mid-tropospheric heights are influenced by a positive correlation between fluctuations of the potential temperature and the condensative heating meaning that condensation occurs in warm regions. Around the 5th August 2012 (great Arctic cyclone event) the term C based on the covariance between the fluctuations of potential temperature and the temperature tendency due to condensation peaks out and reaches values $> 2 \times 10^{-5} K^2/s$.

The other contributions to potential temperature IV tendency fluctuate around zero (Fig.

6.2. TEMPORAL EVOLUTION OF THE CONTRIBUTIONS TO IV TENDENCY

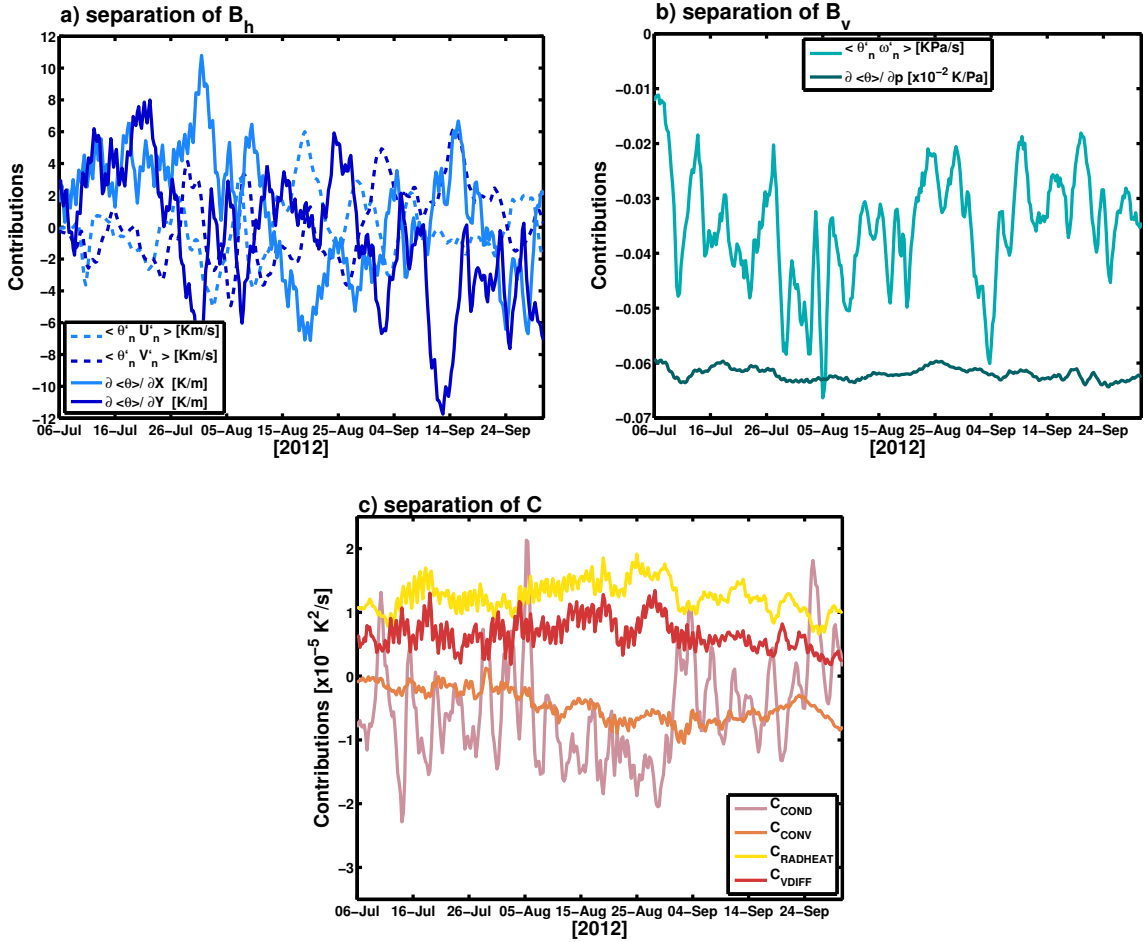


Figure 6.4: Temporal evolution of the domain and vertical averaged separated parts of the contributions B_h (a), B_v (b) and C (c) for the ensemble representing the low ice year 2012. The parts of B_h (a) are the covariances $\langle \theta'_n U'_n \rangle$ and $\langle \theta'_n V'_n \rangle$ (dashed lines) in Km/s and the horizontal gradients of the ensemble mean potential temperature $\frac{\partial \langle \theta \rangle}{\partial X}$ and $\frac{\partial \langle \theta \rangle}{\partial Y}$ (solid lines) in K/m . The parts of B_v (b) are the covariance $\langle \theta'_n \omega'_n \rangle$ in KPa/s and the vertical gradient of ensemble mean potential temperature $\frac{\partial \langle \theta \rangle}{\partial p}$ in $10^{-2} K/Pa$. The parts of C (c) are the covariances between the fluctuations of potential temperature and the temperature tendencies due to condensation, convection, radiation and vertical diffusion, respectively in $10^{-5} K^2/s$.

6.3), because their contribution is in general small (A_v and E_v) or they are balanced over the model domain (with local regions of positive and negative values) (A_h and E_h).

It has to be emphasised that the contributions significantly fluctuate in time as the potential temperature IV itself. The comparison of the temporal evolution of the IV (Fig. 5.5(b)) and of the individual contributions (Fig. 6.3) illustrates mostly a coinciding course like during the period from 27th July to 9th August 2012. Especially B_h and B_v indicate a conform temporal development with IV. More precisely, the correlation between vertical and domain averaged time series of IV and the corresponding time series of B_h is $R = 0.59$ and between IV and B_v $R = -0.69$ during 2012. This is not unexpected, because B_h and B_v are the 'baroclinic' terms, associated with synoptic activity that influences the behaviour of IV

(Giorgi and Bi [2000], Lucas-Picher et al. [2008a], Alexandru et al. [2007], Nikiema and Laprise [2010] and Nikiema and Laprise [2011]). The ensemble 2006 obtains comparable correlations coefficients between the vertical and domain averaged temporal evolution of potential temperature IV and B_h ($R = 0.55$) and B_v ($R = -0.58$). The correlations between vertical and domain averaged time series of IV and the corresponding time series of the 'baroclinic' terms are weaker within the ensemble 2007 and 2009. However, during 2009 the correlation reaches values of $R = 0.47$ between the domain averaged IV at 925 hPa and the corresponding B_h and $R = -0.65$ for the corresponding B_v . Additionally, during 2009 the correlation between the domain averaged temporal evolution of IV and the diabatic source and sink term C ($R = -0.35$ on vertical average and $R = -0.43$ at 925 hPa)) is strongest compared to the correlation coefficients that are achieved in the other years. Apart from some negative peaks the sum of all contributions (Fig. 6.3(black lines)) is positive due to the strong positive contribution of B_h and C which are not fully balanced by B_v . However, during 2006 (Fig. 6.3(a)) and 2007 (Fig. 6.3(b)) the positive and negative peaks of the sum of all terms reach more intense magnitudes.

Temporal Evolution in Different Heights

Fig. 6.5 illustrates the temporal evolution of the seven contributions to the IV tendency of potential temperature at three different height levels (925 hPa, 500 hPa and 300 hPa) for summer 2012. The corresponding time series for the other years show a very similar behaviour of the contributions and therefore, they are shown in the Appendix (Sec. A.2.2). B_h has the strongest and always positive contribution to the IV tendency of potential temperature at all levels. This positive contribution is associated with a generation of IV. However, the values become smaller with increasing height. At 925 hPa and 500 hPa the values reach ca. $6 \times 10^{-5} K^2/s$ and at 300 hPa they are on average reduced to ca. $3 \times 10^{-5} K^2/s$. It is noteworthy that a relationship between the temporal evolution of the term B_h at 500 hPa and the temporal evolution of the ensemble averaged EGR (estimated between 850 hPa and 500 hPa, not shown) is found for all of the four ensembles. Time periods with high (low) positive contribution of B_h to IV tendency are associated with high (low) EGR.

The vertical 'baroclinic' term (B_v) has a negative contribution to the IV tendency of potential temperature during the whole time period at 925 hPa and 500 hPa, and also mostly at 300 hPa (Fig. 6.5). This negative contribution leads to a reduction of the IV of potential temperature. B_v is almost a half magnitude smaller than B_h at 925 hPa and at 300 hPa and there are also short time periods when B_v reaches even positive values at 300 hPa within all simulated ensembles.

The sign of term C differs with the height levels as also shown in Figs. 6.1, 6.2 and Tabs. 6.1

6.2. TEMPORAL EVOLUTION OF THE CONTRIBUTIONS TO IV TENDENCY

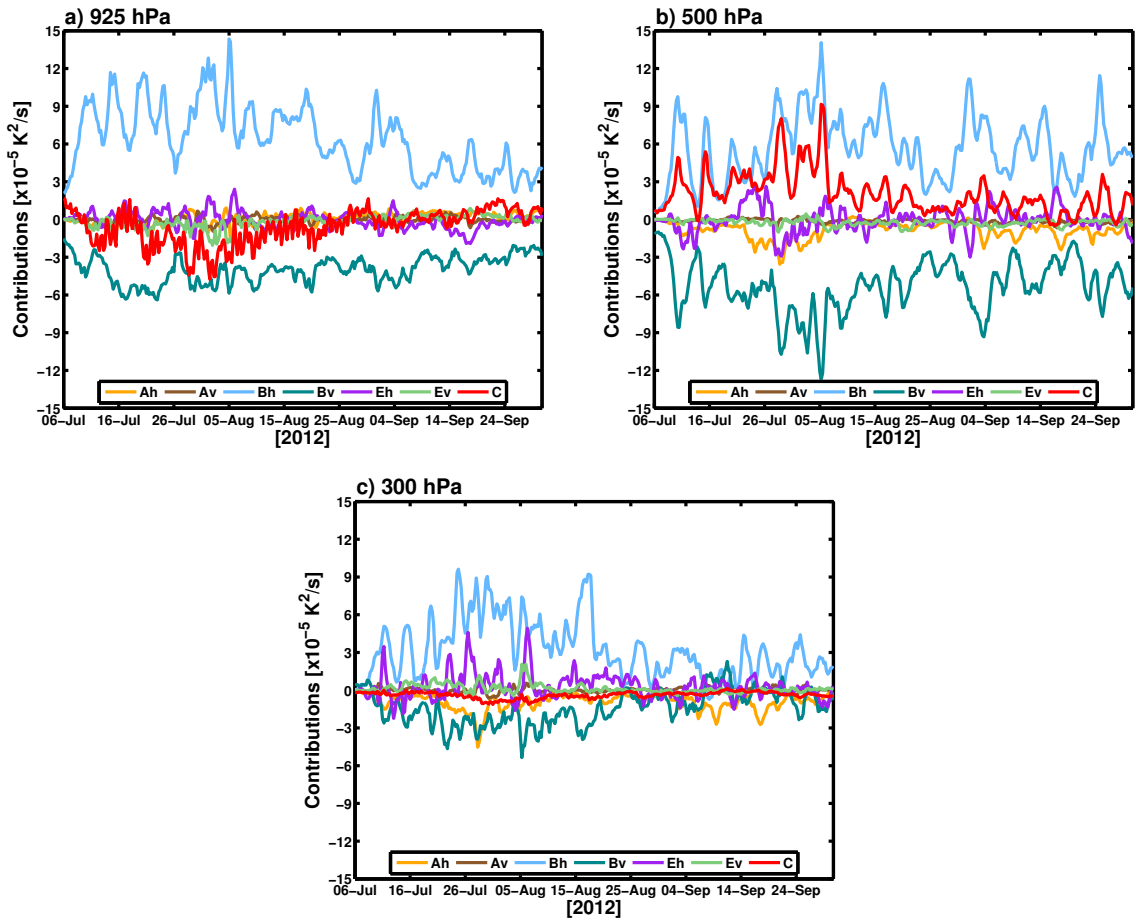


Figure 6.5: Temporal evolution of the domain averaged seven contributions in $10^{-5}K^2/s$ to IV tendency at 925 *hPa* (a), 500 *hPa* (b) and 300 *hPa* (c) for the ensemble representing the low ice year 2012. The corresponding figures for the ensembles representing the low ice year 2007 and the high ice years 2006 and 2009 are shown in the Appendix Figs. A.4, A.2 and A.3.

- 6.4. During 2012, *C* has highest absolute values during the end of July and the beginning of August (coinciding with the occurrence of the great Arctic cyclone event and strongest sea ice reduction) at 925 *hPa* and 500 *hPa*. In 2006, 2007 and 2009 (see Appendix, Figs. A.2, A.4 and A.3), the diabatic source and sink term *C* follows the temporal evolution of the potential temperature IV, like B_h and B_v , but with less intensity.

As already shown in Fig. 6.1, the horizontal transport term A_h is negative above 925 *hPa* and becomes more important with increasing height (Fig. 6.5). The magnitude of E_h and E_v varies strongly with time. Both terms can fluctuate around zero or peak out positively and negatively. The peaks reach highest values of up to $5 \times 10^{-5}K^2/s$ in upper levels in the ensemble 2012 (Fig. 6.5). Within the other ensembles (see Appendix, Figs. A.2, A.4 and A.3) the third-order terms (E_h , E_v) have strongest influence on IV tendency of potential temperature at 500 *hPa*.

Concerning the analyses between the low and high ice years and the influence on the

dynamical and diabatic contributions to the IV tendency, the results indicate that such a relation is weak (compare Fig. 6.5 with Figs. A.2, A.4 and A.3). This is not unexpected due to the results that were found for the IV itself. Of course, the temporal fluctuation differs from year to year, but the general characteristics are the same.

6.3 Spatial Distribution of the Contributions to IV Tendency

The spatial distribution of the contribution to the IV tendency of potential temperature reveals regions that have strong influence on the IV. To get an overview about the averaged pattern, the results are shown for the temporal and vertical averaged terms. Again, the patterns look quite similar between the four analysed ensembles and it is hard to detect a relationship between the contributions to the IV tendency and the high ice years (2006, 2009) and the low ice years (2007, 2012). Hence, the results are exemplarily shown for the ensemble 2012 and special situations are marked out for the other ensembles that are presented in Appendix Figs. A.5, A.7 and A.6.

Fig. 6.6 illustrates the spatial patterns of the temporal and vertical averaged seven contributions to IV tendency during 2012. Again, positive values mean an increase and negative values a reduction of potential temperature IV tendency, indicating sources and sinks for the IV, respectively. Pronounced regionally different patterns are obvious for the different terms.

Horizontal and Vertical Transport Terms A_h and A_v

In contrast to the domain averaged results (see Secs. 6.1 and 6.2) the horizontal and vertical transport terms A_h and A_v have a strong, but have negative and positive impacts on the IV tendency (Figs. 6.6(a), (b)). Therefore, they contribute to generate and reduce the IV depending on the region. Besides, A_h is of the same magnitude as the 'baroclinic' terms B_h and B_v (Fig. 6.6(c), (d)). However, A_v is 100 times smaller than A_h . Positive transport terms indicate that the IV of potential temperature is moved towards this regions, either from outside of the model domain or from regions where the transport term is negative. Consequently, negative transport terms reveals regions which lose IV tendency towards the outside of the model domain or to regions with positive transport terms. The negative values of A_h can be found mostly over the Arctic Ocean (with maxima over the Beaufort Sea in 2012) and Greenland. The positive values, leading to a generation of IV, occur mainly over the land areas. Centres of IV generation due to transport into the model domain, are mostly found over eastern Siberia and Greenland Sea. These regions are

6.3. SPATIAL DISTRIBUTION OF THE CONTRIBUTIONS TO IV TENDENCY

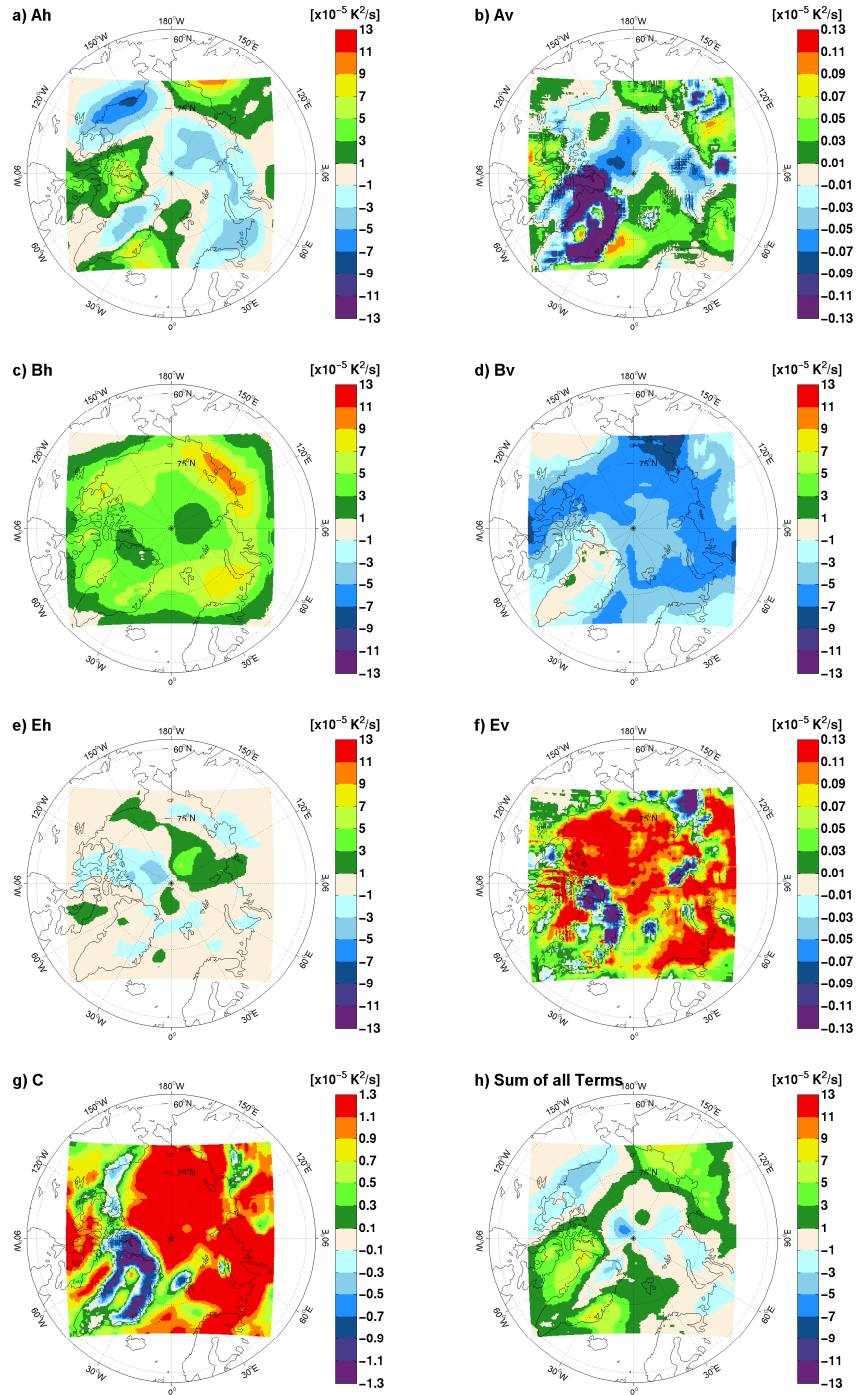


Figure 6.6: Spatial distribution of the temporal and vertical averaged seven contributions in $10^{-5} K^2/s$ to IV tendency ((a)-(g)) and the sum of all contributions in $10^{-5} K^2/s$ (h) for the ensemble representing the low ice year 2012. The contribution C is 10 times and the contributions A_v and E_v are 100 times smaller than the other contributions, therefore, the colorbars are adapted. The corresponding figures for the ensembles representing the low ice year 2007 and the high ice years 2006 and 2009 are shown in the Appendix Figs. A.7, A.5 and A.6.

identified as centres of originating cyclones (e. g. East Siberia) [Serreze et al., 2001]), of high cyclone centre counts (e. g. Greenland Sea) [Serreze and Barrett, 2008] and as areas

where cyclones enter the Arctic Ocean from East Siberia [Serreze et al., 1993] and from the Greenland Sea [Sorteberg and Walsh, 2008]. The spatial distribution of A_h of the other ensembles are quite similar concerning the regions of positive and negative contributions (see Appendix Fig. A.5(a) and Fig. A.6(a)), apart from 2007 (Fig. A.7(a)) when a centre of positive A_h is formed over the Barents and Kara Seas. Despite the general similarity the patterns reveal some small differences between the ensembles like the tongue of positive A_h that ranges from the Queen Elizabeth Islands into the Arctic Ocean which is more pronounced during 2006 (Fig. A.5(a)) and 2007 (Fig. A.7(a)) and extends further in a northward direction, compared to 2012. In comparison to A_h , the positive values of A_v are more widespread and occur over the Atlantic side of the Arctic and all land (apart from Greenland), and negative A_v contributions appear over the central Arctic Ocean and Greenland.

Horizontal and Vertical 'Baroclinic' Terms B_h and B_v

The temporal and vertical averaged horizontal 'baroclinic' term B_h (Fig. 6.6(c)) contributes overall positively to the IV tendency of potential temperature. In general, B_h follows the pattern of high values along the coastlines with centres of strong contribution located at the coast of Laptev/East Siberian Sea and over the Barents Sea $7 \times 10^{-5} K^2/s$ and higher (up to $11 \times 10^{-5} K^2/s$). Smaller contributions are calculated over the central Arctic Ocean and Greenland. Within the ensembles representing the high ice years 2006 (Fig. A.5(c)) and 2009 (Fig. A.6(c)), the contribution of B_h has the same spatial pattern but is more intense, compared to the low ice years 2007 (Fig. A.7(c)) and 2012 (Fig. 6.6(c)) where the centres over Laptev/East Siberian Sea and over the Barents Sea are weaker. The influence of B_h is induced by the movement of warm potential temperature perturbations ($\langle \theta'_n \vec{V}'_n \rangle > 0$) towards cold regions against the mean potential temperature gradient ($\vec{\nabla} \langle \theta \rangle < 0$).

Unlike B_h , B_v (Fig. 6.6(d)) contributes to reduce the IV in the whole model domain. There are no clear centres of a strong negative contribution, but the region along the Russian coast and across the Beaufort Sea shows larger negative values of up to $-7 \times 10^{-5} K^2/s$ in 2012. For 2006 (Fig. A.5(d)), 2007 (Fig. A.7(d)) and 2009 (Fig. A.6(d)) B_v is smaller over the Beaufort Sea, but the strong negative contribution along the Russian coast is noticeable as well. Smallest absolute contribution of B_v to the IV tendency of potential temperature is computed over land, particularly over Alaska and Greenland. On the temporal average the term B_v contributes to a reduction of IV tendency due to the rise of warm and the descent of cold temperature fluctuations. This behaviour is conform with the mean atmospheric stratification and therefore, inhibits the production of IV.

As described for the domain averaged analysis, the 'baroclinic' terms B_h and B_v are the

6.3. SPATIAL DISTRIBUTION OF THE CONTRIBUTIONS TO IV TENDENCY

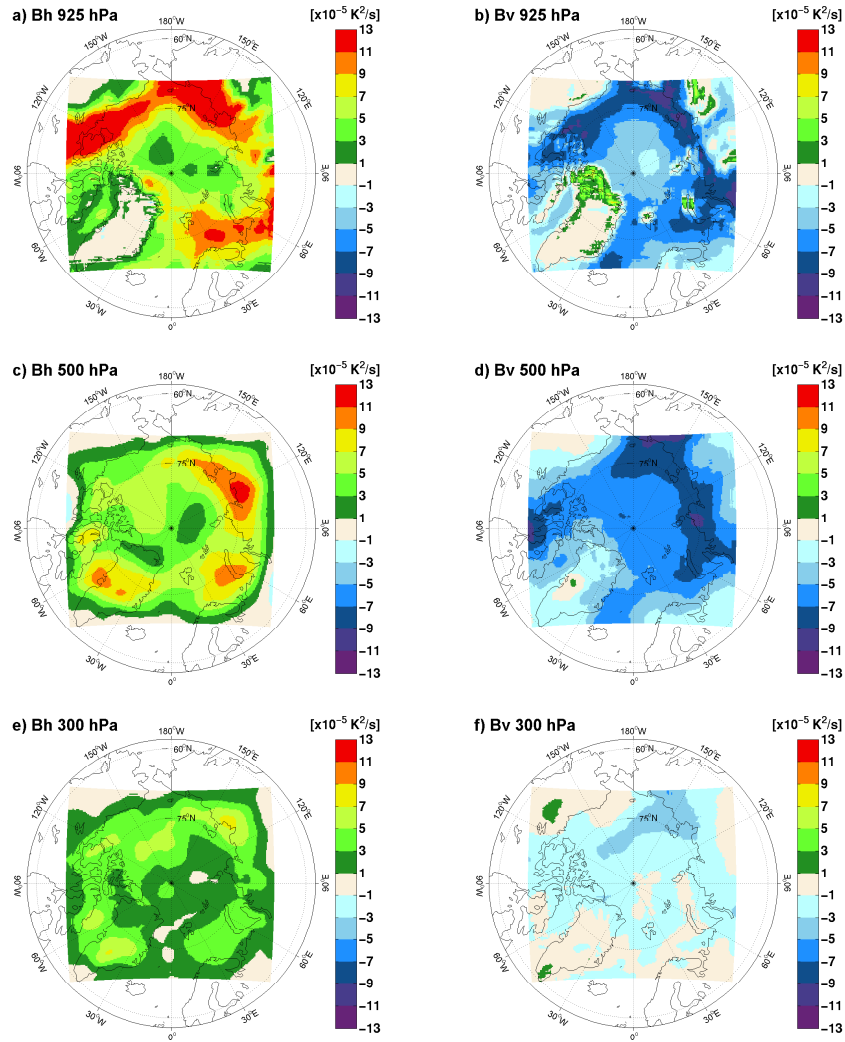


Figure 6.7: Spatial distribution of the temporal averaged contributions B_h (left column) and B_v (right column) in $10^{-5} K^2/s$ to IV tendency at 925 hPa, 500 hPa and 300 hPa (rows) for the ensemble representing the low ice year 2012. The corresponding figures for the ensembles representing the low ice year 2007 and the high ice years 2006 and 2009 are shown in Sec. 6.4 in Fig. 6.9 for B_h and Fig. 6.10 for B_v .

most important ones. Therefore, their spatial distribution is investigated more deeply for the ensemble 2012 at different vertical levels (Fig. 6.7). The horizontal 'baroclinic' term B_h is positive overall and reaches its maximum at 925 hPa. Along the coastlines B_h indicates values higher than $13 \times 10^{-5} K^2/s$. Apart from there, the values range between $1 \times 10^{-5} K^2/s$ and $7 \times 10^{-5} K^2/s$. The magnitudes become weaker with increasing height and at 300 hPa B_h has values lower than $7 \times 10^{-5} K^2/s$. But, the spatial patterns (locations of the maxima) are quite similar at all height levels.

Similar to B_h , the term B_v (Figs. 6.7(b), (d), (f)) shows quite equal spatial distributions with highest contribution along the coastlines, but its sign is negative, illustrating a reduction of IV. The absolute values of B_v are smaller (mostly $> -9 \times 10^{-5} K^2/s$, and rarely $< -11 \times 10^{-5} K^2/s$) compared to B_h . At the lower to the mid-tropospheric level the magnitudes of

contributions over the Arctic Ocean range between $-1 \times 10^{-5} K^2/s$ to $-5 \times 10^{-5} K^2/s$ (at 925 hPa) and ca. $-7 \times 10^{-5} K^2/s$ at 500 hPa.

The EGR was investigated in Sec. 4.3 and within all ensemble years a corresponding belt of high potential for baroclinic instability (see Fig. 4.10) was simulated. Particularly high EGRs are found for 2012 over northern Siberia and in the north of Northern America. This belt of high horizontal and vertical 'baroclinic' contribution terms along the coastlines of the Arctic Ocean at lower and mid-tropospheric levels coincides with the belt of high frontal frequency examined by Serreze et al. [2001]. They found that this frontal zones during summer are caused by the intense temperature gradient between the cold Arctic Ocean and the relatively warm snow-free land.

At upper tropospheric levels the influence of B_v to IV tendency of potential temperature becomes weak and rarely reaches values of $-5 \times 10^{-5} K^2/s$, probably due to the decreasing vertical motion at upper atmospheric levels. In contrast, B_h is still significant at the higher levels with magnitudes from $1 \times 10^{-5} K^2/s$ to $9 \times 10^{-5} K^2/s$.

The height dependency of the ensembles 2006, 2007 and 2009 will be examined in Sec. 6.4. The spatial distributions of the horizontal (Fig. 6.9) and vertical (Fig. 6.10) 'baroclinic' terms at the heights of 925 hPa, 500 hPa and 300 hPa are quite similar to the one showed for the ensemble 2012 with more or less the same magnitudes and centres of high contributions.

Diabatic Source and Sink Term C

The temporal and vertical averaged diabatic source and sink term C (Fig. 6.6(g)) has a ten times smaller contribution to the IV tendency than A_h , B_h and A_v , due to the compensation of positive and negative contributions in the vertical as shown in Figs. 6.1 and 6.2. A small reduction of IV occurs over the Beaufort Sea, Fram Strait and at the coastlines of Greenland within all ensembles. Over most other areas C contributes exclusively to the generation of IV. For 2006 (Fig. A.5(g)) followed by 2009 (Fig. A.6(g)) the positive contributions over the Arctic Ocean are mostly smaller than for 2007 (Fig. A.7(g)) and 2012.

The different parts of the C meaning the covariances between the fluctuations of potential temperature and the temperature tendencies due to condensation, convection, radiation and vertical diffusion reveals that on temporal and vertical average (not shown) the heating rates due to condensation and convection contributes slightly negative to the IV tendency of potential temperature, while the heating rate due to the vertical diffusion and the radiation contributes slightly positive. However, as mentioned before, the diabatic source and sink term based on the condensation and convection is negative below 800 hPa and positive (C_{COND}) and zero (C_{CONV}) in the upper levels. The spatial patterns of the individual contributions are shown at 925 hPa for the ensemble 2012 (Fig. 6.8). The impact of the

6.3. SPATIAL DISTRIBUTION OF THE CONTRIBUTIONS TO IV TENDENCY

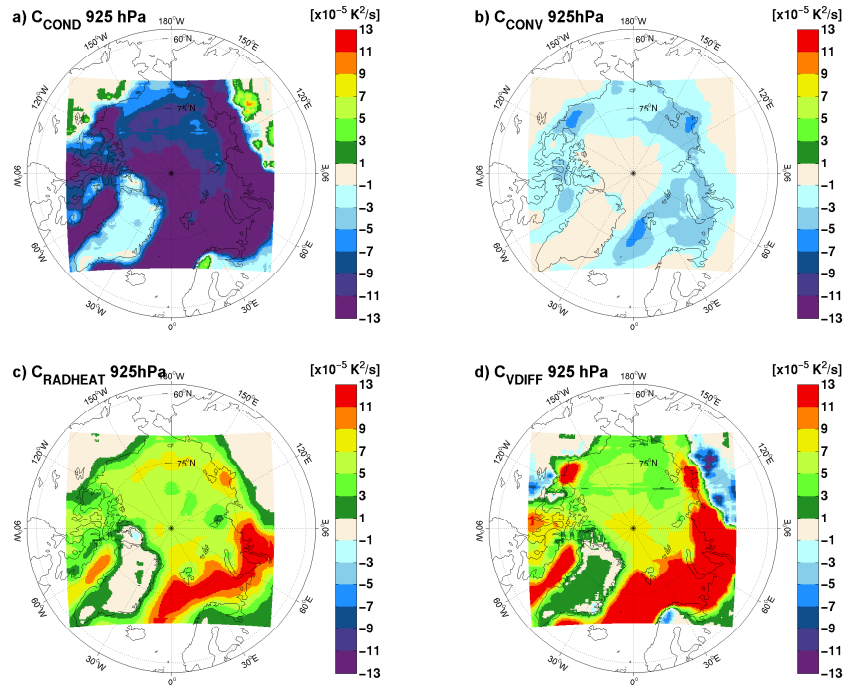


Figure 6.8: Spatial distribution of the temporal averaged separated parts of the contribution C in $10^{-5} K^2/s$ to IV tendency at 925 hPa for the ensemble representing the low ice year 2012. The parts of C are the covariances between the fluctuations of potential temperature and temperature tendencies due to condensation (a), convection (b), radiation (c) and vertical diffusion (d), respectively. The corresponding figures for the temperature tendencies due to condensation and convection for the low ice year 2007 and the high ice years 2006 and 2009 are shown in Sec. 6.4 in Fig. 6.11

temperature tendency due to convection is much weaker compared to the condensation. It reaches maximum values of up to $-7 \times 10^{-5} K^2/s$ and is limited to the coastlines (see Fig. 6.8(b)). The reduction of IV tendency due to C_{COND} (Fig. 6.8(a)) is stronger (values of up to $-13 \times 10^{-5} K^2/s$) and its impact covers the whole Arctic domain. However, the intensity is weaker from the Chukchi Sea into the Arctic Ocean. This region was affected by the tongue of low pressure during August 2012 (see Figs. 4.6(a), (b)) including the great Arctic cyclone event during the beginning of August 2012 that leads to an intense sea ice retreat. Like examined by Porter et al. [2012] and references therein, this open water leads to an enhanced evaporation that can result in increased condensation over the ice free ocean. Obviously, this process is connected with a reductive contribution to the IV tendency. However, the impact is weaker compared to the surroundings hence, this condensation process over the Chukchi Sea tends towards a production of IV. There are some spots over Siberia and Northern America where the C_{COND} contributes positively to IV tendency even near the surface. At the mid-atmospheric heights, the positive contribution due to condensation is strongest over the Barents and Kara Seas and at 300 hPa over the Laptev Sea (not shown). The positive contribution to IV tendency of potential temperature due to the covariance between the potential temperature fluctuations and heating rate by radiation

(Fig. 6.8(c)) and vertical diffusion (Fig. 6.8(d)) are induced by diabatic heating of warm perturbations. Near the surface $C_{RADHEAT}$ contributes overall positively to IV tendency, especially from the Norwegian Sea to the Kara Sea with values of up to $13 \times 10^{-5} K^2/s$ and over the Laptev Sea and the Baffin Bay with values of $10 \times 10^{-5} K^2/s$. This corresponds with the regions that were ice-free from the beginning of the simulations (see Fig. 4.2). The same dependency is found in the ensemble simulations for the other years as well, but with a weaker intensity during 2009 and especially during 2007. The positive contribution could be interpreted by radiation processes that heat the warm perturbations over the open ocean resulting in a generation of IV tendency, probably due to the stronger absorption of short-wave radiation caused by the reduced surface albedo and the resulting increased upward long-wave radiation. At 500 hPa (not shown) the influence of the radiation is negative over the central Arctic Ocean and positive over the Laptev Sea, Northern America and the western part of Greenland. The diabatic heating due to radiation becomes overall negative at 300 hPa (not shown), especially over the East Siberian Sea. Like $C_{RADHEAT}$ the influence of the C_{VDIFF} is positive to the IV tendency of potential temperature with the same regions of strong contribution at 925 hPa, but even more intense. Hence, the turbulent fluxes over the open ocean lead to a heating of the warm air, that strongly generates the IV. This influence decreases with increasing height and is zero above 700 hPa.

Horizontal and Vertical Third-order Terms E_h and E_v and the Sum of all Terms

The values of the third-order terms E_h and E_v (Figs. 6.6(e), (f)) differ about an order of 100 to each other, with E_v being the smaller one. Both are weak compared to the horizontal transport term A_h and the horizontal and vertical 'baroclinic' terms B_h and B_v contribute to a generation and reduction of IV in dependence on the location. The contribution of E_h is mostly limited to the Arctic Ocean and rarely reaches values of $\pm 4 \times 10^{-5} K^2/s$ in vertical and temporal average. E_v has almost an overall positive but small contribution with highest values over the ocean (ca. $0.13 \times 10^{-5} K^2/s$). The ensemble 2007 reveals a smaller positive contribution over the Arctic Ocean and reaches only values of up to $0.09 \times 10^{-5} K^2/s$ in the Beaufort Sea (Fig. A.7(f)). The negative values are found mostly at some coastlines and East Siberia (within all ensembles).

The sum of all seven terms contributing to the IV tendency (Fig. 6.6(h)) is positive, meaning a generation of IV over the eastern Russian Arctic, the Baffin Bay and the Greenland Sea, and negative values occur over the Arctic Ocean, Alaska and the western Russian Arctic. It seems, that the sum of all contributions follows the horizontal transport term A_h (Fig. 6.6(a)). As mentioned before, the spatial distributions reveal that A_h (Figs. 6.6(a)) reaches the same magnitude as the 'baroclinic' terms, but contributes positively and negatively to IV depending on the region. Therefore, the spatial average leads to a cancelation of A_h ,

resulting in small values considering the vertical profile and temporal evolution (Figs. 6.1, 6.3 and 6.5). From this it is also obvious that the sum of all contributions (Fig. 6.6(h)) provides a pattern which is quite similar to the spatial distribution of A_h and not to B_h and B_v , which are compensating each other. The sum of all terms within the other ensembles (Figs. A.5, A.7 and A.6(h)) behaves similar to 2012. However, in 2007 the generation of IV tendency is more widespread (Fig. A.7(h)) and a reduction is found only over the Laptev Sea and over/north of Greenland. This high positive net tendency is summarised in Tab. 6.3.

6.4 Impact of the Sea Ice Distribution on the IV and its Contributions

One idea of the study was to investigate the influence of the sea ice cover on the IV and its dynamical and diabatic contributions. The sea ice cover modifies the exchange of moisture and heat between the atmosphere and the ocean and one might expect on IV.

The impact of reduced summer sea ice cover on the atmosphere was analysed and discussed recently in detail by Porter et al. [2012]. They build two ensembles with 15 members covering the time period from mid June to the beginning of December for the years 1994 to 2008 with the WRF model. The model was driven by the summer sea ice conditions of 1996 and 2007. Under low ice condition enhanced sensible and latent heat fluxes that leads to an increased $2m$ air temperature and specific humidity during the early autumn. This warming is first limited to the lower atmosphere but from the mid of September the temperature rises also in higher levels (up to $12 km$) compared to the run that was performed with the high ice condition. The changing temperature and specific humidity influence the cloud cover resulting in less low-level clouds and increased mid-level clouds during the low ice condition due to the decrease of static stability (Schweiger et al. [2008], Porter et al. [2012]). The surface albedo is reduced in the case of low ice cover and hence, absorption is enhanced leading to a reduced net surface short-wave radiation and former to an increased net upward long-wave radiation over the open ocean. The response of all these feedbacks due to the low ice conditions last until mid-autumn (Strey et al. [2015], Porter et al. [2012])

In this study two high ice years (2006 and 2009) and two low ice years (2007 and 2012) are selected from the years of this millennium. The above-mentioned physical processes and effects concerning the influence of the ice cover on the atmosphere are also valid for these simulations. However, other than expected, an effect of the sea ice cover on IV could not be detected. No impact on IV in the atmospheric circulation is found. A weak effect, restricted

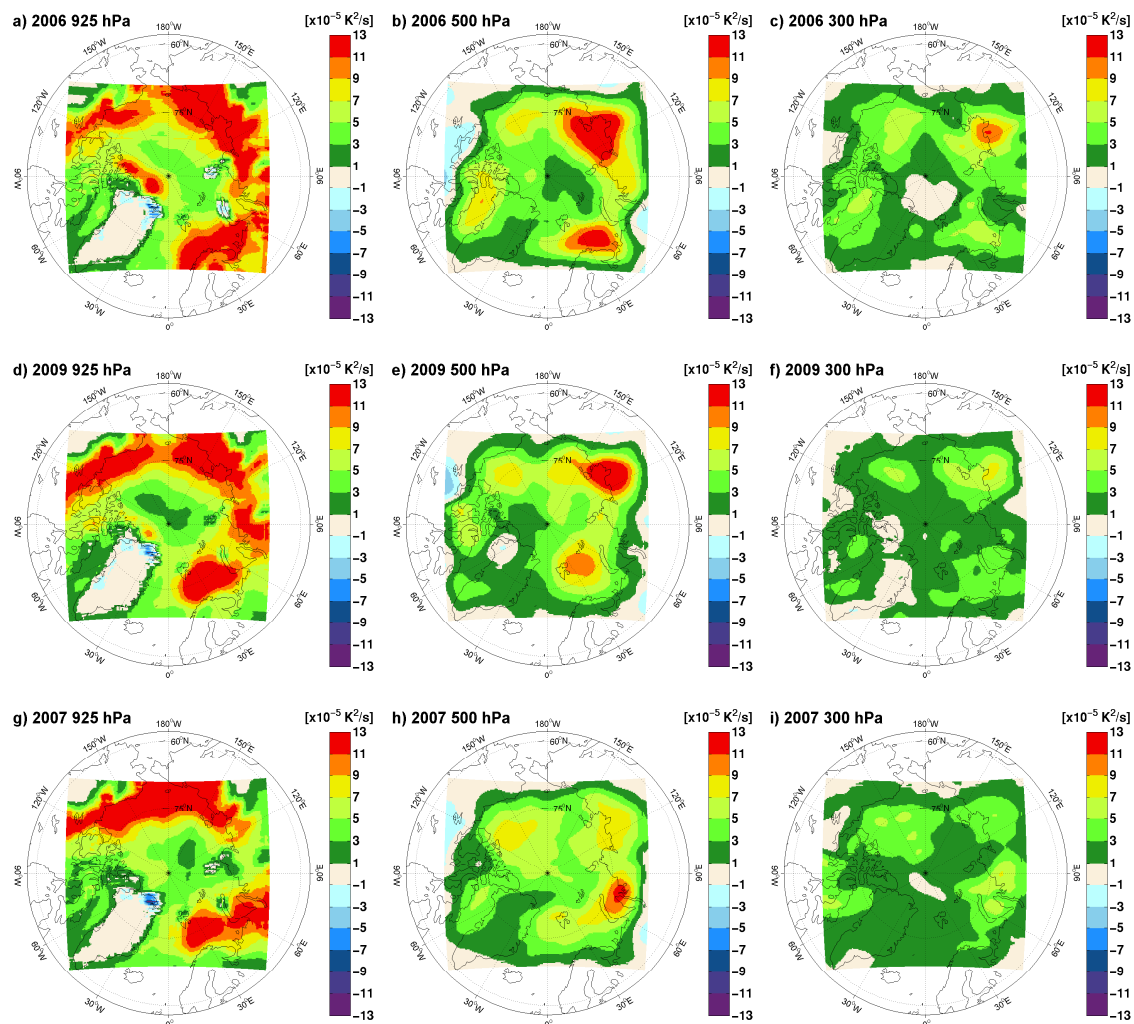


Figure 6.9: Spatial distribution of the temporal averaged contribution B_h in $10^{-5} K^2/s$ to IV tendency at 925 hPa, 500 hPa and 300 hPa (columns) for the ensembles representing the high ice years 2006 and 2009 (first and second row) and the low ice year 2007 (third row). The corresponding figures for the low ice year 2012 are shown in Fig. 6.7(left column).

to the lower atmosphere, is found for the IV of potential temperature. The temporal and domain averaged vertical profiles (Fig. 5.5(a)) reveal that in lower levels the IV is larger for high ice years (2006, 2009) compared to the low ice years (2007, 2012). Further, Fig. 5.6 suggests that the IV at 925 hPa tends to decrease from July to September, like the sea ice extent as well. Besides, the spatial distribution at 925 hPa (Fig. 5.7(left column)) illustrates that the IV is lower for the low ice years, but the locations of maximum IV do not reflect the ice-free locations. At the upper levels the impact of the sea ice cover on the IV is not seen. The atmospheric dynamics probably is more important for the development of the IV. Therefore, it is not surprising that the analysis of the seven individual contributions to IV tendency (see Chapter 6) did not reveal a correlation between the sea ice condition and the contribution terms, apart from some weak relations that are found for B_h , B_v and

6.4. IMPACT OF THE SEA ICE DISTRIBUTION ON THE IV AND ITS CONTRIBUTIONS

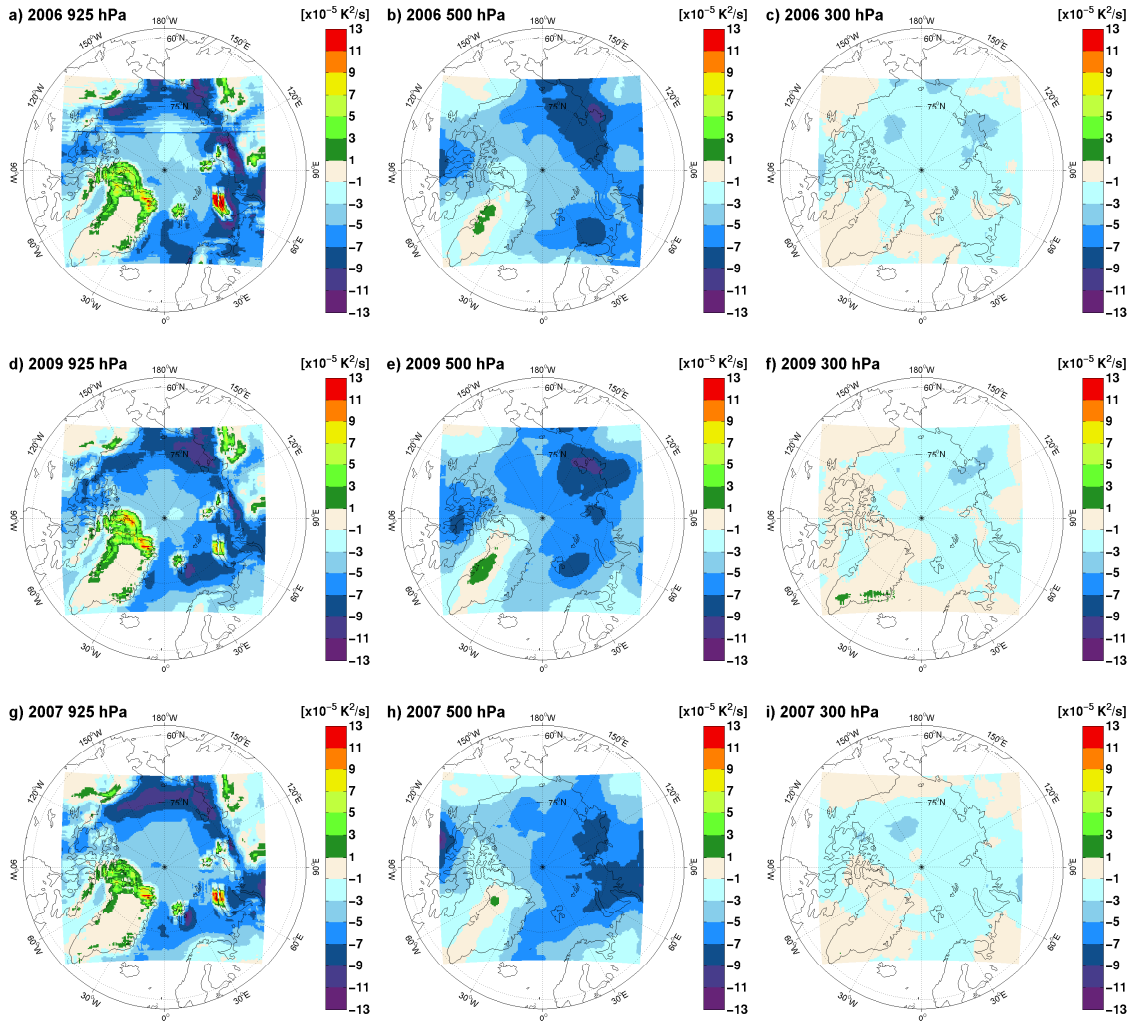


Figure 6.10: Spatial distribution of the temporal averaged contribution B_v in $10^{-5} K^2/s$ to IV tendency at 925 hPa, 500 hPa and 300 hPa (columns) for the ensembles representing the high ice years 2006 and 2009 (first and second row) and the low ice year 2007 (third row). The corresponding figures for the low ice year 2012 are shown in Fig. 6.7(right column).

C. Hence, this section focuses on the behaviour of the horizontal and vertical 'baroclinic' contributions (B_h and B_v) and the diabatic source and sink term C with respect to the sea ice distribution. The analysis of the vertical profiles of the temporal and domain averaged contributions (Fig. 6.1) do not show any distinct classification concerning low and high ice years. Only a less intense impact of the contribution C near the surface (ca. $-4 \times 10^{-5} K^2/s$ compared to ca. $-6 \times 10^{-5} K^2/s$ during 2006, 2007 and 2009) is noticed for the low ice year 2012. Similarly, a weaker contribution by the horizontal 'baroclinic' term B_h near the surface is found during 2012.

However, the analysis of the spatial distributions of the contributions may enables a classification related to the sea ice extent. The vertical and temporal averaged horizontal 'baroclinic' term B_h reveals that the regions of high contribution over the Laptev/East

Siberian Seas and over the Barents Sea are weaker during the low ice years 2007 (see Fig. A.7(c)) and 2012 (see Fig. 6.6(c)) compared to the high ice years 2006 (see Fig. A.5(c)) and 2009 (see Fig. A.6(c)). For more details Fig. 6.9 shows the temporal averaged contribution B_h at 925 hPa, 500 hPa and 300 hPa for the high ice years 2006 and 2009 and the low ice year 2007. The corresponding results for the low ice year 2012 were shown in Figs. 6.7(left column). The area between 90° E and 120° E covering Siberia B_h is smaller during low ice years (maximum $9 \times 10^{-5} K^2/s$ during 2012 and maximum $7 \times 10^{-5} K^2/s$ during 2007). The local maxima of B_h over the Laptev Sea area at 300 hPa is slightly less pronounced during the low ice years compared to the high ice condition. This behaviour is also partly noticed at 500 hPa.

The investigation of the vertical 'baroclinic' term B_v (Fig. 6.10 for 2006, 2009 and 2007, Fig 6.7(right column) for 2012) concerning the sea ice distribution reveals, that at 925 hPa the impact of B_v is slightly stronger over the Chukchi/Beaufort Seas when sea ice is reduced. However, at 500 hPa the reduced sea ice seems to lead to a weaker influence of B_v over the Laptev Sea and East Siberian Sea. This is not true for 2012, but for 2007, when the centre of strong negative contribution is limited to the Laptev Sea only. During 2012 (Fig 6.7(d)) a strong negative contribution due to B_v over the whole Russian coast is found. The obtained results concerning the 'baroclinic' contributions B_h and B_v are quite unexpected, because it is known that the IV depends on the synoptic situation (e. g. Caya and Biner [2004], Rinke et al. [2004], Alexandru et al. [2007]). Further, a correlation between the synoptic activity and the reduced sea ice is found (Jaiser et al. [2012], Porter et al. [2012]). They argued that the reduced sea ice leads to an enhanced atmospheric heating that results in a modified baroclinicity. In this work a relation between the EGR and the B_h and B_v is found however, the relation to the sea ice is hard to detect.

The diabatic source and sink term C for 2012 is shown in Fig. 6.6(g) and for 2006, 2007 and 2009 in Figs. A.5(g), A.7(g) and A.6(g). Under low sea ice conditions the influence of C becomes stronger and reaches values of up to $1.5 \times 10^{-5} K^2/s$ over the Arctic Ocean during summer 2012. The individual covariances between the potential temperature fluctuation and the temperature tendencies due to condensation (C_{COND}) and convection (C_{CONV}) are shown at 925 hPa for the high ice years 2006 and 2009 (Fig. 6.11(first and second row)), and the low ice years 2007 (Fig. 6.11(third row)) and 2012 (Fig. 6.8(a), (b)). Concerning the covariance C_{COND} it is found that the negative influence is generally weaker over the central Arctic Ocean compared to the surroundings. It seems that with decreasing sea ice concentration the reduction due to the C_{COND} over the Chukchi Sea is more pronounced. However, this is not valid for the low ice year 2012 in this area (Fig. 6.8(a)). The Chukchi Sea was affected by the great Arctic cyclone event that leads to a strong sea ice retreat during the beginning of August 2012. May this rapid sea ice loss induces a weaker reducing

6.4. IMPACT OF THE SEA ICE DISTRIBUTION ON THE IV AND ITS CONTRIBUTIONS

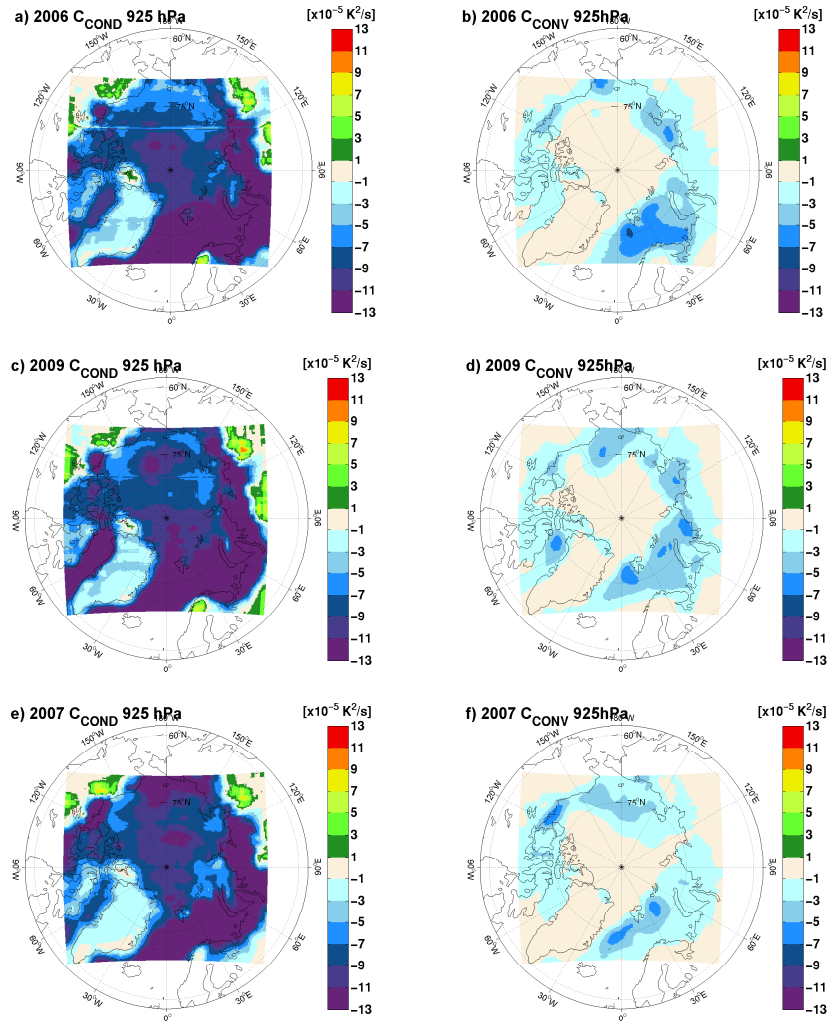


Figure 6.11: Spatial distribution of the temporal averaged separated parts of the contribution C in $10^{-5} K^2/s$ to IV tendency at 925 hPa for the ensembles representing the high ice years 2006 (first row) and 2009 (second row) and the low ice year 2007 (third row). The parts of the term C shown here are the covariances between the fluctuations of potential temperature and temperature tendencies due to condensation (left column) and convection (right column), respectively. The corresponding figures for the low ice year 2012 are shown in Fig. 6.8.

impact on the IV due to the condensative heating. This illustrates that the covariance of the potential temperature fluctuations and the heating rate of condensation tends towards a positive contribution to IV tendency of potential temperature.

The covariance between the potential temperature fluctuation and the temperature tendency due to convection is in general zero over the central Arctic Ocean (Fig. 6.11 for 2006, 2009, 2007 and Fig. 6.8(b) for 2012). However, during the low ice years 2007 and 2012 the negative contribution of the temperature tendency due to convection is larger over the East Siberian/Chukchi Seas compared to the high ice years. Further, it is found that the impact of the C_{CONV} strongly follows the border of sea ice concentration during September (see Fig. 4.2). This includes the polynya in the Beaufort Sea during 2006 and the bight

of open water north of the Chukchi Sea and the corresponding tongue of sea ice in the Beaufort Sea during 2009. For the low ice year 2007 the tongues of sea ice ranging into the Beaufort Sea and into the western part of the Laptev Sea is represented and for 2012 the sea ice peak that occurs a little west of 150° E is visible. This behaviour of C_{CONV} results in a stronger reduction of IV in years with lower sea ice conditions.

A summarising remark of the influence of the sea ice on the potential temperature IV tendency is that in some regions the horizontal 'baroclinic' term B_h contribute weaker to a generation of IV tendency during low ice years compared to high ice years. Whereas, the vertical 'baroclinic' term B_v contributes to a stronger reduction of IV tendency during the low ice years compared to the high ice years. In sum this shows that low ice conditions enhance a negative 'baroclinic' contribution to IV tendency resulting in a stronger reduction of the IV. The same is detected for some of the individual covariances of the diabatic source and sink term C at 925 hPa. The covariance between the fluctuation of potential temperature and temperature tendency due to convection contributes more negatively to IV tendency since it follows strongly the border of the sea ice cover. The analysis of the covariance between the fluctuation of potential temperature and condensation reveals a stronger negative contribution to the IV tendency with enhanced sea ice loss over the Chukchi Sea. However, this is not valid for the low ice years 2012. During 2012 the great Arctic cyclone event and the resulting sea ice retreat lead to an impact of the condensative heating that is comparable to the high ice years with less negative values over the Chukchi Sea. However, concerning the diabatic source and sink term C , the generation of IV tendency is enhanced with decreasing sea ice cover (Fig. 6.6(g) for 2012, Fig. A.7(g) for 2007, Fig. A.7(g) for 2009 and Fig. A.7(g) for 2006). This is caused by the covariance between the potential temperature fluctuations and the radiative heating (for 2012 see Fig. 6.8(c), for 2006, 2007 and 2009 not shown), whose positive contribution over the Arctic Ocean is slightly enhanced during the low ice years (especially during 2007) compared to the high ice years.

It is found that the IV of potential temperature is weaker in low ice years compared to the high ice years in the lower troposphere (see Fig. 5.5(a) and Fig. 5.7(first column)). Obviously, on average this is caused by both 'baroclinic' terms, which contribute less positive (B_h) and more negative (B_v) to the IV tendency of potential temperature. However, the found dependencies between the sea ice cover and the IV and its contributions is only weak and may are not significant. Probably, the non-linear dynamics within the season are averaged out due to the seasonal means (JAS). This leads to the idea to investigate individual time steps to find a more distinct relationship between the IV and its contributions and the sea ice cover and atmospheric conditions (see Chapter 8).

Chapter 7

Comparison of Potential Temperature IV based on HIRHAM5 and CRCM5

Within this chapter, the impact of two different RCMs on the IV and its dynamical and diabatic contributions is investigated. Hence, the results obtained with the HIRHAM5 (see Sec. 5.2 and Chapter 6) are compared to results of the Canadian RCM version 5 (CRCM5). Both models cover the same Arctic domain and are driven with the same LBC and partly the same IC. The comparison is done for the low sea ice year 2012 covering the time period from July to September. The findings explained in the present chapter will be published by Nikiema et al. [2015].

7.1 CRCM Model Description

The CRCM5 is a limited-area model based on the Canadian Global Environment Multiscale model (GEM) [Zadra et al., 2008]. For this work it is applied with a horizontal resolution of 0.25° on a rotated latitude-longitude grid. In the vertical 56 levels are used that are discretised with a hybrid terrain-following hydrostatic-pressure coordinate ($\sigma - p$ -coordinates [Laprise, 1992]). An Arakawa staggered C-grid is applied for the horizontal discretisation. The model runs with a time stepping scheme based on an implicit semi-Lagrangian two-time-level marching scheme described by Côté et al. [1998] with a time step of 12 minutes.

For the comparison of the IV and its dynamical and diabatic contributions between the HIRHAM5 and the CRCM5 over the Arctic for the summer season 2012, both models use the same simulation set-up to generate the ensemble with 20 members (explained in Sec. 2.2) and store the required variables on the same 19 vertical pressure levels. Both models are driven with the same LBC provided by the ERA-Interim data set. However, there are some differences concerning the IC which are used from ERA-Interim to drive

the HIRHAM5, but the CRCM5 is partly forced with data from a simulation run performed with the CRCM5. This is true for the variables land-surface temperature, volumetric water content of soil, sea ice temperature and snow depth. Besides, the sea ice thickness is calculated within the CRCM5 including a parameterisation for the albedo and heat conductivity (Semtner [1976], Ebert and Curry [1993], Flato and Brown [1996]), whereas it is set constant to 2 *m* in HIRHAM5. Additionally, the set-ups of the two RCMs differ in the time discretisation, because the HIRHAM5 runs with a semi-implicit leapfrog time stepping scheme with a time step of 120 seconds, whereas the CRCM uses a time step of 12 minutes with the implicit semi-Lagrangian two-time-level marching scheme. For the investigation both models cover the same Arctic domain, but for the simulations with the CRCM5 the domain is larger due to the ten grid point wide semi-Lagrangian halo additionally to the ten grid-point wide sponge zone that is included in both models. The analysis is done excluding the halo and the sponge zone on the common grid of 188 x 170 grid points for both models.

Concerning the parameterisations the models differ as well. CRCM5 uses the convection scheme that is based on the Kain-Fritsch deep convection [Kain and Fritsch, 1990] and the Kuo-transient scheme for shallow convection [Kuo, 1965] whereas the HIRHAM5 uses the mass flux scheme of Tiedtke [1989] that includes formulations for deep, shallow and mid-level convection. The CRCM5 uses the large-scale condensation scheme from Sundqvist et al. [1989] and HIRHAM5 uses the prognostic statistical cloud scheme developed by Tompkins [2002]. The radiation parameterisation in CRCM5 is performed with the correlated-K radiation scheme [Li and Barker, 2005], whereas HIRHAM5 uses the solar and terrestrial radiation scheme based on Fouquart and Bonnel [1980] and Mlawer et al. [1997], respectively. The vertical diffusion from Benoit et al. [1989] is used in the CRCM5 and the one from Roeckner et al. [2003] in the HIRHAM5. In both RCMs the horizontal diffusion is weak with a fourth-order horizontal diffusion in the CRCM5 and sixth-order horizontal diffusion in the HIRHAM5. The horizontal diffusion is considered within the CRCM5 budget study of potential temperature IV tendency and hence, contributes to the diabatic source and sink term *C*. Within the HIRHAM5 budget study the horizontal diffusion is neglected.

Within the data provided by the CRCM5 the spin-up time of five days is excluded. It has to be mentioned that the spin-up is considered only in Fig. 7.1(b) to illustrate the behaviour of the spin-up. All temporal averages and the temporal evolutions in Fig. 7.3(b) are calculated without this spin-up time and therefore, cover the time period from July 11th to September 30th 2012.

7.2 Results

7.2.1 Comparison of Potential Temperature IV

The vertical profiles of the domain and temporal averaged IV (across-member variance) of the potential temperature for the HIRHAM5 and CRCM5 are shown in Fig. 7.1(a). Both models show the same profiles with high values in the lower troposphere and at 500 *hPa* and in between the IV is weaker. The lowest values are observed at 300 *hPa* and at the surface due to the LBC that are the same for all ensemble members. Compared to the CRCM5 the HIRHAM5 reaches lower values of IV through the whole atmosphere, especially in the lower troposphere. Both RCMs disagree in their absolute maxima. The absolute maximum of IV generated with the HIRHAM5 is found at 500 *hPa* (ca. $7 K^2$), whereas the absolute maximum within the CRCM5 simulations is located at 925 *hPa* ($8.5 K^2$).

The vertical averaged IV of the potential temperature fluctuates in time (Fig. 7.1(b)) and is quite similar in both models. Both time series are correlated with a coefficient of 0.93. In general, the IV of the HIRHAM5 is smaller than the IV of the CRCM5. The differences between the vertical averaged magnitudes is mainly caused by the IV at 925 *hPa* (Fig. 7.1(b)). Nevertheless, the high correlation coefficient of 0.92 between the time series at 925 *hPa* illustrates that the fluctuation between both curves is quite equal. At 300 *hPa* the magnitude of the IV generated with HIRHAM5 and CRCM5 differ less from each other, but reach a slightly weaker correlation coefficient of 0.90.

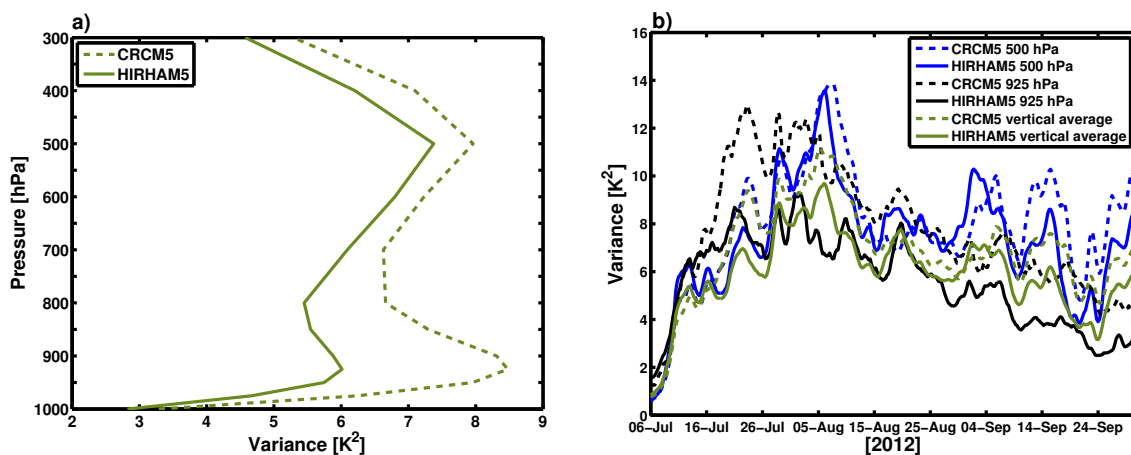


Figure 7.1: Vertical profiles of the temporal and domain averaged across-member variance (IV) in K^2 (a) and the domain averaged temporal evolution at 925 *hPa*, at 500 *hPa* and the vertical averaged across-member variance (IV) in K^2 (b) for the models HIRHAM5 (solid) and CRCM5 (dashed) for the ensemble 2012. The temporal averages in (a) are calculated from 11th July to 30th September (neglecting the spin-up time of 5 days). The green solid line in (a) is comparable to the one shown in Fig. 5.5(a), apart from the neglected spin-up time. The solid lines in (b) are the same as shown in Fig. 5.5(b) and Fig. 5.6(d).

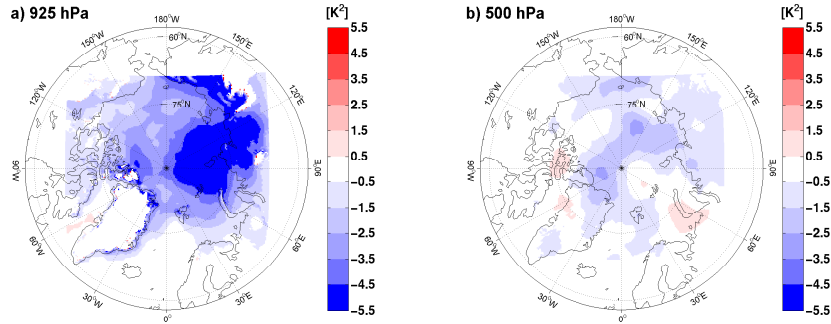


Figure 7.2: Spatial distribution of the difference of the temporal averaged across-member variance (IV) in K^2 between the two RCMs (HIRHAM5 minus CRCM5) at 925 hPa (a) and at 500 hPa (b) for the ensemble 2012. The differences are based on the absolute values of the potential temperature IV simulated with the HIRHAM5 (Fig. 5.7(g), (h)). The temporal averages are calculated from 11th July to 30th September (neglecting the spin-up time of 5 days).

The spatial distributions of the IV generated with the HIRHAM5 simulations during 2012 at 925 hPa and 500 hPa are shown in Fig. 5.7(g) and (h). The patterns of the IV generated within the CRCM5 are quite similar, especially at 500 hPa. Fig. 7.2 represents the corresponding differences of the IV in HIRHAM5 and in CRCM5. It is obvious that HIRHAM5's IV of potential temperature is smaller than CRCM5's IV. As visible in Fig. 7.1(a) and (b) the largest differences of the simulated IV are found at 925 hPa. The strongest IV of the CRCM5 is located at the same regions (north of Greenland towards the Beaufort Sea and from the Laptev Sea to the East Siberian Sea) like identified with the HIRHAM5 (see Fig. 5.7(g)). However, the area of large IV from the Laptev Sea to the East Siberian Sea is extended in CRCM5 and covers more adjacent ocean and Siberian land and reaches almost the Chukchi Sea. Hence, the difference between the models is strongly negative over Siberia and the Siberian coast reaching far into the Arctic Ocean. At 500 hPa (Fig. 7.2(b)) and the vertical averaged (not shown) differences of IV between the CRCM5 and HIRHAM5 are small ($< -3.5 K^2$).

The largest differences between both RCMs occur near the surface leading to the conclusion that the different parameterisations in the boundary layer, the sea ice and land-surface schemes are responsible for this result [Nikiema et al., 2015].

7.2.2 Comparison of the Contributions to IV Tendency

Applying the diagnostic budget equation for the IV tendency of the potential temperature (Eq. 3.34) leads to the seven dynamical and diabatic contributions to the IV tendency. Other than in Chapter 6, the horizontal and vertical third-order terms (E_h and E_v) are not considered separately but are summarised in term E . All terms are shown domain and temporally averaged in Fig. 7.3(a) and domain and vertically averaged in Fig. 7.3(b) for

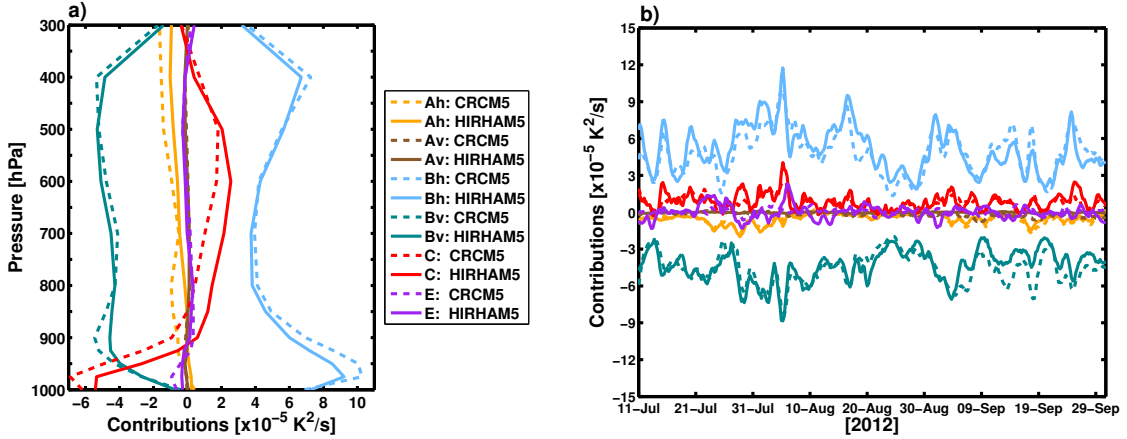


Figure 7.3: Vertical profiles of the temporal and domain averaged seven contributions (a) and temporal evolution of the domain and vertical averaged seven contributions (b) in $10^{-5} K^2/s$ to IV tendency for the models HIRHAM5 (solid) and CRCM5 (dashed) for the ensemble 2012. The temporal averages in (a) are calculated from 11th July to 30th September (neglecting the spin-up time of 5 days).

the HIRHAM5 and CRCM5.

The vertical profiles illustrate that both, the vertical structure and the magnitude of each contribution is quite similar for both RCMs. CRCM5 deviates strongest (ca. $1 \times 10^{-5} K^2/s$) from HIRHAM5 concerning the diabatic source and sink term C . Compared to the CRCM5 the HIRHAM5's C contributes to a weaker reduction of IV near the surface and to a stronger generation of IV between 900 hPa and 500 hPa. This is caused by the horizontal diffusion that is neglected in the HIRHAM5's IV budget and is considered in the CRCM5. HIRHAM5 uses a sixth-order horizontal diffusion that contributes with ca. $-0.3 \times 10^{-5} K^2/s$ to the IV tendency in the lower levels and converge to zero with increasing height.

The temporal evolution of the contributions to the IV tendency of potential temperature reveals that both RCM time series are highly correlated concerning the individual terms. This is not unexpected, because of the strong correlation between both IV time series that is clearly shown in Fig. 7.1(b). The largest correlation is found for the terms A_h , B_h , C and B_v with coefficients of 0.88, 0.83, 0.78 and 0.75. A_v and E are weakly correlated. However, their impact on the IV tendency is small anyway and hence, they will not be considered further in this chapter.

The spatial distributions of the horizontal transport term A_h and both 'baroclinic' terms B_h and B_v obtained with the CRCM5 are very similar concerning the signs and location of maxima to those found for the HIRHAM5 (see Fig. 6.6(a), (c) and (d)). Hence, the differences (Fig. 7.4(a), (b) and (c)) are small between both models. For A_h negative differences (Fig. 7.4(a)) are found in regions with a positive contribution to IV tendency of potential temperature and positive differences coincides with regions of negative contribution in

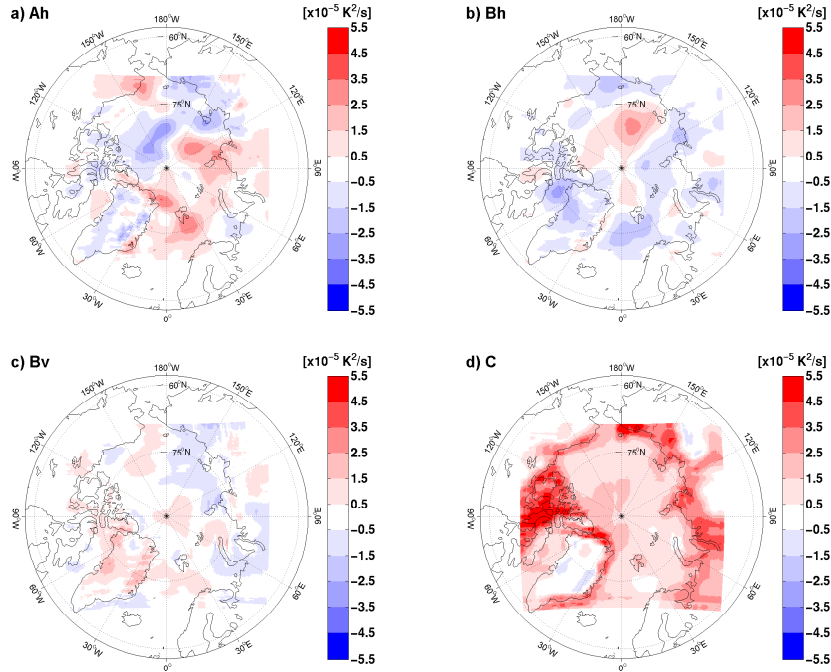


Figure 7.4: Spatial distribution of the difference of the temporal and vertical averaged contributions A_h (a), B_h (b), B_v (c) and C (d) in $\times 10^{-5} K^2/s$ to IV tendency between the two RCMs (HIRHAM5 minus CRCM5) for the ensemble 2012. The differences are based on the absolute values of the contributions simulated with the HIRHAM5 (Fig. 6.6(a), (c), (d) and (g)). The temporal averages are calculated from 11th July to 30th September (neglecting the spin-up time of 5 days).

both models. This means that a weaker generation of IV and a weaker reduction of IV is simulated with HIRHAM5 compared to CRCM5. These results illustrate more pronounced amplitudes between positive and negative contribution to IV tendency due to CRCM5's A_h . Fig. 7.4(b) represents the differences for the term B_h between both RCMs. B_h contributes overall positively to IV tendency which is mostly slightly less distinct for the HIRHAM5 simulations compared to the CRCM5 simulations, illustrated by the negative differences. In contrast, over an area ranging from the East Siberian Sea into the central Arctic Ocean, the difference indicates that the B_h from the HIRHAM5 exceeds the one from the CRCM5. The differences between both models are smaller for the vertical 'baroclinic' term B_v (Fig. 7.4(c)) compared to horizontal 'baroclinic' term B_h and especially compared to A_h . Positive differences illustrate that HIRHAM5's B_v delivers a weaker contribution to a reduction of IV than CRCM5's B_v . This is found for example over the Chukchi Sea, the Pole and from the Queen Elizabeth Islands over Greenland to the Norwegian Sea. In western Russia and north of the Laptev Sea towards the East Siberian Sea the differences indicate a stronger negative contribution of B_v from HIRHAM5 compared to CRCM5.

The domain and vertical averaged temporal evolution of the diabatic source and sink term C (Fig. 7.3(b)) reveals that both models reach mostly the same magnitude or the HIRHAM5 exceeds the CRCM5. The investigation of the spatial distribution has revealed

that the contribution of C to IV tendency of potential temperature is mainly positive in the HIRHAM5 (see Fig. 6.6(g)). The C in CRCM5 contributes to a generation of IV over the Arctic Ocean, small areas in Siberia and in Alaska, but reaches mostly small values ($< 0.7 \times 10^{-5} K^2/s$). In other areas the term C contributes to an intense reduction of IV (with values $< 1.3 \times 10^{-5} K^2/s$) in CRCM5. Hence, C exhibits positive differences (Fig. 7.4(d)). The differing parameterisations lead to a different spatial pattern of the separated parts belonging to C (temperature tendencies due to convection, condensation, radiation and vertical diffusion). For example, the covariance considering the radiative heating reach high values from the Greenland Sea over Barents Sea to Kara Sea in HIRHAM5 (see Fig. 6.8(c)), whereas the spatial pattern is more homogeneous and the belt of high positive contribution (from Norwegian Sea to Kara Sea) is missing for the radiative heating in CRCM5 [Nikiema et al., 2015]. Besides, the less intense negative impact of the condensative heating on the diabatic term C from the Chukchi Sea towards the Arctic Ocean (see Fig. 6.8(a)) is less pronounced in magnitude and horizontal range within the ensemble 2012 performed with the CRCM5 [Nikiema et al., 2015]. The temperature tendency due to the vertical diffusion in the lower troposphere has an intense positive contribution to the term C within the HIRHAM5 (see Fig. 6.2) and only a weak positive contribution within the CRCM5 [Nikiema et al., 2015]. However, this different behaviour of the individual parts of the term C seems to be compensated in the domain average resulting in the same vertical structure of C comparing both models (Fig. 7.3(a)). Only a systematic difference tending to a weaker reduction (below 900 hPa) and a stronger generation (above 900 hPa) of IV is found in HIRHAM5, compared to CRCM5. This difference is explained above and results also from the neglected horizontal diffusion in HIRHAM5.

In general it has to be emphasised that all results concerning the IV of potential temperature and its diabatic and dynamical contributions are very similar in vertical structure, temporal evolution and spatial distribution for the two applied RCMs. Hence, the investigation reveals that the influence of the physics in the RCMs on the IV and its contribution is weak. For both RCMs the same contributions (A_h , B_h , B_v and C) are detected to be important, and have the same behaviour of generating or reducing the IV. These results illustrate that the IV and its contributions are generated by the described physical processes and the natural non-linear behaviour of the atmosphere that is associated with the integration area and does not depend on the chosen model parameterisations.

Chapter 8

Case Studies of the Processes of Potential Temperature IV

Until now the focus was on investigating the IV of potential temperature and its contributions on the seasonal (JAS) time scale for each of the four ensembles. Hence, seasonal averaged spatial distributions and vertical profiles were calculated. The temporal behaviour of the potential temperature IV and the corresponding contribution terms were analysed and Fig. 5.5(b) and Fig. 5.6 illustrated that the IV fluctuates strongly in time with periods of low and high IV. In this present chapter a much shorter time scale, namely individual time steps, are examined to get a more detailed insight in the atmospheric processes generating IV. Therefore, 13 time steps of particular high IV events have been selected within the four ensembles. These events are marked in Fig. 5.6 and listed in Table 8.1. The values in Tab. 8.1 are vertically and spatially averaged. During 2006 three events are selected and concerning the vertical and domain averaged IV of potential temperature these are the strongest events during all years. The horizontal and vertical 'baroclinic' terms B_h and B_v are always the strongest contributors to the IV tendency of potential temperature, especially on 5th September 2006 ($B_h = 15.15 \times 10^{-5} K^2/s$ and $B_v = -9.64 \times 10^{-5} K^2/s$) followed by 5th August 2012 ($B_h = 11.76 \times 10^{-5} K^2/s$ and $B_v = -8.85 \times 10^{-5} K^2/s$). Both time steps and the 15th September 2007 are characterised by high values of the sum of all contributions (last row), because the intense contribution of B_h is not fully compensated by the other terms. In general the other terms are quite weak on vertical and domain average, apart from the diabatic source and sink term C . The intensity of the contribution of C strongly depends on the time and reaches quite high values on 5th September 2006, 9th September 2009, 20th August 2007 and on 23rd July 2006.

Four events (one for each ensemble) are discussed in detail (shaded grey in Tab. 8.1), because they illustrate and explain the relation between the specific atmospheric conditions and the IV. The spatial distribution of IV is shown for the vertical level where the maximum

Table 8.1 : Vertical and domain averaged potential temperature across-member variance (IV in K^2), the seven contributions in $\times 10^{-5} K^2/s$ to IV tendency and the sum of all contributions (last row) for the analysed 13 high IV events within the four ensembles 2006, 2007, 2009 and 2012. The four grey shaded columns indicate the high IV events that are examined in detail in this study (Chapter 8).

	2006			2007			2009			2012			
	23-07 00UTC	05-09 06UTC	22-09 18UTC	25-07 00UTC	20-08 06UTC	15-09 18UTC	23-07 00UTC	16-08 00UTC	06-09 06UTC	21-09 12UTC	05-08 06UTC	02-09 18UTC	15-09 12UTC
IV	10.04	11.01	10.75	6.75	8.32	7.53	8.59	7.68	7.81	7.35	9.48	6.90	6.20
Ah	-1.18	0.46	-0.24	-0.24	-0.45	-0.57	-0.74	-0.85	-0.12	-0.72	-1.16	-0.43	-0.23
Av	-0.09	-0.08	-0.04	-0.03	-0.02	-0.05	-0.02	-0.05	-0.10	-0.03	-0.05	0.02	-0.04
Bh	9.45	15.15	5.80	3.02	5.87	7.46	3.24	6.84	5.16	4.27	11.76	5.89	4.60
Bv	-6.35	-9.64	-4.23	-3.16	-5.64	-4.44	-3.12	-4.53	-6.63	-4.71	-8.85	-5.75	-3.21
Eh	-1.36	1.00	0.55	-0.20	1.38	1.55	0.09	-0.55	-0.52	0.79	0.81	-0.20	-0.42
Ev	-0.02	0.15	0.10	0.03	0.07	0.01	0.13	0.09	0.15	0.08	-0.03	0.06	0.10
C	1.15	2.46	-0.73	0.76	1.34	0.64	-0.56	0.03	1.35	1.01	0.40	0.84	-0.01
sum of all terms	1.60	9.50	1.21	0.18	2.55	4.60	-0.98	0.98	-0.71	0.69	2.88	0.43	0.79

IV is achieved during this particular time step. Only the most important contributions to IV tendency of potential temperature in the corresponding level are presented. For the interpretation of the results some atmospheric variables (such as temperature, mslp and geopotential) are shown as well.

8.1 Case: 23rd July 2006 00 UTC

The first maximum IV event in 2006 is simulated on July 23rd at 00 UTC at 925 *hPa* (Fig. 5.6(a)). At 500 *hPa* and at 300 *hPa* the peaks are shifted in time and reach their maximum before the selected time step. Fig. 8.1(a) represents the spatial distribution of IV in 925 *hPa*. It is obvious that the maximum IV is found in the eastern part of the model domain, especially in the region covering the Barents Sea, Kara Sea and northern Siberia with values exceeding $30 K^2$. However, the centre with high IV extends into the Arctic Ocean with values of up to $20 K^2$. The region of high IV compounds from two centres of high IV that are located over central Siberia and a large area covering the Barents and Kara Seas. Both developed two days before the maximum IV event. Through the vertical, the intensity of the centre of maximum IV decreases at 850 *hPa* and especially at 700 *hPa*, but increases again at 500 *hPa*. Additionally, a smaller and weaker centre of IV is found over the Canadian coast. This is more pronounced during the day before and after the maximum IV event.

The location of the maximum IV of potential temperature coincides with an area of quite high across-member standard deviation for the geopotential height at 925 *hPa* ($> 60 gpm$, Fig. 8.2(a)) and at 500 *hPa* ($> 110 gpm$, Fig. 8.2(b)) calculated for this time step. However, the deviation between the individual ensemble members is strongest over the central Arctic Ocean between $120^\circ E$ and $180^\circ E$. This region coincides with the IV reaching up to $20 K^2$. The pronounced gradient of the across-member standard deviation along the Eurasian coast at 500 *hPa* induces the intensification of the IV at 500 *hPa* mentioned before.

The centre of high IV tendency is mainly generated by the horizontal 'baroclinic' term B_h (Fig. 8.1(c)). B_h is mostly positive during this time step with one centre coinciding with the centre of maximum IV. The main reduction of IV tendency is due to the horizontal transport term A_h (Fig. 8.1(b)). Large negative values of up to $-24 \times 10^{-5} K^2/s$ occur over the area of maximum IV. Negative A_h describes a transport of IV out of this area. It seems, that the IV is moved in accordance with the pressure pattern (Fig. 8.2(a)) from Barents and Kara Sea and northern Siberia (negative contribution to IV tendency) westward to Scandinavia (positive contribution to IV tendency).

The other terms (not shown) contribute only weak or in a heterogeneous way to the IV tendency of potential temperature, apart from B_v that reaches partly strong negative values

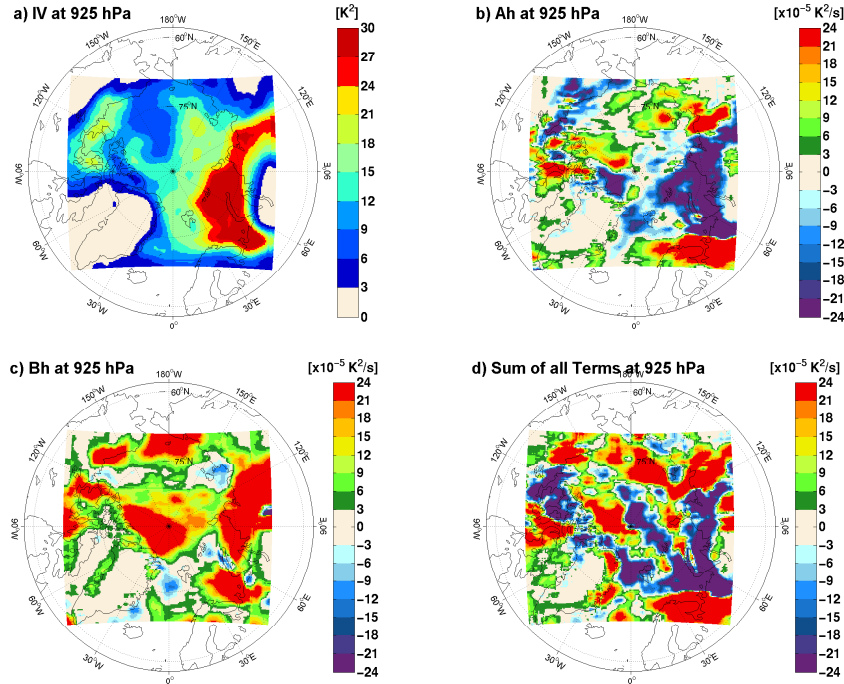


Figure 8.1: Spatial distribution of the potential temperature across-member variance (IV) in K^2 (a) and the contributions A_h (b) and B_h (c) in $10^{-5}K^2/s$ to IV tendency and the sum of all seven contributions in $10^{-5}K^2/s$ (d) for 23rd July 2006 at 00 UTC at 925 hPa.

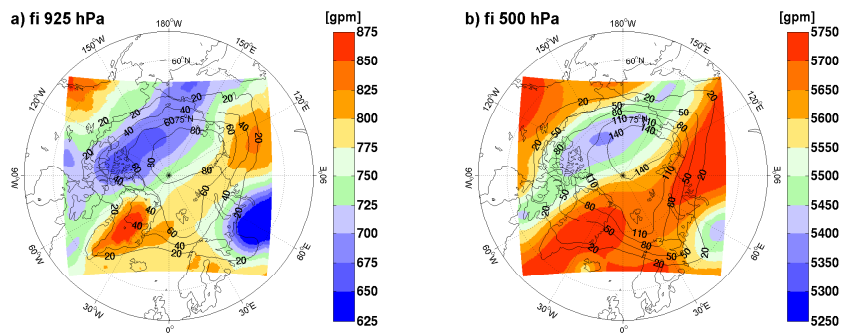


Figure 8.2: Spatial distribution of the simulated ensemble mean geopotential height in gpm at 925 hPa (a) and at 500 hPa (b) for 23rd July 2006 at 00 UTC. The contour lines illustrate the HIRHAM5 cross-member standard deviation of the corresponding variables during this time step.

over the area coinciding with maximum IV. Hence, the sum of all contributions (Fig. 8.1(d)) illustrates that the region of maximum IV is mainly determined by a negative contribution representing a reduction of IV. This is caused by the fact, that the centre of maximum IV has already started to dissipate compared to the previous time steps. Nevertheless, the maximum IV event occurs not during the previous time steps, because the area covering the eastern Arctic Ocean reaches lower values as achieved on 23rd July at 00 UTC (values of up to $18 K^2$).

8.2 Case: 15th September 2007 18 UTC

The domain averaged temporal evolution of the IV in different levels during 2007 (see Fig. 5.6(b)) reveals, that on 15th September 2007 at 18 UTC the maximum IV is found at 500 *hPa* with values of approximately $10 K^2$. The spatial distribution of the IV of potential temperature during this time step is shown for 500 *hPa* (Fig. 8.3(a)) and is characterised by an area of high values in the western model domain, especially over the Queen Elizabeth Islands. The centre is formed by a small centre ranging from the Beaufort Sea into the Arctic Ocean that expands eastward during the two days before the maximum IV event and reaches to the northwestern part of Greenland.

The atmospheric circulation is characterised by high pressure at the surface (see Fig. 8.4(a)) and with increasing height low pressure conditions are formed (Figs. 8.4(b)). Hence, the across-member standard deviation for both pressure variables illustrate varying realisations between the ensemble members over the Queen Elizabeth Islands and at the Siberian coast. The centre of high across-member standard deviation at the Siberian coast weakens with increasing height and the centre over the Queen Elizabeth Islands intensifies with increasing height. This centre of maximum across-member standard deviation (up to 140 *gpm* at 500 *hPa*) in the western Arctic Ocean coincides with the maximum IV of potential temperature at 500 *hPa*. This is contrary to the case on 23rd July 2006 when the IV of potential temperature indeed coincides with high across-member variance, but not with the region of absolute maximum. Further, the region of high IV is characterised by low temperature (up to $-12^\circ C$) near the surface compared to the surroundings. Additionally, the across-member standard deviation of the temperature reaches as well high values at the Queen Elizabeth Islands.

In more physical terms the IV tendency in this area is generated and reduced by the horizontal transport term A_h (Fig. 8.3(b)) and both 'baroclinic' terms B_h (Fig. 8.3(c)) and B_v (Fig. 8.3(d)). The IV is moved from Alaska (negative A_h contribution) eastward to the Beaufort Sea (positive A_h contribution) and further, from the North of Greenland and the Queen Elizabeth Islands (negative A_h contribution) eastward to Greenland Sea (positive A_h contribution). The location of the maximum gradient of A_h at $90^\circ W$ coincides with the area of maximum IV. The border of positive and negative values of the 'baroclinic' contributions ranges from the East to the West with the generating contribution of B_h located north of its reducing influence. For the B_v it is the other way around. Unlike the case that occurs on 23rd July 2006 (see Sec. 8.1) both 'baroclinic' terms reach positive and negative values that are well defined from each other with a border that crosses the region of maximum IV.

Interesting is the diabatic source and sink term C (Fig. 8.3(e)). C contributes to a generation

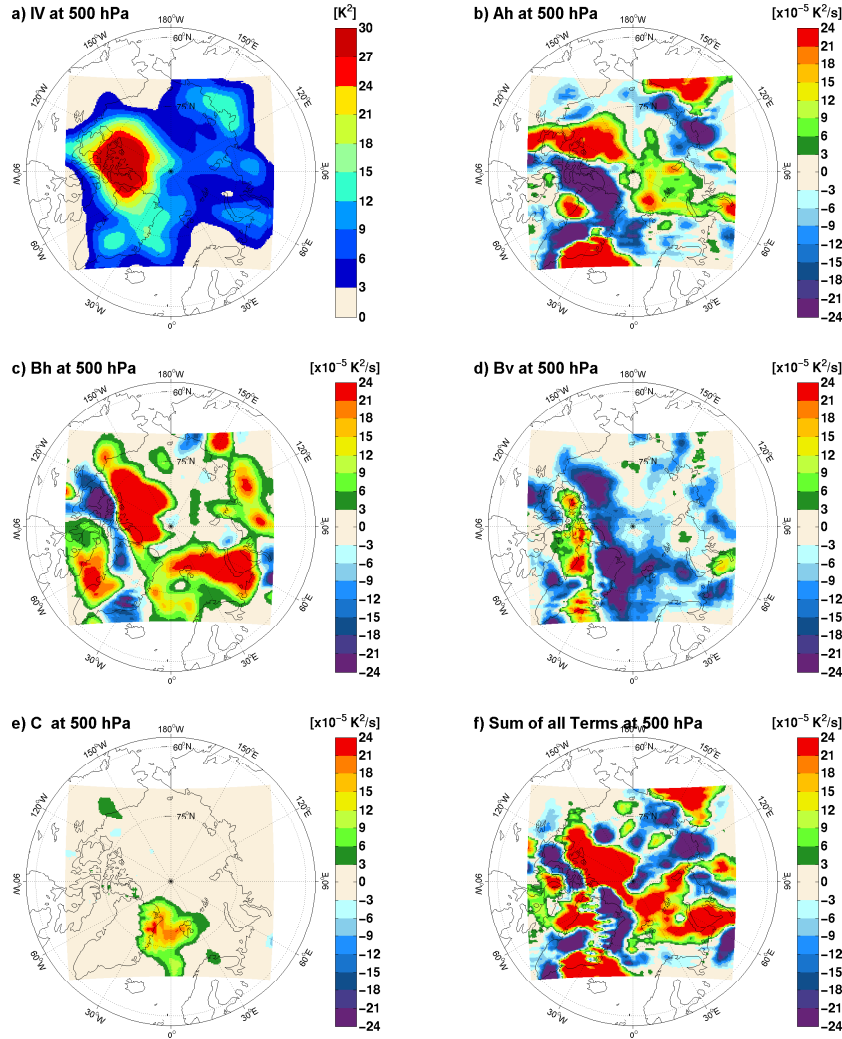


Figure 8.3: Spatial distribution of the potential temperature across-member variance (IV) in K^2 (a) and the contributions A_h (b), B_h (c), B_v (d) and C (e) in $10^{-5}K^2/s$ to IV tendency and the sum of all seven contributions in $10^{-5}K^2/s$ (f) for 15th September 2007 at 18 UTC at 500 hPa.

of IV tendency with values of up to $20 \times 10^{-5}K^2/s$ east of Greenland, but contributes not to the IV tendency in the area of maximum IV. However, Fig. 8.3(a) reveals, that the IV reaches values of approximately $12 K^2$ east of Greenland, coinciding with the generation due to the diabatic contribution.

The sum of all terms (Fig. 8.3(f)) illustrate a positive contribution to IV tendency over the ocean part and the northern Queen Elizabeth Islands of the maximum IV area and negative contribution to the southern part.

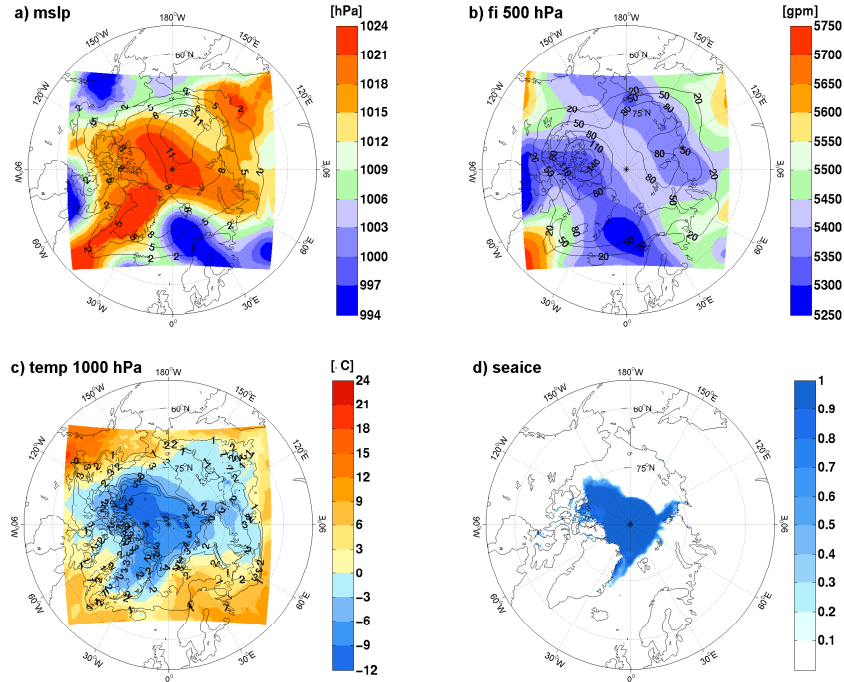


Figure 8.4: Spatial distribution of the simulated ensemble mean mslp in hPa (a), geopotential height at $500 hPa$ in gpm (b), the temperature at $1000 hPa$ in $^{\circ}C$ (c) and the sea ice concentration provided by ERA-Interim (d) for 15th September 2007 at 18 UTC. The contour lines in (a), (b) and (c) illustrate the HIRHAM5 across-member standard deviation of the corresponding variables during this time step.

8.3 Case: 16th August 2009 00 UTC

The domain averaged temporal evolution of IV during 2009 (Fig. 5.6(c)) illustrates that the peak of high potential temperature IV on 16th August 2009 at 00 UTC is found at $925 hPa$ (approximately $10 K^2$ at). And, the IV at $500 hPa$ is of similar order of magnitude and the same is valid for the other levels (not shown) apart from $300 hPa$. This event is interesting, because the spatial distribution of IV reveals, that the area of high IV shifts between the vertical levels (Fig. 8.5(a) for $925 hPa$ and Fig. 8.7(a) for $500 hPa$).

At $925 hPa$, high IV is simulated along the coastlines with values up to $20 K^2$ and with an absolute maximum in the East Siberian Sea (ca. $30 K^2$). This region is characterised by relatively high pressure conditions (Fig. 8.6(a), (b)). The across-member standard deviation of the geopotential height at $925 hPa$ shows a strong gradient over the region of maximum IV of potential temperature at $925 hPa$. However the largest across-member standard deviation is simulated mainly over the western central Arctic Ocean, coinciding with the region of maximum potential temperature IV that is found at $500 hPa$. The same pattern is seen in the $500 hPa$ geopotential height across-member standard deviation.

Concerning the contributions to IV tendency of potential temperature, the spatial distribution of the horizontal 'baroclinic' term B_h (Fig. 8.5(c)) is in agreement with the

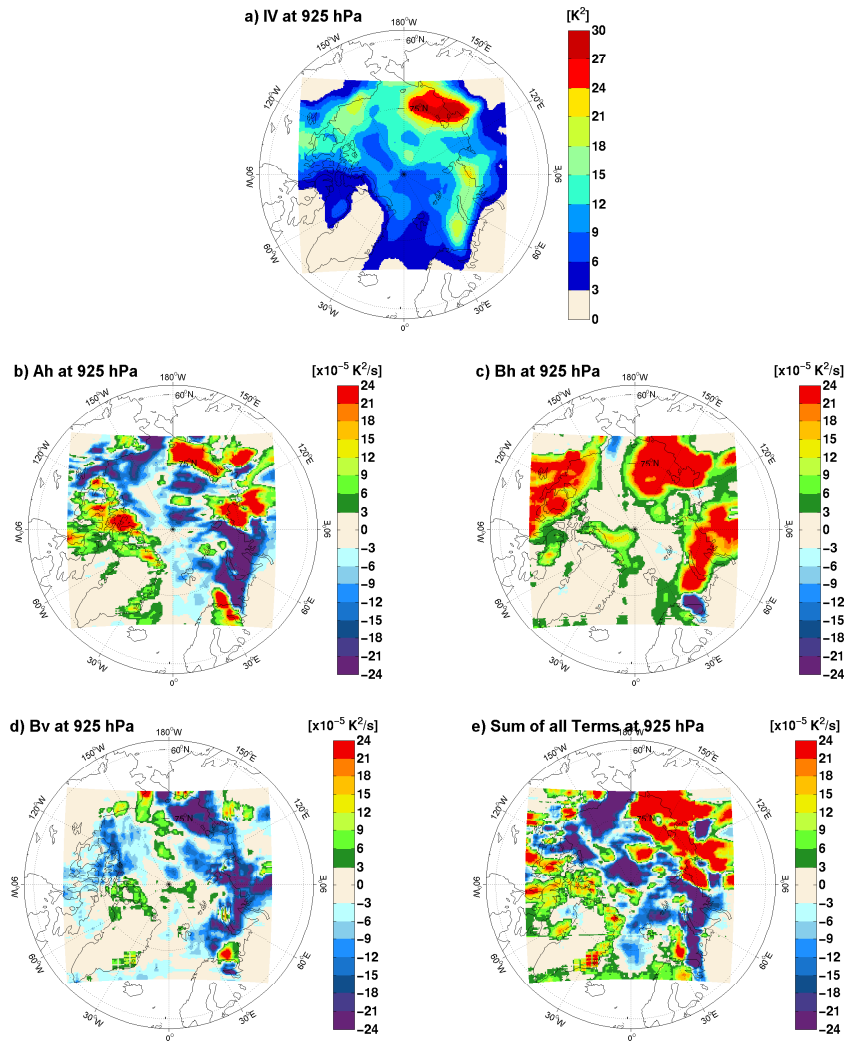


Figure 8.5: Spatial distribution of the across-member variance (IV) in K^2 (a) and the contributions A_h (b), B_h (c) and B_v (d) in $10^{-5} K^2/s$ to IV tendency and the sum of all seven contributions in $10^{-5} K^2/s$ (e) for 16th August 2009 at 00 UTC at 925 hPa.

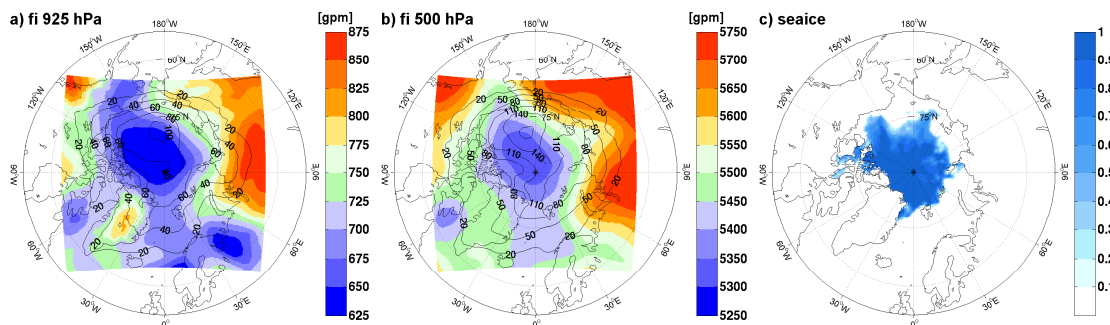


Figure 8.6: Spatial distribution of the simulated ensemble mean geopotential height in gpm at 925 hPa (a), at 500 hPa (b) and the sea ice concentration provided by ERA-Interim (c) for 16th August 2009 at 00 UTC. The contour lines in (a) and (b) illustrate the HIRHAM5 across-member standard deviation of the corresponding variables during this time step.

8.3. CASE: 16TH AUGUST 2009 00 UTC

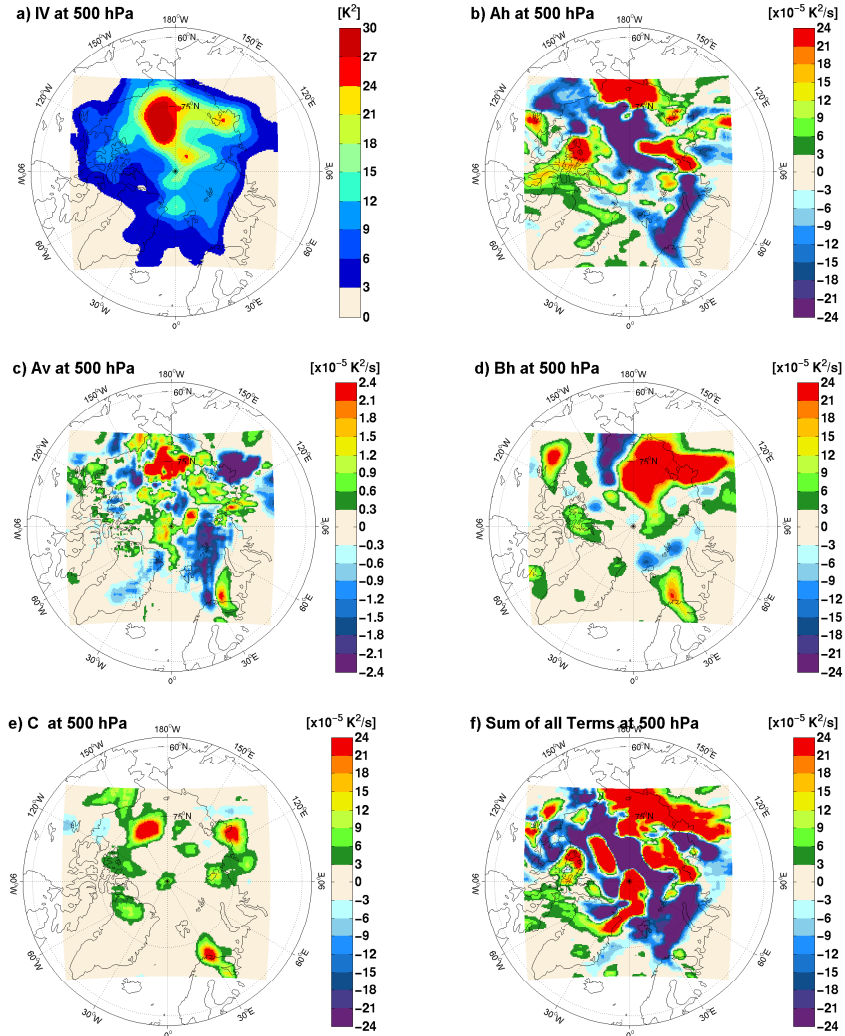


Figure 8.7: Spatial distribution of the across-member variance (IV) in K^2 (a) and the contributions A_h (b), A_v (c), B_h (d) and C (e) in $10^{-5} K^2/s$ to IV tendency and the sum of all seven contributions in $10^{-5} K^2/s$ (f) for 16th August 2009 at 00 UTC at 500 hPa.

corresponding region of high IV. High values of B_h occur along the coastlines. A reduction of the IV tendency along the Eurasian coast is induced by the vertical 'baroclinic' term B_v (Fig. 8.5(d)). A_h (Fig. 8.5(b)) contributes to a generation of the IV tendency at the area of maximum IV, due to the fact that IV is transported southward from the central Arctic Ocean north of the East Siberian Sea (negative contribution due to A_h) to the East Siberian Sea (positive contribution due to A_h). However, IV is as well moved from the Barents and Kara Sea eastward to the Laptev Sea, leading to a centre of weaker IV ($18 K^2$) at the Eurasian coast (Fig. 8.5(a)). Hence, the sum of all terms (Fig. 8.5(e)) indicates a negative contribution to IV tendency in this area, whereas the East Siberian Sea and the northeastern part of Siberia are characterised by a positive contribution to IV tendency. At 500 hPa the centre of high IV (Fig. 8.7(a)) is shifted towards the Chukchi Sea. The main

generation of IV at this level is due to the diabatic source and sink term C (Fig. 8.7(e)) that covers the sea ice border and the bight of the ice-free area north of the Chukchi Sea (Fig. 8.6(c)). Additionally, the vertical transport term A_v (Fig. 8.7(c)) contributes positively to the IV tendency of potential temperature at the same area as C , but with a magnitude that is 100 times smaller. This positive contribution illustrates that the IV is transported from another level into the 500 hPa level. Below 500 hPa the term A_v contributes negatively to the IV tendency in this region indicating a transport of IV towards upper levels. A_h (Fig. 8.7(b)) contributes negatively and positively to the maximum IV at 500 hPa , because IV is moved from the central Arctic Ocean towards the Chukchi Sea with the strongest gradient covering the region of maximum IV. The horizontal 'baroclinic' term B_h (Fig. 8.7(d)) contributes to a generation and a reduction of IV over the area of maximum IV. However, the region of positive contribution ranges towards the East Siberian Sea and Siberia coinciding with values of up to $18 K^2$ (Fig. 8.7(a)). There the positive contribution to IV tendency of potential temperature is weakened by the vertical 'baroclinic' term B_v (not shown). The sum of all terms (Fig. 8.7(f)) reveals a positive contribution to the IV tendency, whereas the region of maximum IV is influenced by a positive and a negative contribution due to the sum of all terms.

8.4 Case: 5th August 2012 06 UTC

The 5th August 2012 at 06 UTC is chosen, because this is the maximum IV event of potential temperature generated within the ensemble 2012 (see Tab. 8.1 and Fig. 5.6(d)) and coincides with the occurrence of the great Arctic cyclone event during the beginning of August 2012. The results are shown at 500 hPa , which is the level of highest IV. The spatial distribution highlights the locations of strong IV (Fig. 8.8(a)). Values of IV higher than $30 K^2$ occur over two centres. The first centre ranges from the Laptev Sea to the Beaufort Sea covering the Arctic Ocean. This is the more intense centre and reaches down to the surface (not shown). The second centre is located over the north of Greenland and Greenland Sea.

During the two days prior this maximum event, the two centres start to form due to several small centres of high IV, where the centre over Greenland grows faster, despite being the smaller one. After the maximum event both centres dissipate again into several small regions of enhanced IV (not shown).

Concerning the results, the most relevant contributions are both 'baroclinic' terms, B_h and B_v (Tab. 8.1, Fig. 8.8(b), (c)). Both vertical and domain averaged contributions reach values of up to $11.76 \times 10^{-5} K^2/s$ (B_h) and $-8.85 \times 10^{-5} K^2/s$ (B_v). The diabatic source and sink term C has also important regional influence on the IV tendency during this maximum

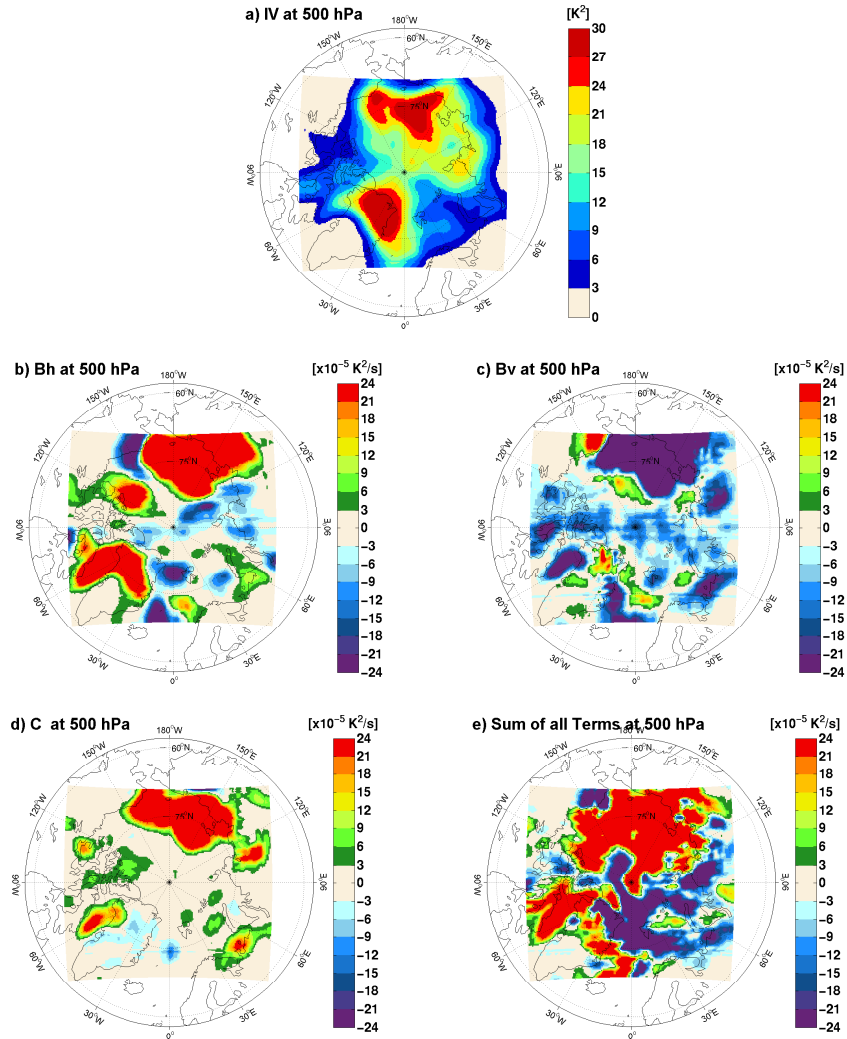


Figure 8.8: Spatial distribution of the across-member variance (IV) in K^2 (a), and the contributions B_h (b), B_v (c) and C (d) in $10^{-5} K^2/s$ to IV tendency and the sum of all seven contributions in $10^{-5} K^2/s$ (e) for 5th August 2012 at 06 UTC at 500 hPa.

potential temperature IV event. C has absolute values comparable to B_h and B_v and is therefore shown as well (Fig. 8.8(d)). The other terms have a negligible contribution to IV tendency with A_h , A_v and E_v reducing and E_h generating IV in domain and vertical average (see Tab. 8.1). The clear centres of strong positive contributions to IV tendencies of potential temperature are caused due to B_h and C which both reach values $> 25 \times 10^{-5} K^2/s$ over the East Siberian Sea and Chukchi Sea which are compensated only by B_v (values $< -25 \times 10^{-5} K^2/s$). This centre of strong impact on the IV tendency due to the 'baroclinic' terms coincides with the region of low pressure ranging from the Chukchi Sea to East Siberian Sea into the central Arctic Ocean at 500 hPa geopotential height (Fig. 8.9(b)) and that expands towards Northern America and the Siberian land at the surface (mslp in Fig. 8.9(a)). Interestingly, the EGR during this time step (Fig. 8.9(c)) reveals a region of high

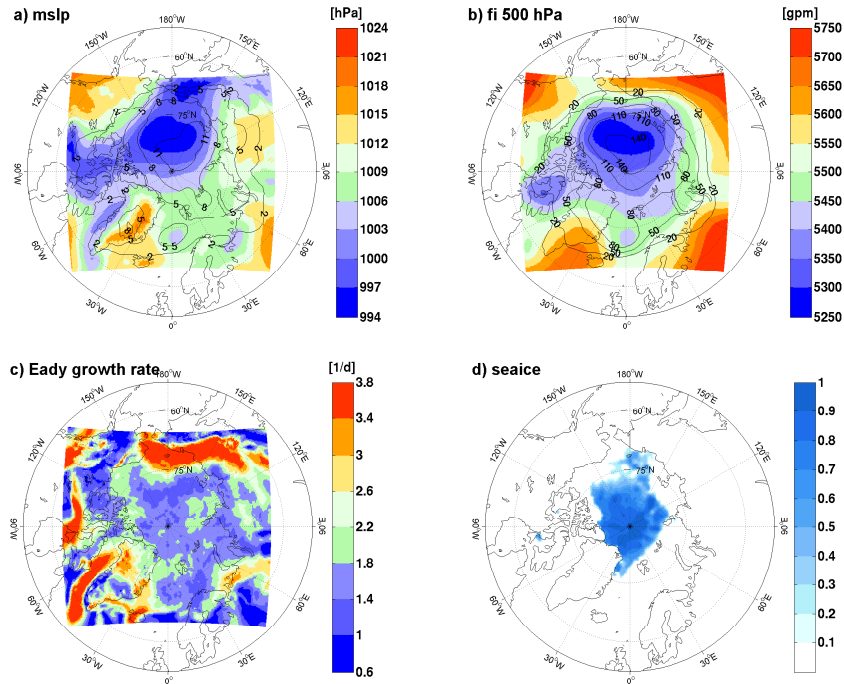


Figure 8.9: Spatial distribution of the simulated ensemble mean mslp in hPa (a), geopotential height at 500 hPa in gpm (b), the Eady growth rate between 850 hPa and 500 hPa in $1/d$ (c) and the sea ice concentration provided by ERA-Interim (d) for 5th August 2012 at 06 UTC. The contour lines in (a) and (b) illustrate the HIRHAM5 across-member standard deviation of the corresponding variables during this time step.

potential for baroclinic instability ranging from central Siberia over the East Siberian Sea to the Chukchi Sea. This result is associated with the great Arctic cyclone event in the beginning of August 2012 and further confirms the strong contribution of the 'baroclinic' terms to potential temperature IV tendency. Simmonds and Rudeva [2012], Zhang et al. [2013] and Parkinson and Comiso [2013] investigated this cyclone and identified its origin over Siberia on 2nd August and its maximum appearance on 4th August with a central pressure of 966 hPa over the East Siberian Sea, as also indicated by the simulated mslp (Fig. 8.9(a)). This cyclone leads to a strong sea ice retreat in this area (Zhang et al. [2013] and Parkinson and Comiso [2013] and seen in Fig. 8.9(d) for the ERA-Interim sea ice concentration) resulting in changed vertical fluxes of moisture and heat between the ocean and the atmosphere influencing turbulence and diabatic processes, explaining the positive contribution of the term C over this specific region.

The sum of all terms (Fig. 8.8(e)) partly reflects the pattern of the IV (Fig. 8.8(a)) and the horizontal 'baroclinic' term (B_h (Fig. 8.8(b))). The average over the domain reveals a strong generation of potential temperature IV tendency due to all seven contributions.

Chapter 9

Conclusion and Outlook

9.1 Summary and Discussion

Within this work the atmospheric RCM HIRHAM5 is applied over the Arctic domain to investigate the model generated internal variability (IV). IV means that RCMs provide different solutions for simulations that differ in their IC only. Therefore, four ensembles are arranged and each consists of 20 members that differ in their IC, but use the same LBC. The ensembles are performed for the years 2006 and 2009 representing high ice years and 2007 and 2012 representing low ice years. All four ensembles cover the time period from July to September, the season of intense sea ice melting. The across-member standard deviation for the atmospheric circulation and the across-member variance for the potential temperature are analysed as a measure for the IV. The model runs with a horizontal resolution of approximately 25 km and 40 vertical levels. Any nudging is turned off for this analysis to ensure a free evolution of each simulation resulting in a distinct development of HIRHAM5's IV.

9.1.1 Arctic IV and the Contributions to IV Tendency

Until now, this is the first study that analyses the budget of IV tendency of potential temperature in an Arctic RCM, namely the HIRHAM5, and identifies the dynamical and diabatic contributions to the IV tendency. Further, this is the first study that quantifies the IV generated within the HIRHAM5. Rinke and Dethloff [2000] and Rinke et al. [2004] determined the IV of the former model version HIRHAM4 and found smaller across-member standard deviation in the Arctic atmospheric circulation compared to the HIRHAM5. But, they used a much smaller ensemble with four members only, covering the year 1990. In agreement with current results they detected a more intense IV compared to studies investigating the mid-latitudes. This is due to the specific atmospheric situations

with the characteristic circum-polar vortex in the Arctic that keeps perturbations longer in the model domain. Whereas, von Storch [2005] define the mid-latitudes as well-flushed regions generating a weaker IV in RCMs. This finding is supported by this present study and by Sommerfeld et al. [2015] for the IV of the potential temperature compared to the studies of Nikiema and Laprise [2010] and Nikiema and Laprise [2011]. They investigated a region covering northeastern part of Northern America and parts of the Atlantic Ocean. The IV in the Arctic exceeds the IV of Northern American region by an order of ten to 100 considering the across-member variance of potential temperature. HIRHAM5's IV over the Arctic fluctuates strongly in time related to the synoptic situation. This result is consistent with previous studies (Giorgi and Bi [2000], Christensen et al. [2001], Caya and Biner [2004], Rinke et al. [2004], Alexandru et al. [2007], Nikiema and Laprise [2010], Nikiema and Laprise [2011]).

One further part of this thesis is the detailed investigation of the dynamical and diabatic contributions that generate and reduce the IV. A diabatic budget equation (Eq. 3.34) for the IV of the potential temperature developed by Nikiema and Laprise [2010] and Nikiema and Laprise [2011] is applied. This method reveals seven terms that contribute to the IV tendency.

For the Arctic domain the most important influence on IV is provided by the horizontal and vertical 'baroclinic' terms (B_h, B_v). B_h contributes to the growth of IV and B_v to a decreasing IV. Nikiema and Laprise [2010] and Nikiema and Laprise [2011] found as well that B_v contributes strongest to the reduction of IV over Northern American region, however the influence of B_h is weak over this domain. The negative contribution of B_v to IV tendency is caused by the statically stable atmosphere ($\frac{\partial(\theta)}{\partial p} < 0$) and the subsiding cold perturbations and rising warm perturbations ($\langle \theta'_n \omega'_n \rangle < 0$). The positive contribution of B_h to IV tendency is due to the movement of heat by the covariance of fluctuations of potential temperature and the horizontal wind that is against the horizontal gradient of the ensemble mean potential temperature. This means that cold fluctuations are transported towards warm regions and warm perturbations towards cold regions indicating a behaviour that generates IV.

Considering the horizontal transport term A_h the vertical profile and the temporal evolution suggest that the impact on IV is small, in accordance with the results of Nikiema and Laprise [2010] and Nikiema and Laprise [2011]. However, the spatial distribution of A_h reveals that its influence depends on the location within the model domain. A_h induces a reduction in a specific location when the IV is transported towards another location where it contributes to a generation of IV. In addition, A_h reaches positive values when IV is transported into the model domain and negative values when it is moved out of the model domain.

The diabatic source and sink term C (covariance of fluctuations of potential temperature and the diabatic heating rates J'_n) induces a decrease of IV below 900 hPa and an increase of IV above. IV grows in the higher levels due to the heating rates of vertical diffusion, radiation and condensation. The reduction of IV in lower levels is caused by the condensative and convective heating that is not fully compensated by the heating rates of radiation and vertical diffusion. Thus, over the Arctic the term C is influenced by other processes compared to Northern American region. In this mid-latitude region C leads to the strongest growth of IV induced by the condensative and convective heating (Nikiema and Laprise [2010] and Nikiema and Laprise [2011]).

In agreement with the results obtained over Northern American region the other terms (A_v , E_h and E_v) are small in general.

9.1.2 Dependency of the Arctic IV on the Sea Ice Conditions

The four ensembles are performed to verify the assumption that the sea ice conditions have an impact on the IV and the dynamical and diabatic contributions to IV tendency. This assumption is based on the findings that the reduced sea ice cover has an impact on the atmosphere. For example, the 2m air temperature and the specific humidity are increased during low ice conditions compared to high ice conditions, which leads to a decreased static stability (Schweiger et al. [2008], Porter et al. [2012], Jaiser et al. [2012], Rinke et al. [2013]). In addition, the radiative feedback is modified during low ice conditions due to the changed albedo over the open ocean compared to the ice covered conditions. This results in a reduced upward short-wave radiation at the surface and an enhanced upward long-wave radiation [Porter et al., 2012]. Thus, it is assumed that the IV is stronger during low ice conditions compared to high ice conditions, due to the changed energy fluxes.

Hence, the IV is analysed for two low ice years (2006, 2009) and two high ice years (2007, 2012). Contrary to the expectations an influence of the sea ice cover on the IV is not found for the atmospheric circulation and is only weak for the potential temperature. Only near the surface a classification between low and high ice years is possible based on the temporal averaged IV of potential temperature. However, differently than expected the IV decreases with reduced sea ice cover. In the middle and upper troposphere no distinct behaviour of IV is detected concerning low and high ice years.

The results for the individual contributions to the IV budget are quite similar between the ensembles. This is valid for the vertical profiles, the temporal evolution and the spatial patterns for all seven terms. The centres of maximum contribution to IV tendency are located in the same areas of the Arctic within all ensembles. Only slight differences between the ensembles are detected in the strength of the contributions for the horizontal 'baroclinic' term B_h and the diabatic source and sink term C . This could be related to the

sea ice cover. However, mostly this is valid only when the low ice year 2007 is compared to the high ice years 2006 and 2009. The IV and its contributions during the low ice year 2012 mainly behave differently to 2007. Probably this is due to the fact, that the intense sea ice retreat during 2012 is induced due to the great Arctic cyclone event during the beginning of August (Simmonds and Rudeva [2012], Zhang et al. [2013], Parkinson and Comiso [2013]). This event leads to a break up and melting of the already thin sea ice. In general, the strongest sea ice reduction is observed when the Arctic atmosphere is characterised by warm and anticyclonic conditions (Ogi and Wallace [2007], Dorn et al. [2012]) or a positive Arctic dipole anomaly (DA) occurs [Wang et al., 2009].

The results obtained by comparing the two low ice years and the two high ice years lead not to solid conclusions about the impact of sea ice cover on IV. Maybe, the considered number of years with low and high ice conditions is too small. Besides, the chosen years all represent the "new state" of the Arctic and thus, differ too little concerning their sea ice extent. Hence, years with more distinct high ice conditions (as those occurred in the 1980s and 1990s) should be analysed and compared with the 2000s.

Another reason for the similarity across the ensembles arises from the consideration of the seasonal mean which was used for the investigation of the IV and its contributions. This approach averages out the detected signals on daily time scales. Therefore, individual time steps have been analysed too, to get a more detailed insight concerning the impact of the atmospheric and sea ice conditions on the IV. Indeed, it is found that on specific time steps the horizontal and vertical 'baroclinic' terms (B_h , B_v) contribute both positively and negatively to the IV tendency of potential temperature depending on the location within the model domain. A relation between B_h and B_v and the EGR is detected for some of the investigated cases, illustrating the influence of cyclones on the IV. The strongest correspondence is found for the 5th August 2012 coinciding with the great Arctic cyclone event. Besides, the diabatic source and sink term C has a strong positive impact on the IV tendency depending on the time step. However, it is hard to detect a relation between the sea ice cover and the terms B_h , B_v and C . Only on 16th August 2009 and 5th August 2012 a spatial pattern correlation has been found. This leads to the conclusion that the investigation of individual time steps is may not practical as well, because it cannot be required that the sea ice retreat and its impact on IV occur simultaneously. It cannot be ruled out that both processes are exposed to a temporal shift. Concerning larger time scales Rinke et al. [2013] discussed the impact of the sea ice retreat during September on the atmospheric conditions and feedbacks in the following autumn and winter. Perhaps, the influence of the sea ice conditions during September on the IV is stronger in the following season than directly in the summer.

9.1.3 Dependency of the Arctic IV on the Model

In cooperation with the Canadian group [Nikiema et al., 2015], it was possible to compare the IV and its dynamical and diabatic contributions generated with the HIRHAM5 to another RCM, namely the CRCM5. The comparison is performed for the low ice year 2012 covering the season from July to September. Both RCMs use the same integration area over the Arctic with a horizontal resolution of approximately 25 km and are driven with the same LBC and partly the same IC.

The investigation reveals that both RCMs provide quite similar characteristics for the IV of the Arctic, apart from the fact, that the IV generated within the HIRHAM5 is smaller than the IV in CRCM5 simulations. Strongest differences are found in the lower troposphere probably caused by the differing parameterisation, for example concerning the land-surface and sea ice processes. The seven terms that contribute to IV tendency of potential temperature in the two RCMs exhibit the same sign (indicating a production or reduction of IV) and magnitude. Even the spatial patterns are quite similar for the RCMs indicating a weak dependency of the applied model on the IV and its contributions.

However, it is detected that the dynamical contributions (A_h , B_h , B_v) to IV tendency of potential temperature generated within the HIRHAM5 are weaker compared to the CRCM5. But, the diabatic term C reaches higher values of producing the IV within the HIRHAM5 compared to the CRCM5. The individual covariances between the fluctuations of potential temperature and the heating rates due to convection, condensation, vertical diffusion and radiation that are summarised in C , behave differently within both models. This is associated with the different parameterisation and might also be connected with the different sea ice thickness that is set constant to 2 m in HIRHAM5, whereas it is calculated in CRCM5. The sum of all four parts of C leads to a similar vertical structure of the entire C term within both models. Only a slight shift towards a weaker negative contribution near the surface and a stronger positive contribution above 900 hPa is found for the HIRHAM5 compared to the CRCM5. This may be explainable due to the neglected horizontal diffusion in the HIRHAM5's IV budget. The horizontal diffusion contributes negatively to the IV tendency and is considered in the CRCM5's IV budget.

The comparison of two RCMs reveals that the IV is a natural generation process caused by the non-linear behaviour of the atmospheric dynamics and does not depend on the physical or numerical structure of the model.

9.2 Outlook

Like summarised in Sec. 9.1 the IV of potential temperature in an Arctic RCM and its dynamical and diabatic contributions do not depend on the sea ice conditions and on the

chosen RCM. This leads to the conclusion that the processes inducing the IV is related to the non-linear behaviour within the model domain in general. However, it is well known, that the non-linear behaviour depends on the general atmospheric circulation. Hence, the magnitude and the behaviour of the IV is influenced by the location of the model domain and by the season. This is detected as well in this study by comparing the results obtained for the Arctic with the northeastern part of the Northern American region. Further, it is assumed that there is a dependency of the IV on the season. Already Rinke and Dethloff [2000] and Rinke et al. [2004] analysed the IV generated with a RCM covering the Arctic during different seasons and identified a stronger IV during winter compared to summer. Hence, the next step should be the investigation of HIRHAM5's IV and its dynamical and diabatic contributions for the winter season.

The detected independency of the IV on the sea ice conditions has to be analysed in a more detailed way. An enhanced number of years need to be investigated to enlarge the ensemble of high and low ice years to be able to achieve more solid results. Besides, the definition of high ice years should be related with a sea ice area that is one standard deviation larger than the 30-year climatology from 1981 to 2010 (commonly used by the NSIDC [2015]). This ensures a more distinct contrast between high and low ice years and helps to detect statistical significant differences between those years. It is assumed that the constant sea ice thickness in HIRHAM5 (set to 2 m) leads to a reduced energy exchange between the ocean and the atmosphere resulting in a weaker dependency of the IV on the sea ice cover. Hence, the vertical fluxes of turbulent heat over ocean areas should be analysed within HIRHAM5. In addition, a sensitivity experiment with a thinner sea ice thickness in HIRHAM5 could provide a clearer conclusion about the influence of the sea ice cover on the IV and its contributions.

Further, it need to be considered that the IV of potential temperature was performed mainly for the temporal averages over the season from July to September. This results in a cancelling out of the short-term fluctuations of IV and the mean state of IV is captured only. With the investigation of the individual time steps it is tried to compensate this weakness, however, only for some cases a dependency of the IV on the atmospheric conditions could be detected. Thus, the connection between the IV of potential temperature and the atmospheric and sea ice conditions is not clearly understood by using seasonal averages and individual time steps. Hence, further analysis covering different time scales have to be investigated in future. This includes the consideration of shifts between the IV event and the corresponding atmospheric conditions and sea ice events.

Bibliography

- Alexandru, A., de Elía, R., Laprise, R., 2007. Internal Variability in Regional Climate Downscaling at the Seasonal Scale. *Monthly Weather Review* 135, 3221–3238. [1, 2, 3, 10, 11, 15, 25, 36, 46, 62, 74, 98]
- Alexandru, A., de Elía, R., Laprise, R., 2009. Sensitivity Study of Regional Climate Model Simulations to Large-Scale Nudging Parameters. *Monthly Weather Review* 137, 1666–1686. [3]
- Benoit, R., Côté, J., Mailhot, J., 1989. Inclusion of a TKE boundary layer parameterization in the Canadian regional finite-element model. *Monthly Weather Review* 117, 1726–1750. [78]
- Buizza, R., Palmer, T. N., 1998. Impact of Ensemble Size on Ensemble Prediction. *Monthly Weather Review* 126, 2503–2518. [2]
- Caya, D., Biner, S., 2004. Internal variability of RCM simulations over an annual cycle. *Climate Dynamics* 22, 33–46. [1, 2, 3, 51, 74, 98]
- Christensen, O. B., Christensen, J. H., Machenhauer, B., Botzet, M., 1998. Very-high-resolution regional climate simulations over scandinavia. *Journal of Climate* 11, 3204–3229. [1]
- Christensen, O. B., Drews, M., Christensen, J. H., Dethloff, K., Ketelsen, K., Hebestadt, I., Rinke, A., 2007. The HIRHAM Regional Climate Model Version 5(b). Technical Report 06-17, 1–22. [7]
- Christensen, O. B., Gaertner, M. A., Prego, J. A., Polcher, J., 2001. Internal variability of regional climate models. *Climate Dynamics* 17, 875–887. [1, 3, 51, 98]
- Côté, J., Gravel, S., Méthot, A., Patoine, A., Roch, M., Staniforth, A., 1998. The operational CMC-MRB Global Environmental Multiscale (GEM) model: Part I. Design Consideration and Formulation. *Monthly Weather Review* 126, 1373–1395. [77]

- Crétat, J., Pohl, B., 2012. How Physical Parameterizations Can Modulate Internal Variability in a Regional Climate Model. *Journal of the Atmospheric Sciences* 69, 714–724. [3]
- Davies, H., 1976. A lateral boundary formulation for multi-level prediction models. *Quarterly Journal of Meteorological Society* 102, 405–418. [10]
- Davies, H., Turner, R., 1977. Updating prediction models by dynamical relaxation: An examination of the technique. *Quarterly Journal of Meteorological Society* 103, 225–245. [10]
- Dee, D. P., Uppala, S. M., Simmons, A. J., Berrisford, P., Poli, P., Kobayashi, S., Andrae, U., Balmaseda, M. A., Balsamo, G., Bauer, P., Bechtold, P., Beljaars, A. C. M., van de Berg, L., Bidlot, J., Bormann, N., Delsol, C., Dragani, R., Fuentes, M., Geer, A. J., Haimberger, L., Healy, S. B., Hersbach, H., Holm, E. V., Isaksen, L., Kållberg, P., Köhler, M., Matricardi, M., McNally, A. P., Monge-Sanz, B. M., Morcrette, J.-J., Park, B.-K., Peubey, C., de Rosnay, P., Tavolato, C., Thepaut, J.-N., F., V., 2011. The ERA-Interim reanalysis: configuration and performance of the data assimilation system. *Quarterly Journal of the Royal Meteorological Society* 137, 553–597. [9]
- Denis, B., Laprise, R., Côté, J., 2002. Downscaling ability of one-way nested regional climate models: the big-brother experiment. *Climate Dynamics* 18, 627–646. [1]
- Dethloff, K., Rinke, A., Lehmann, R., Christensen, J. H., Botzet, M., Machenhauer, B., 1996. Regional climate model of the Arctic atmosphere. *Journal of Geophysical Research* 101, 23401–23422. [5]
- Dorn, W., Dethloff, K., Rinke, A., 2012. Limitation of a coupled regional climate model in the reproduction of the observed Arctic sea-ice retreat. *The Cryosphere* 6, 985–998. [29, 31, 100]
- Eady, E. T., 1949. Long Wave and Cyclone Waves. *Tellus* 1, 33–52. [14]
- Ebert, E. E., Curry, J. A., 1993. An intermediate one-dimensional thermodynamic sea ice model for investigating ice-atmosphere interactions. *Journal of Geophysical Research* 98, 10085–10109. [78]
- Eckermann, S., 2009. Hybrid σ -p Coordinate Choices for a Global Model. *Monthly Weather Review* 137, 224–245. [7]
- ECMWF, 2015. Known quality issues with ERA-Interim data: old.ecmwf.int/research/era/do/get/index/QualityIssues. Last accessed 22. April 2015. [26, 29]

BIBLIOGRAPHY

- Flato, G. M., Brown, R. D., 1996. Variability and climate sensitivity of landfast Arctic sea ice. *Journal of Geophysical Research* 101 (C11), 25767–25777. [78]
- Fouquart, Y., Bonnel, B., 1980. Computation of Solar Heating of the Earth's Atmosphere: A New Parameterization. *Beiträge zur Physik der Atmosphäre* 53, 35–62. [8, 78]
- Giorgi, F., Bi, X., 2000. A study of internal variability of a regional climate model. *Journal of Geophysical Research* 105, 29503–29521. [1, 2, 3, 51, 62, 98]
- Gneiting, T., Raftery, A. E., 2005. Weather Forecasting with Ensemble Methods. *Science* 310, 248–249. [2]
- Hagemann, S., 2002. An Improved Land Surface Parameter Dataset for Global and Regional Climate Models. Technical Report 336, Max-Planck-Institut (MPI) für Meteorologie, Hamburg, 1–21. [8]
- Hoskins, B. J., Valdes, P. J., 1990. On the Existence of Storm-Tracks. *Journal of the Atmospheric Sciences* 47 (15), 1854–1864. [14]
- IPCC, 2013. Climate Change 2013: The Physical Science Basis, Chapter 11: Near-term Climate Change: Projections and Predictability. Working Group I: Contribution to the IPCC 5th Assessment Report, 953–1028. [1]
- Jaiser, R., Dethloff, K., Handorf, D., Rinke, A., Cohen, J., 2012. Impact of sea ice cover changes on the Northern Hemisphere atmospheric winter circulation. *Tellus* 64, Article ID 11595, 11 pages. [4, 14, 74, 99]
- Kain, J. S., Fritsch, J. M., 1990. One-Dimensional Entraining/Detraining Plume Model and Application in Convective Parameterization. *Journal of the Atmospheric Sciences* 47, 2784–2802. [78]
- Klaus, D., 2014. Validierung und Verbesserung der arktischen Wolkenparametrisierung im regionalen Atmosphärenmodell HIRHAM5. Ph.D. thesis, University Potsdam. [8, 10, 31, 36]
- Klaus, D., Dorn, W., Dethloff, K., Rinke, A., Mielke, M., 2012. Evaluation of two cloud Parameterizations and their possible adaptation to arctic climate conditions. *Atmosphere* 3, 419–450. [10]
- Køltzow, M., 2007. The effect of a new snow and sea ice albedo scheme on regional climate model simulations. *Journal of Geophysical Research* 112, D07 110. [8]

BIBLIOGRAPHY

- Kuo, H. L., 1965. On Formation and Intensification of Tropical Cyclones Through Latent Heat Release by Cumulus Convection. *Journal of the Atmospheric Sciences* 22, 40–63. [78]
- Laprise, R., 1992. The Euler Equation of Motion with Hydrostatic Pressure as an Independent Variable. *Monthly Weather Review* 120, 197–207. [77]
- Laprise, R., de Elía, R., Caya, D., Biner, S., Lucas-Picher, P., Diaconescu, E., Leduc, M., Alexandru, A., Separovic, L., Canadian Network for Regional Climate Modelling and Diagnostics, 2008. Challenging some tenets of Regional Climate Modelling. *Meteorology and Atmospheric Physics* 100, 3–222. [1]
- Li, J., Barker, H. W., 2005. A Radiation Algorithm with Correlated-k Distribution: Part I Local and Thermal Equilibrium. *Journal of the Atmospheric Sciences* 62, 286–309. [78]
- Lindzen, R. S., Farrell, B., 1980. A Simple Approximate Result for the Maximum Growth Rate of Baroclinic Instabilities. *Journal of the Atmospheric Sciences* 37, 1648–1654. [14]
- Lorenz, E. N., 1963. Deterministic nonperiodic flow. *Journal of the Atmospheric Sciences* 20, 130–141. [1]
- Lucas-Picher, P., Caya, D., Biner, S., Laprise, R., 2008b. Quantification of the Lateral Boundary Forcing of a Regional Climate Model Using an Aging Tracer. *Monthly Weather Review* 136, 4980–4996. [1, 2]
- Lucas-Picher, P., Caya, D., de Elía, R., Laprise, R., 2008a. Investigation of regional climate models' internal variability with a ten-member ensemble of 10-year simulations over a large domain. *Climate Dynamics* 31, 927–940. [1, 2, 3, 10, 25, 46, 51, 62]
- Mlawer, E. J., Taubman, S. J., Brown, P. D., Iacono, M. J., Clough, S. A., 1997. Radiative transfer for inhomogeneous atmospheres: RRTM, a validated correlated-k model for the longwave. *Journal of Geophysical Research* 102 (D14), 16663–16682. [8, 78]
- Nikiema, O., Laprise, R., 2010. Diagnostic budget study of the internal variability in ensemble simulations of the Canadian RCM. *Climate Dynamics* 36, 2313–2337. [I, III, 2, 3, 4, 16, 23, 25, 36, 51, 53, 56, 62, 98, 99]
- Nikiema, O., Laprise, R., 2011. Budget study of the internal variability in ensemble simulations of the Canadian Regional Climate Model at the seasonal scale. *Journal of Geophysical Research* 116, 1–18. [I, III, 2, 3, 16, 25, 36, 62, 98, 99]

BIBLIOGRAPHY

- Nikiema, O., Sommerfeld, A., Laprise, R., Rinke, A., Dethloff, K., 2015. Chaos in Regional Climate Model simulations over the Arctic domain: Comparison of inter-member variability in ensemble simulations of CRCM5 and HIRHAM5 models. *Polarforschung*, in review. [3, 77, 80, 83, 101]
- NSIDC, 2015. National Snow and Ice Data Center: Arctic Sea Ice News & Analysis - Monthly Archives: nsidc.org/arcticseaicenews/. Last accessed 24. January 2015. [13, 26, 28, 29, 30, 34, 102]
- O'Brien, T. A., Sloan, L. C., Snyder, M. A., 2011. Can ensembles of regional climate model simulations improve results from sensitivity studies? *Climate Dynamics* 37, 1111–1118. [2]
- Ogi, M., Wallace, J. M., 2007. Summer minimum Arctic sea ice extent and the associated summer atmospheric circulation. *Geophysical Research Letters* 34, L12705. [100]
- Omrani, H., Drobinski, P., Dubos, T., 2012a. Investigation of indiscriminate nudging and predictability in a nested quasi-geostrophical model. *Quarterly Journal of the Royal Meteorological Society* 138, 158–169. [3, 10, 36]
- Omrani, H., Drobinski, P., Dubos, T., 2012b. Spectral nudging in regional climate modelling: how strongly should we nudge? *Quarterly Journal of the Royal Meteorological Society* 138, 1808–1813. [3]
- Paciorek, C. J., Risbey, J. S., Ventura, V., Rosen, R. D., 2002. Multiple Indices of Northern Hemisphere Cyclone Activity, Winter 1949-99. *Journal of Climate* 15, 1573–1590. [14]
- Parkinson, C. L., Comiso, J. C., 2013. On the 2012 record low Arctic sea ice cover: Combined impact of preconditioning and an August storm. *Geophysical Research Letters* 40, 1356–1361. [31, 33, 43, 56, 96, 100]
- Porter, D. F., Cassano, J. J., Serreze, M. C., 2012. Local and large-scale atmospheric response to reduced Arctic sea ice and ocean warming in the WRF model. *Journal of Geophysical Research* 117, 1–21. [4, 69, 71, 74, 99]
- Rapać, M., Leduc, M., Laprise, R., 2011. Evaluation of internal variability and estimation of downscaling ability of the Canadian Regional Climate Model for different domain sizes over the north atlantic region using the Big-Brother experimental approach. *Climate Dynamics* 36, 1979–2001. [2, 3]
- Rinke, A., Dethloff, K., 2000. On the sensitivity of a regional Arctic climate model to initial and boundary conditions. *Climate Research* 14, 101–113. [2, 3, 4, 25, 36, 45, 46, 97, 102]

BIBLIOGRAPHY

- Rinke, A., Dethloff, K., Dorn, W., Handorf, D., Moore, J. C., 2013. Simulated Arctic atmospheric feedbacks associated with late summer sea ice anomalies. *Journal of Geophysical Research: Atmospheres* 118, 7698–7714. [4, 14, 99, 100]
- Rinke, A., Marbaix, P., Dethloff, K., 2004. Internal Variability in Arctic regional climate simulations: case study for the SHEBA year. *Climate Research* 27, 197–209. [1, 3, 4, 25, 41, 46, 51, 74, 97, 98, 102]
- Rockel, B., Raschke, E., Weyres, B., 1991. A Parameterization of Broad Band Radiative Transfer Properties of Water, Ice and Mixed Clouds. *Beiträge zur Physik der Atmosphäre* 64, 1–12. [8]
- Roeckner, E., Bäuml, G., Bonaventura, L., Brokopf, R., Esch, M., Giorgetta, M., Hagemann, S., Kirchner, I., Kornblueh, L., Manzini, E., Rhodin, A., Schlese, A., Schulzweida, U., Tompkins, A., 2003. The atmospheric general circulation model ECHAM5. Part I: Model description. MPI-Report 349. [7, 8, 78]
- Roesch, A., Jaeger, E. B., Lüthi, D., Seneviratne, S. I., 2008. Analysis of CCLM model biases in relation to intra-ensemble model variability. *Meteorologische Zeitschrift* 17 (4), 369–382. [2, 3]
- Schweiger, A. J., Lindsay, R. W., Vavrus, S., Francis, J. A., 2008. Relation between Arctic sea ice and clouds during autumn. *Journal of Climate* 21 (18), 4799–4810. [71, 99]
- Semtner, A. J., 1976. A Model for the Thermodynamic Growth of Sea Ice in Numerical Investigations of Climate. *Journal of Physical Oceanography* 6, 379–389. [78]
- Separovic, L., de Elía, R., Laprise, R., 2011. Impact of spectral nudging and domain size in studies of RCM response to parameter modification. *Climate Dynamics* 38 (7-8), 1325–1343. [3]
- Serreze, M. C., 1995. Climatology Aspects of Cyclone Development and Decay in the Arctic. *Atmosphere-Ocean* 33, 1–23. [38]
- Serreze, M. C., Barrett, A. P., 2008. The Summer Cyclone Maximum over the Central Arctic Ocean. *Journal of Climate* 21, 1048–1065. [14, 65]
- Serreze, M. C., Box, J. E., Barry, R. G., Walsh, J. E., 1993. Characteristics of Arctic Synoptic Activity, 1952-1989. *Meteorology and Atmospheric Physics* 51, 147–164. [38, 66]
- Serreze, M. C., Lynch, A. H., Clark, M. P., 2001. The Arctic Frontal Zone as Seen in the NCEP-NCAR Reanalysis. *Journal of Climate* 14, 1550–1567. [37, 65, 68]

BIBLIOGRAPHY

- Simmonds, I., Lim, E.-P., 2009. Bias in the calculation of Southern Hemisphere mean baroclinic eddy growth rate. *Geophysical Research Letters* 36, 1–5. [14]
- Simmonds, I., Rudeva, I., 2012. The great Arctic cyclone of August 2012. *Geophysical Research Letters* 39, 1–6. [31, 33, 43, 56, 96, 100]
- Sommerfeld, A., Nikiema, O., Rinke, A., Dethloff, K., Laprise, R., 2015. Arctic budget study of intermember variability using HIRHAM5 ensemble simulations. *Journal of Geophysical Research - Atmosphere* 120, 9390–9407. [3, 98]
- Sorteberg, A., Walsh, J. E., 2008. Seasonal cyclone variability at 70 N and its impact on moisture transport into the Arctic. *Tellus* 60A, 570–586. [38, 66]
- Strey, S. T., Chapman, W. L., Walsh, J. E., 2015. The 2007 sea ice minimum: Impact on the Northern Hemisphere atmosphere in late autumn and early winter. *Journal of Geophysical Research* 115, D23103. [71]
- Sundqvist, H., Berge, E., Kristjansson, J. E., 1989. Condensation and Cloud Parameterization Studies with a Mesoscale Numerical Weather Prediction Model. *Monthly Weather Review* 117, 1641–1657. [78]
- Tanre, D., Geleyn, J.-F., Slingo, J. M., 1984. First results of the introduction of an advanced aerosol-radiation interaction in the ECMWF low resolution global model. In: Gerber, H., Deepak, A. (Eds.), *Aerosols and their Climate Effects*. pp. 133–177. [8]
- Theis, S., Gebhardt, C., 2009. Grundlagen der Ensembletechnik und Wahrscheinlichkeitsaussagen. In: Rapp, J. (Ed.), *promet - Moderne Verfahren und Instrumente der Wettervorhersage im Deutschen Wetterdienst*. Vol. 35 (1/3). Deutscher Wetterdienst, pp. 104–110. [2]
- Tiedtke, M., 1989. A comprehensive mass flux scheme for cumulus parameterization in large-scale models. *Monthly Weather Review* 117, 1779–1799. [8, 78]
- Tompkins, A. M., 2002. A Prognostic Parameterization for the Subgrid-Scale Variability of Water Vapor and Clouds in Large-Scale Models and Its Use to Diagnose Cloud Cover. *Journal of the Atmospheric Sciences* 59 (12), 1917–1942. [8, 78]
- Undén, P., Rontu, L., Järvinen, H. J., Lynch, P., Calvo, J., Cats, G., Cuxart, J., Eerola, K., Fortelius, C., Garcia-Moya, J. A., 2002. HIRLAM Scientific Documentation. HIRLAM-5 Project, Swedish Meteorological and Hydrological Institute (SMHI): Norrköping, Sweden. [7]

BIBLIOGRAPHY

- van Engelen, R., Wolters, L., Cats, G., 1997. Tomorrow's Weather Forecast: Automatic Code Generation for Atmospheric Modeling. *IEEE Computational Science & Engineering* 4 (3), 22–31. [7]
- von Storch, H., 2005. Models of global and regional climate. In: Anderson, M. G. (Ed.), *Meteorology and Climatology. Encyclopedia of Hydrological Sciences*, pp. 478–490. [2, 3, 15, 46, 51, 98]
- Wang, J., Zhang, J., Watanabe, E., Ikeda, M., Mizobata, K., Walsh, J. E., Bai, X., Wu, B., 2009. Is the Dipole Anomaly a major driver to record lows in Arctic summer sea ice extent? *Geophysical Research Letters* 36, L05706. [28, 29, 100]
- Wu, W., Lynch, A. H., Rivers, A., 2005. Estimating the Uncertainty in a Regional Climate Model Related to Initial and Lateral Boundary Conditions. *Journal of Climate* 18, 917–931. [1, 3, 51]
- Zadra, A., Caya, D., Côté, J., Dugas, B., Jones, C., Laprise, R., Winger, K., Caron, L.-P., 2008. The Next Canadian Regional Climate Model. *Physics in Canada* 64 (2), 74–83. [77]
- Zhang, J., Lindsay, R., Schweiger, A., Steele, M., 2013. The impact of an intense summer cyclone on 2012 arctic sea ice retreat. *Geophysical Research Letters* 40, 720–726. [31, 33, 34, 43, 48, 56, 96, 100]
- Zhang, X., Walsh, J. E., Zhang, J., Bhatt, U. S., Ikeda, M., 2004. Climatology and Interannual Variability of Arctic Cyclone Activity: 1948-2002. *Journal of Climate* 17, 2300–2317. [38]
- Zhou, X., Matthes, H., Rinke, A., Klehmet, K., Heim, B., Dorn, W., Klaus, D., Dethloff, K., Rockel, B., 2014. Evaluation of the Arctic Land Snow Cover Characteristics, Surface Albedo, and Temperature during the Transition Seasons from Regional Climate Model Simulations and Satellite Data. *Advanced Meteorology*, Article ID 604157, 15 pages. [10]

Chapter A

Appendix

A.1 Equations

Reynolds Decomposition and Reynolds Postulates

$$a = \langle a \rangle + a' \quad (\text{A.1})$$

$$\langle \langle a \rangle \rangle = \langle a \rangle \quad (\text{A.2})$$

$$\langle a' \rangle = 0 \quad (\text{A.3})$$

$$\langle a \rangle = \langle \langle a \rangle + a' \rangle = \langle \langle a \rangle \rangle + \langle a' \rangle = \langle a \rangle \quad (\text{A.4})$$

$$\langle ab \rangle = \langle a \rangle \langle b \rangle + \underbrace{\langle \langle a \rangle b' \rangle}_{=0} + \underbrace{\langle a' \langle b \rangle \rangle}_{=0} + \langle a' b' \rangle \quad (\text{A.5})$$

$\vec{\nabla}$ -Rules

$$\vec{\nabla} \cdot (a\vec{A}) = a\vec{\nabla} \cdot \vec{A} + \vec{A} \cdot \vec{\nabla} a \quad (\text{A.6})$$

Euler Decomposition

$$\frac{D}{Dt} = \frac{\partial}{\partial t} + \langle \vec{V} \rangle \cdot \vec{\nabla} + \langle \omega \rangle \frac{\partial}{\partial p} \quad (\text{A.7})$$

A.2 Figures

A.2.1 Vertical Profile of the Contributions to IV Tendency

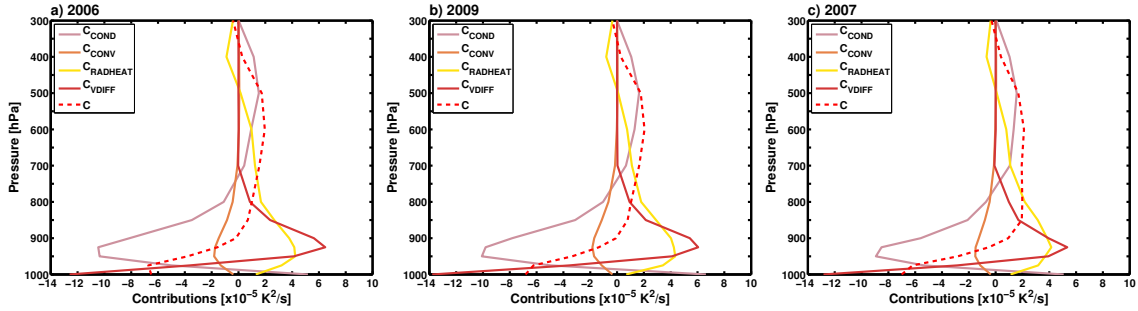


Figure A.1: Vertical profile of the temporal and domain averaged contribution C in $10^{-5} K^2/s$ (dashed lines) to IV tendency and the separated parts of the term C meaning the covariances between the fluctuations of potential temperature and temperature tendencies due to condensation, convection, radiation and vertical diffusion, respectively for the ensembles representing the high ice years 2006 (a), 2009 (b) and the low ice year 2007 (c). The dashed lines are identical to the red lines in Fig. 6.1(a) for 2006 (dashed line) and 2009 (solid line) and Fig. 6.1(b) for 2007 (dashed line). The corresponding figure for the ensemble representing the low ice year 2012 is shown in Sec. 6.1 in Fig. 6.2.

A.2.2 Temporal Evolution of the Contributions to IV Tendency

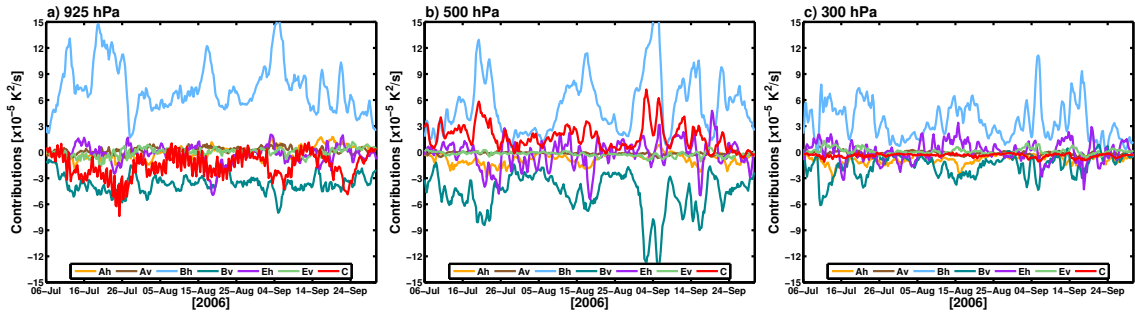


Figure A.2: Temporal evolution of the domain averaged seven contributions in $10^{-5} K^2/s$ to IV tendency at 925 hPa (a), 500 hPa (b) and 300 hPa (c) for the ensemble representing the high ice year 2006.

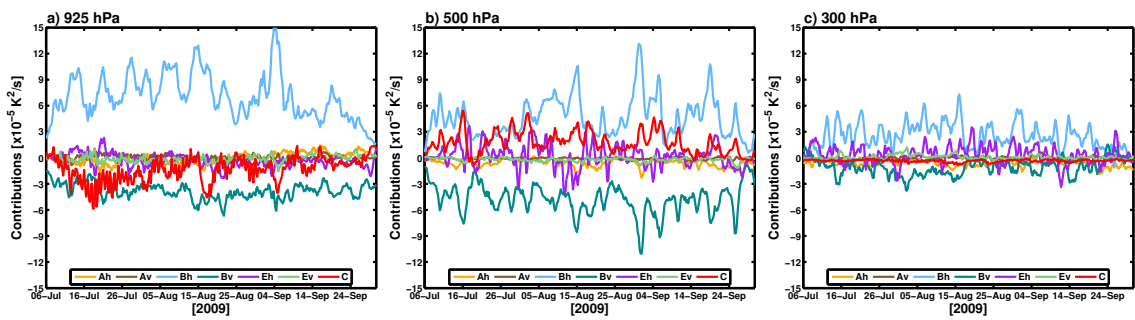


Figure A.3: Temporal evolution of the domain averaged seven contributions in $10^{-5} K^2/s$ to IV tendency at 925 hPa (a), 500 hPa (b) and 300 hPa (c) for the ensemble representing the high ice year 2009.

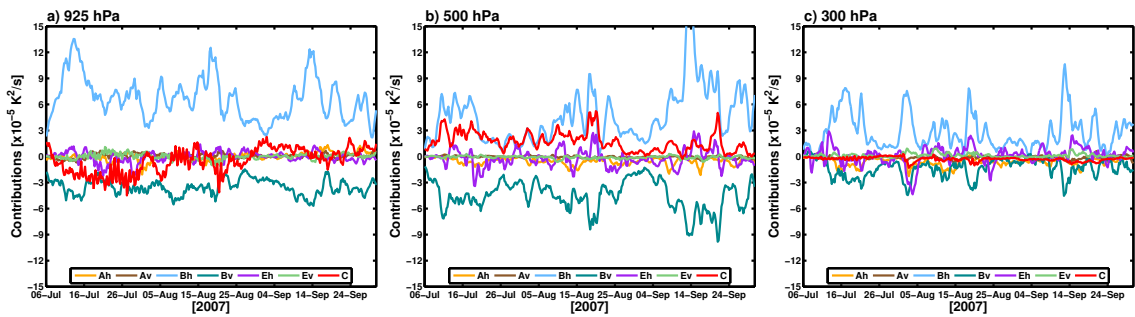


Figure A.4: Temporal evolution of the domain averaged seven contributions in $10^{-5} K^2/s$ to IV tendency at 925 hPa (a), 500 hPa (b) and 300 hPa (c) for the ensemble representing the low ice year 2007. The corresponding figures for the ensemble representing the low ice year 2012 are shown in Sec. 6.2 in Fig. 6.5.

A.2.3 Spatial Distribution of the Contributions to IV Tendency

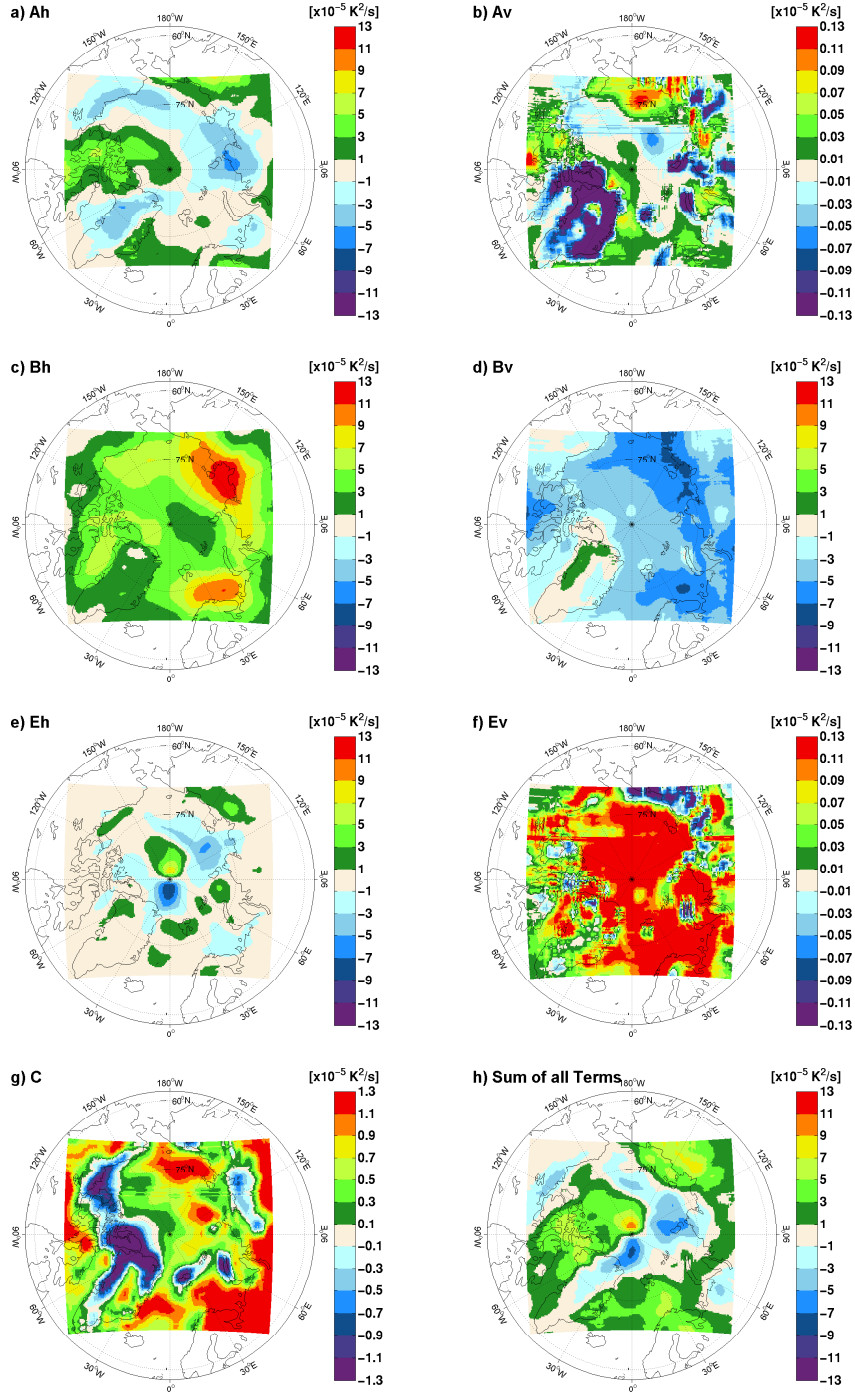


Figure A.5: Spatial distribution of the temporal and vertical averaged seven contributions in $10^{-5} K^2/s$ to IV tendency ((a)-(g)) and the sum of all contributions in $10^{-5} K^2/s$ (h) for the ensemble representing the high ice year 2006. The contribution C is 10 times and the A_v and E_v are 100 times smaller than the other contributions, therefore, the colorbars are adapted.

A.2. FIGURES

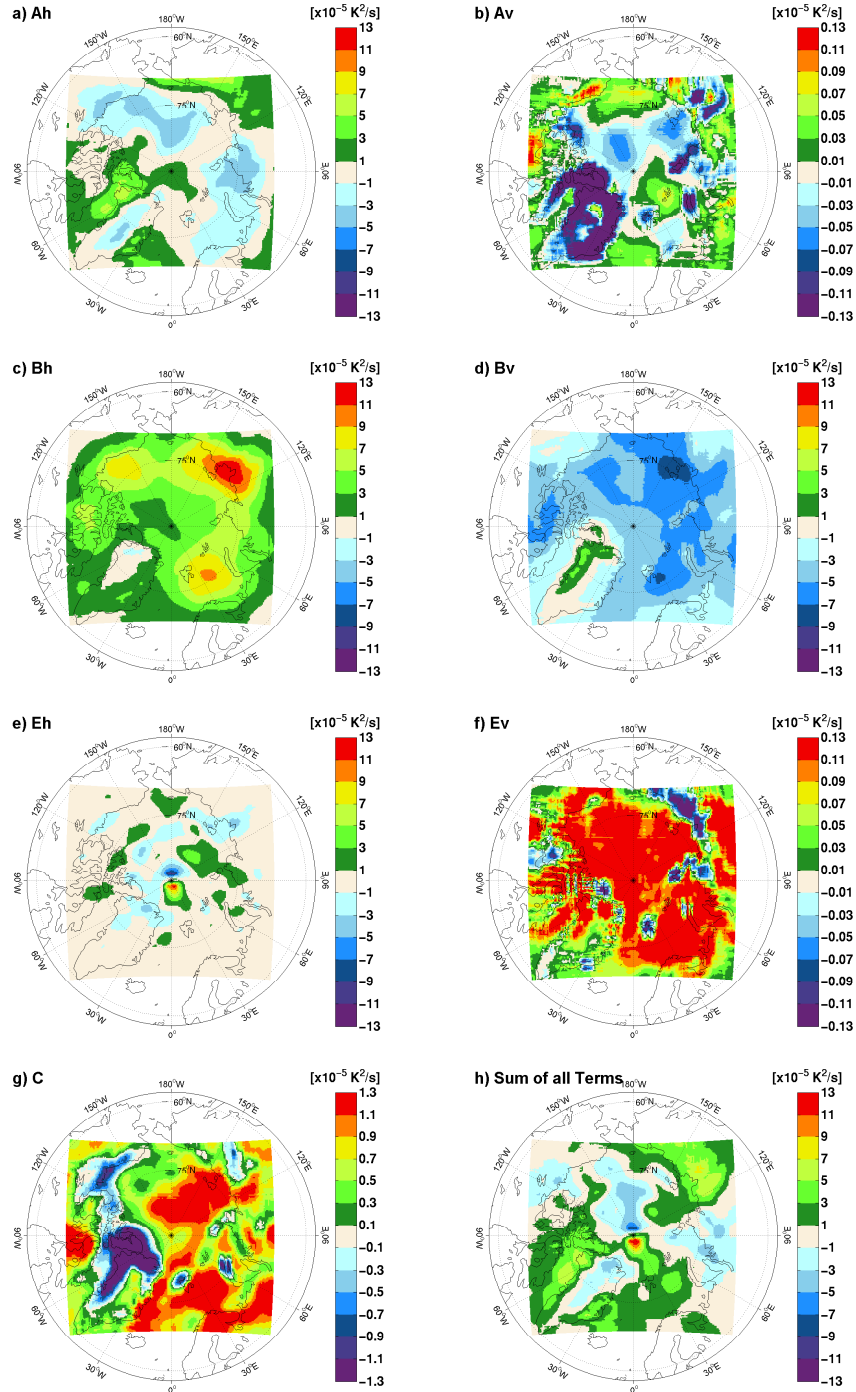


Figure A.6: Spatial distribution of the temporal and vertical averaged seven contributions in $10^{-5} K^2/s$ to IV tendency ((a)-(g)) and the sum of all contributions in $10^{-5} K^2/s$ (h) for the ensemble representing the high ice year 2009. The contribution C is 10 times and the A_v and E_v are 100 times smaller than the other contributions, therefore, the colorbars are adapted.

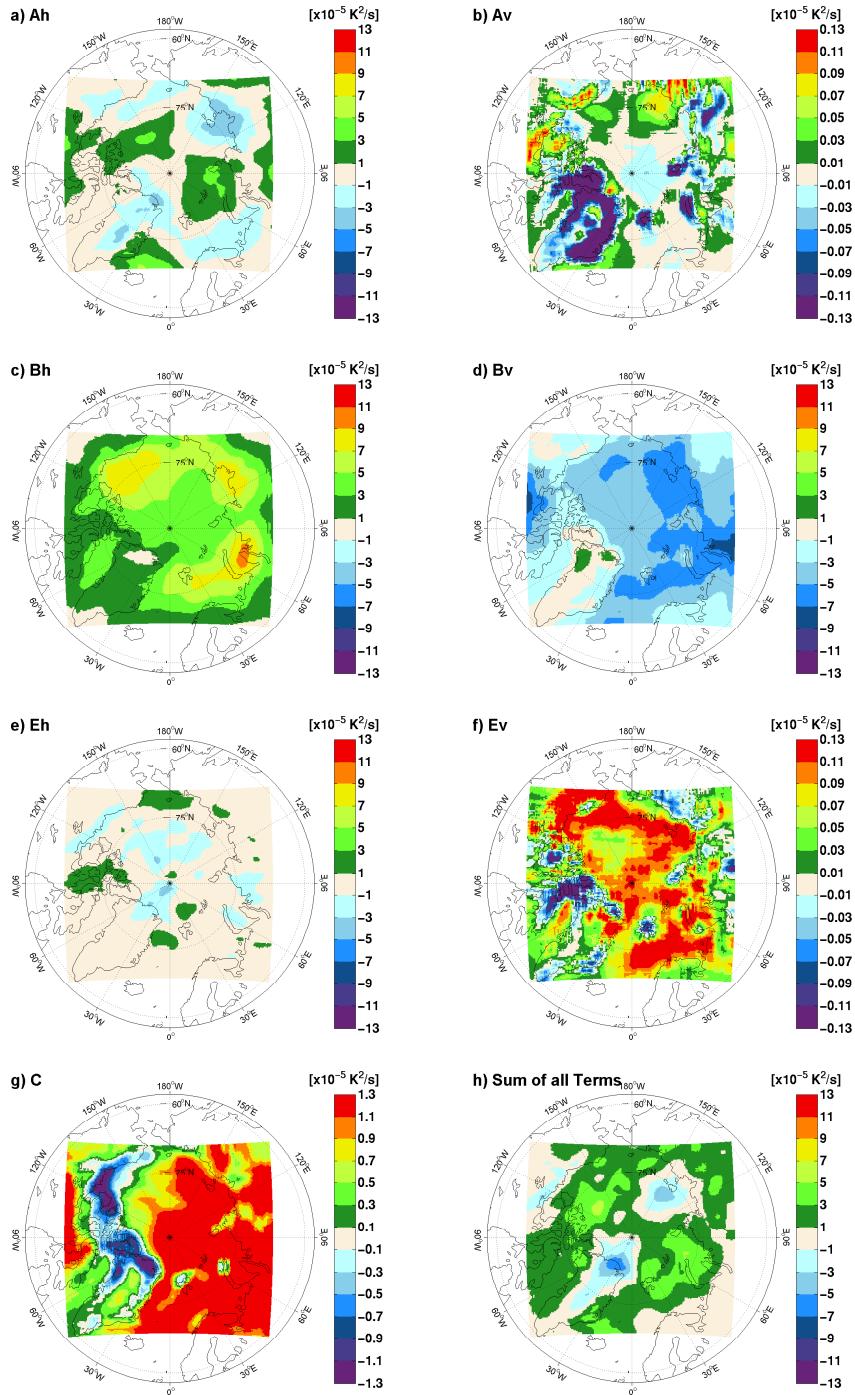


Figure A.7: Spatial distribution of the temporal and vertical averaged seven contributions in $10^{-5} K^2/s$ to IV tendency ((a)-(g)) and the sum of all contributions in $10^{-5} K^2/s$ (h) for the ensemble representing the low ice year 2007. The contribution C is 10 times and the A_v and E_v are 100 times smaller than the other contributions, therefore, the colorbars are adapted. The corresponding figures for the ensemble representing the low ice year 2012 are shown in Sec. 6.3 in Fig. 6.6.

Acknowledgements

First of all, I am grateful to Prof. Dr. Klaus Dethloff, Prof. Dr. René Laprise and Prof. Dr. Peter Lemke for reviewing this dissertation.

Additionally, I thank the Alfred Wegener Institute Helmholtz Centre for Polar and Marine Research in Potsdam to gave me the opportunity to write my thesis and the Helmholtz Climate Initiative REKLIM for funding this work.

The simulations with the HIRHAM5 were performed at the German Climate Computing Centre (DKRZ, Hamburg).

Special thanks go to Dr. Oumarou Nikiema and Prof. Dr. René Laprise from the Université du Québec á Montréal for providing and explaining me their method of the diagnostic budget study for the IV of potential temperature, for the scientific discussions and for enabling the usage of the data obtained with the CRCM5.

Furthermore, I would like to thank Ines Hebestadt for her technical support concerning the HIRHAM5 and the DKRZ.

I am grateful to Prof. Dr. Klaus Dethloff und Dr. Annette Rinke for supervising me during the three years of PhD. They always were ready to discuss with me, listen to me and answer my questions. Thank you for giving a lot of support by solving scientific problems and proofreading my thesis.

In addition, I thank my friendly colleagues Wolfgang Dorn, Daniel Klaus, Moritz Mielke, Thomas Orgis, Benjamin Segger, Fabian Kremser for (scientific) talks and the welcome diversions during the coffee breaks. Special thank goes to Franzi, not only for again sharing the office for several years, but rather for the motivation and encouraging words when I needed some and for your close friendship.

I wish to express my gratitude to all my friends beside the AWI for their moral support and friendship, despite the rare time we spend together during the last months. A lot of hugs go to all of them and especially to Benjamin.

My family always supported me in every way during my whole life and I would like to thank them. Grandma and Grandpa, I wish you could witness this moment with me, I miss you.

Declaration of Authenticity

I assure, that the present PhD thesis is entirely written by myself and the use of other material is clearly identified.

This work was not submitted to another university.

Potsdam, 14th December 2015

Anja Sommerfeld